

Karla Kauffmann

Including Collisions in Gyrokinetic Tokamak and Stellarator Simulations

**IPP 12/10
April, 2012**

Including Collisions in Gyrokinetic Tokamak and Stellarator Simulations

I n a u g u r a l d i s s e r t a t i o n

zur

Erlangung des akademischen Grades

doctor rerum naturalium (Dr. rer. nat.)

an der Mathematisch-Naturwissenschaftlichen Fakultät

der

Ernst-Moritz-Arndt-Universität Greifswald

vorgelegt von

Karla Kauffmann

geboren am 25.01.1982

in Antofagasta

Greifswald, 10.04.2012

Dekan:	Prof. Dr. Klaus Fesser
1. Gutachter:	Prof. Dr. Per Helander
2. Gutachter:	Prof. Dr. Laurent Villard
Tag der Promotion:	10.04.2012

Abstract

Particle and heat transport in fusion devices often exceed the neoclassical prediction. This anomalous transport is thought to be produced by turbulence caused by microinstabilities such as ion and electron-temperature-gradient (ITG/ETG) and trapped-electron-mode (TEM) instabilities, the latter ones known for being strongly influenced by collisions. Additionally, in stellarators, the neoclassical transport can be important in the core, and therefore investigation of the effects of collisions is an important field of study. Prior to this thesis, however, no gyrokinetic simulations retaining collisions had been performed in stellarator geometry.

In this work, collisional effects were added to EUTERPE, a previously collisionless gyrokinetic code which utilizes the δf method. To simulate the collisions, a pitch-angle scattering operator was employed, and its implementation was carried out following the methods proposed in [1, 2]. To test this implementation, the evolution of the distribution function in a homogeneous plasma was first simulated, where Legendre polynomials constitute eigenfunctions of the collision operator. Also, the solution of the Spitzer problem was reproduced for a cylinder and a tokamak. Both these tests showed that collisions were correctly implemented and that the code is suited for more complex simulations.

As a next step, the code was used to calculate the neoclassical radial particle flux by neglecting any turbulent fluctuations in the distribution function and the electric field. Particle fluxes in the neoclassical analytical regimes were simulated for tokamak and stellarator (LHD¹) configurations. In addition to the comparison with analytical fluxes, a successful benchmark with the DKES code was presented for the tokamak case, which further validates the code for neoclassical simulations.

¹Large Helical Device; a stellarator from the National Institute for Fusion Science (NIFS) located in Toki, Japan.

In the final part of the work, the effects of collisions were investigated for slab and toroidal ITGs and TEMs in a tokamak configuration. The results show that collisions reduce the growth rate of slab ITGs in cylinder geometry, whereas they do not affect ITGs in a tokamak, which are mainly curvature-driven. However it is important to note that the pitch-angle scattering operator does not conserve momentum, which is most critical in the parallel direction. Therefore, the damping found in a cylinder could be the consequence of this missing feature and not a physical result [3]. Nonetheless, the results are useful to determine whether the instability is mainly being driven by a slab or toroidal ITG mode.

EUTERPE also has the feature of including kinetic electrons, which made simulations of TEMs with collisions possible. The combination of collisions and kinetic electrons made the numerical calculations extremely time-consuming, since the time step had to be small enough to resolve the fast electron motion.

In contrast to the ITG results, it was observed that collisions are extremely important for TEMs in a tokamak, and in some special cases, depending on whether they were mainly driven by density or temperature gradients, collisions could even suppress the mode (in agreement with [4, 5]).

In the case of stellarators it was found that ITGs are highly dependent on the device configuration. For LHD it was shown that collisions slightly reduce the growth rate of the instability, but for Wendelstein 7-X² they do not affect it and the growth rate showed a similar trend with collisionality to that of the tokamak case. Collisions also tend to make the ballooning structure of the modes less pronounced.

²An optimized stellarator currently being built in the Institute for Plasma Physics (IPP) located in Greifswald, Germany.

Contents

Contents	vii
List of figures	xi
Nomenclature	xv
1 Introduction	1
1.1 Fusion	1
1.2 Plasma and magnetic confinement	3
1.3 Collisional transport	6
1.4 Anomalous transport and microinstabilities	8
1.5 Contribution of this thesis	8
1.6 Outline	9
2 Theoretical framework	11
2.1 Coordinate systems	11
2.2 Drift-kinetic and gyrokinetic model	13
2.3 Short description of numerics in EUTERPE	17
2.4 δf method and two-weight scheme	18
2.4.1 δf method without collisions	19
2.4.2 Collisional δf method	20
2.4.3 Initial conditions	24
2.5 Collision operator	25
2.5.1 Fokker-Planck operator	26
2.5.2 Pitch-angle scattering	29
2.5.3 Implementation in EUTERPE	34

CONTENTS

2.6	Neoclassical formalism	38
2.6.1	Particle orbits	39
2.6.2	Characteristic parameters	40
2.6.3	Neoclassical transport equations	42
2.6.4	General considerations for EUTERPE	44
2.7	Stellarator geometries used	45
2.7.1	Large Helical Device (LHD)	45
2.7.2	Wendelstein 7-X (W7-X)	46
3	Collision implementation tests	49
3.1	Legendre polynomials	49
3.2	Spitzer problem	53
3.2.1	Formulation	53
3.2.2	Velocity dependence	56
3.2.3	Time dependence	57
3.2.4	Implementation in EUTERPE	57
3.2.5	Results	59
4	Neoclassical transport in EUTERPE	65
4.1	Analytical fluxes in neoclassical regimes	65
4.1.1	Banana regime	65
4.1.2	Pfirsch-Schlüter regime	68
4.1.3	Plateau regime	70
4.1.4	Stellarator $1/\nu$ regime	70
4.2	Results and discussion	71
4.2.1	Implementation in EUTERPE	73
4.2.2	Benchmark	75
4.2.2.1	Stellarator results	81
5	Microinstabilities	83
5.1	Gyrokinetic model for slab ITGs	83
5.2	Toroidal ITGs	87
5.3	Trapped electron mode instabilities	90
5.4	Results and discussion	93

CONTENTS

5.4.1	ITG instabilities with collisions	93
5.4.2	Collisional TEM instabilities in a tokamak	99
5.4.3	Collisional ITG instabilities in LHD	100
5.4.4	Collisional ITG instabilities in W7-X	104
6	Conclusions and Outlook	109
6.1	Conclusions	109
6.2	Outlook	112
	References	115
	Declaration	123
	Curriculum Vitae	125
	Acknowledgements	129

List of Figures

1.1	Binding energy per nucleon. Fusion processes occur to the left side of iron (^{56}Fe). Fission processes, to the right.	2
1.2	Tokamak. The central solenoid provides the plasma current. The toroidal field coils (red) provide the toroidal component of the magnetic field and the vertical field coils (green) are used to further control the position and shape of the plasma.	5
1.3	Left: stellarator with planar (red) and helical (green) coils. Right: stellarator with a set of modular non-planar coils.	6
1.4	Neoclassical particle flux vs. collision frequency. Both axes are displayed in logarithmic scale.	7
2.1	Magnetic coordinates	12
2.2	Gyrating positive ion in a magnetic field.	14
2.3	Incoming velocity \mathbf{v}_{in} of a particle in two coordinates systems: A non-primed system in which z is parallel to B and a primed system in which z' is parallel to \mathbf{v}_{in}	31
2.4	Outcoming velocity \mathbf{v}_{out} of a particle with respect to the incoming velocity \mathbf{v}_{in}	32
2.5	Poloidal projection of orbits. Left: Two different banana orbits that intersect in a point P on a flux-surface ψ . Right: a positively charged passing particle and its shifted trajectory due to drifts.	40
2.6	Magnetic flux surface of LHD at $s = 0.5$. The color indicates the magnitude of the magnetic field. Red color is used for higher values and blue for lower values.	46

LIST OF FIGURES

2.7	Three cross sections of the flux surfaces over a half field period of LHD. From left to right: $\varphi = 0$, $\varphi = 2\pi/40$, $\varphi = 2\pi/20$	46
2.8	Magnetic flux surface of W7-X at $s = 0.5$. The color indicates the magnitude of the magnetic field. Red color is used for higher values and blue for lower values.	47
2.9	Three cross sections of the flux surfaces over a half field period of W7-X. From left to right $\varphi = 0$, $\varphi = 2\pi/20$, $\varphi = 2\pi/10$	47
3.1	Analytical (lines) and numerical (bars) time evolution of δf initially loaded as the first Legendre polynomial (top) and second Legendre polynomial (bottom). The time step was taken as $\Delta t = 0.1 \Omega_*^{-1}$	52
3.2	Collision frequency and electric field dependence of the Spitzer current in a cylinder. The collisionalities correspond to the Pfirsch-Schlüter regime. Solid lines show the analytical values and the symbols show the numerical results.	60
3.3	Saturation of the parallel current with $\nu = 10^{-2} \Omega_*$ and $\bar{E}_{\parallel} = 10^{-2}$ in a tokamak. In red is the current calculated with a constant collision frequency. In green, the current is calculated with a velocity dependent collision frequency. Since the current saturates much faster for the case with constant ν than for the case with velocity dependent ν , time has been multiplied by ten in the case of constant ν for the sake of comparison. The solid lines are the analytical saturation values for currents with a velocity independent (magenta) and velocity dependent (blue) collision frequencies.	62
3.4	Current saturation in a tokamak: analytical (green, magenta) and numerical (red, blue) results ($\bar{E}_{\parallel} = 10^{-2}$ and $\nu = 10^{-6} \Omega_*$).	62
4.1	Time evolution of the normalized radial particle flux in the Pfirsch-Schlüter (left) and banana (right) regime in a tokamak.	73
4.2	Time evolution of the marker distribution along the s direction, when the time step chosen is too large. Here, markers can be seen leaving the flux-surface in LHD.	74

LIST OF FIGURES

4.3	Neoclassical radial particle flux at $s = 0.51$ for a circular tokamak of aspect ratio $A = 5$ obtained with EUTERPE (red), DKES (green) and the analytical values (black). The flux is normalized to the analytical flux in the plateau regime and the collision frequency is normalized to the transit frequency.	80
4.4	Neoclassical radial particle flux at $s = 0.51$ for the LHD stellarator with the <i>standard</i> magnetic configuration for $R = 3.75$ m with no radial electric field $E_r = 0$. Results shown for EUTERPE (blue) and the analytical values (black).	82
5.1	Coordinate system for slab ITGs.	84
5.2	Growth rate dependence on collisionality for different geometries. In this case, LHD was chosen as the example of stellarator geometry.	95
5.3	Evolution in time of the electric field energy for ITGs with and without collisions.	96
5.4	Poloidal cuts for the ITG instability at a time= $2.2 \times 10^4 \Omega_*^{-1}$. On the left: $\nu = 0$. On the right: $\nu = 1 \times 10^{-2} \Omega_*$	96
5.5	Growth rate dependence on η_i . Collisionless case (dotted lines and open symbols). Collisional case (solid lines and filled symbols). The black box indicates the area enlarged and displayed in Fig. 5.6. . .	98
5.6	Detail of Fig. 5.5	98
5.7	Growth rate vs. η_i for a tokamak with aspect ratio $A = 3$ in the collisionless case. The simulations with adiabatic electrons are represented by the blue curve. Simulations with kinetic electrons are depicted in red.	100
5.8	TEM instability growth rate as a function of collisionality for $R/L_{Te} = 0$, $R/L_{Ti} = 3.21$. Blue circles represent the values for $R/L_n = 3.75$. Red diamonds, for $R/L_n = 2.57$	101
5.9	Collisionless ITG mode for LHD. Shown here is the beginning of a period ($\varphi = 0$, left) and the middle of a period ($\varphi = 2\pi/20$, right). Dashed lines represent $s = 0.1, 0.5, 1.0$	102
5.10	Collisional ($\nu = 1 \times 10^{-2} \Omega_*$) ITG mode for LHD at the beginning (left) and the middle (right) of a period.	102

LIST OF FIGURES

5.11	Fourier components for the electrostatic potential of the ITG mode (top) and Fourier spectra (bottom) for the ITG mode in the LHD configuration (shown here with increasing collisionality from left to right: $\nu = 0$, $\nu = 7.0 \times 10^{-3} \Omega_*$, $\nu = 1.0 \times 10^{-2} \Omega_*$).	103
5.12	Collisionality dependence of the growth rate of ITG instabilities in different devices (as in Fig. 5.2) now including W7-X.	105
5.13	Three cross sections of W7-X over a half field period. From left to right $\varphi = 0$, $\varphi = 2\pi/20$, $\varphi = 2\pi/10$. Above: without collisions; below: collisional case with frequency $\nu = 1 \times 10^{-2} \Omega_*$	106
5.14	Fourier components for the electrostatic potential of the ITG mode (top) and Fourier spectra (bottom) for W7-X configuration. Shown here for $\nu = 0$ (left) and $\nu = 1.0 \times 10^{-2} \Omega_*$ (right).	107

Nomenclature

Roman Symbols

B magnetic field

j current density

a minor radius

$A = R_0/a$ aspect ratio

f_s probability distribution function of a species *s*

$k_{\parallel,\perp}$ wave number parallel/perpendicular to the magnetic field

L_B scale length of the magnetic variation

$L_{n,T}$ density/temperature characteristic length

m_s species mass

p plasma pressure

q safety factor

q_s species charge

r radial label in cylindrical coordinates

R_0 major radius

s normalized toroidal flux surface label

Nomenclature

s_0 normalization flux-surface

$v_{\text{th},s} = \sqrt{2T_s/m_s}$ thermal velocity of species s

z height label in cylindrical coordinates

Greek Symbols

α gyroangle

$\epsilon = a/R_0$ inverse aspect ratio

$\eta_i \equiv \frac{d \ln T}{d \ln n}$ ratio between the scale lengths of density and ion temperature gradients

ι rotational transform

κ_n measure of the inverse of density scale length

κ_T measure of the inverse of temperature scale length

$\Omega \equiv ZeB/m$ general cyclotron frequency for a species with mass m and charge Ze

$\Omega_c \equiv ZeB_0/m$ general cyclotron frequency at a reference point

Ω_i ion cyclotron frequency

ψ toroidal flux surface label

$\rho_s \equiv \frac{v_{\perp,s}}{\Omega_s}$ Larmor radius

$\rho_{th} \equiv \frac{v_{\text{th}}}{\Omega_c}$ thermal Larmor radius

θ poloidal angle

φ toroidal angle

Fortiter quo numquam quisquam ire.

Chapter 1

Introduction

This thesis addresses the implementation of collisions in a previously collisionless gyrokinetic code called EUTERPE, and investigates the effect of such collisions on plasma transport and instabilities. In this chapter, some basic concepts about fusion and plasma physics will be introduced as well as the motivation for this work.

1.1 Fusion

In atoms, protons and neutrons are bound together to form the nucleus. This bonding force is called the strong nuclear force, which is one of the fundamental interactive forces in nature. The energy of the bound system (nucleus) is always lower than the energy of its constituents individually (protons and neutrons). This is called *the mass defect* Δm . The binding energy can then be calculated by Einstein's famous equation relating energy to mass: $E = \Delta mc^2$.

This nuclear energy can be obtained by two processes:

- Fission, which transforms a high mass nucleus into new lighter nuclei. These heavy elements are from iron ^{56}Fe to the right in Fig. 1.1. Fission will not be further addressed since it is outside the scope of this work.
- Fusion, which binds light nuclei to form a new heavier nucleus. In Fig. 1.1 these elements corresponds to the ones on the left side of iron.

1. INTRODUCTION

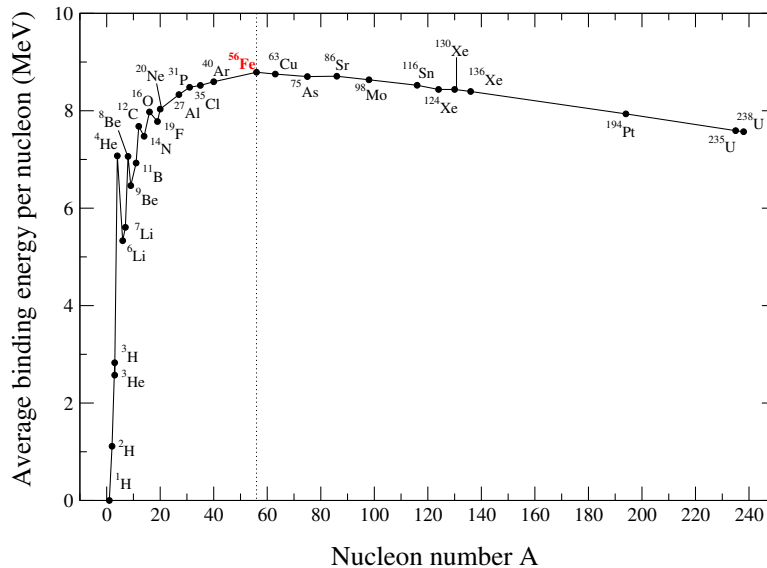


Figure 1.1: Binding energy per nucleon. Fusion processes occur to the left side of iron (^{56}Fe). Fission processes, to the right. Data from [6].

The nuclear binding force, is a short-range force, unlike the Coulomb force, which, at greater distances between the particles dominates the interactions. In order to have fusion, then, it is necessary to overcome the repulsion by the Coulomb force. This condition alone requires extremely high temperatures (~ 500 keV) which would have made fusion in a laboratory practically impossible. Fortunately, it can still be achieved at temperatures below the Coulomb barrier due to quantum tunneling, which allows the nuclei to have a higher probability to undergo fusion reactions at lower temperatures. Also, since the temperature is the average kinetic energy, there will be always particles in the tail of the distribution function that can be in the range of the temperatures needed for fusion.

In nature, fusion occurs naturally in all of the stars in the universe. For stars similar to the Sun, the proton-proton cycle, which transform hydrogen to helium, is the dominant reaction occurring in the core. This kind of fusion, however, occurs very slowly and is therefore unfeasible on Earth. The best candidate for producing energy in a fusion reactor, is the deuterium-tritium (DT) reaction,



1.2 Plasma and magnetic confinement

where D is a deuteron (nucleus of deuterium) which contains one proton and one neutron, T is a triton (nucleus of tritium) containing one proton and two neutrons, ${}^4\text{He}$ is an α -particle (nucleus of Helium) consisting of two protons and two neutrons, and n is a neutron. Its large cross-section at low energies and the abundance of deuterium in water make this choice the most promising for fusion power.

To achieve the density and temperatures needed for ignition (Lawson criterion [7]), it is necessary to confine a thermalized state of deuterons and tritons, as well as electrons. This state of high temperature gas is called plasma.

1.2 Plasma and magnetic confinement

Plasma is a high temperature gas which is composed of positively charged ions, and electrons which exhibit collective behavior. One of its properties is that it is *quasi-neutral*, i.e. local charge concentrations are shielded from the system or device scale length. This happens because electrons surround ions and screen the ion charge. The length scale of this screening is called the *Debye length* and it measures the range of an electric potential in a plasma. Outside the screening zone, the density of positive charges is approximately equal to the density of negative charges.

If the charges are slightly separated (small density perturbation) this causes a restoring electric field to appear. Particles react to this field by oscillating with a frequency called the *plasma frequency*, which is much higher for electrons than for the ions, due to the mass difference.

When a magnetic field is applied, the Lorentz force makes the charged particles in a plasma describe circular and helical orbits around the magnetic field lines. This property leads to the confinement of these particles by the magnetic field and minimizes the contact of the plasma with the device chamber walls. This is necessary since the plasma temperature is far too high for any material to withstand for an extended amount of time. Additionally, if material from the walls leaks into the plasma, this quickly cools down by emission of Bremsstrahlung (deceleration radiation), which is unfavorable, since high temperatures are required for fusion.

1. INTRODUCTION

Some early confinement systems consisted of linear magnetic mirror devices. The problem with such systems is that the losses at the ends were too large to attain the required confinement time. A better approach is a toroidal chamber. A purely toroidal magnetic field, however, is not a good solution, since the non-uniformity and curvature of the magnetic field produces a drift of the charged particles that leads to a charge separation and a related electric field, which finally makes the particles drift radially outwards. To counteract this effect, the magnetic field lines are twisted, so that the charge separation is prevented. The twist of the magnetic field lines is achieved by adding a poloidal component to the toroidal magnetic field.

Two different concepts of toroidal chambers were conceived in the 1950's: the tokamak and the stellarator. They differ mainly by the methods they use to twist the magnetic field.

Tokamak

The tokamak device was first theoretically developed by Tamm and Sakharov, in the Soviet Union, in 1952. The name comes from the Russian *toroidal'naya kamera s magnitnymi katushkami*, which means toroidal chamber with magnetic coils. It works by producing a toroidal magnetic field with external planar coils. The poloidal contribution to the magnetic field is mainly done by the plasma itself, which carries an electric current, produced externally by induction. The toroidal and the poloidal components combined give the magnetic field its twisted shape. Having a current through the plasma helps by contributing to the heating, but it has a main drawback: due to the limited time that the transformer can generate the plasma current, the tokamak can only be operated in a pulsed mode, i.e. not continuously. The plasma current can also induce disruptions, which are short-timed, violent current break-downs, that are detrimental to the device. They can produce mechanical stress and localized heat loads that can damage the machine. A schematic view of the tokamak can be seen in Fig. 1.2.

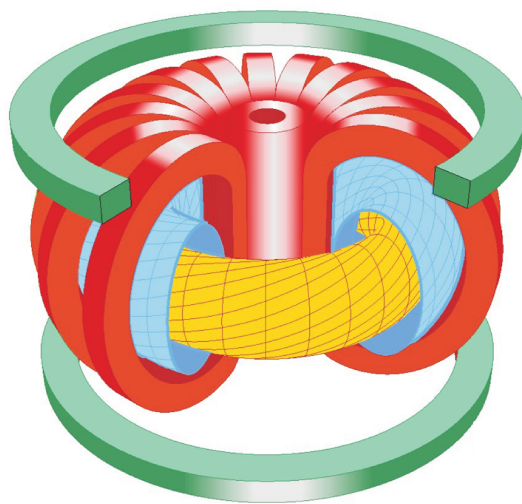


Figure 1.2: Tokamak device diagram. The central solenoid provides the plasma current. The toroidal field coils (red) provide the toroidal component of the magnetic field and the vertical field coils (green) are used to further control the position and shape of the plasma.¹

Stellarator

Around the same time (1951), in Princeton USA, Lyman Spitzer developed the stellarator concept. The magnetic field in this device is produced mainly by the coils; the plasma current is absent (in the absence of plasma pressure) since now the poloidal field component is given also externally. The advantage of this is that there are no disruptions and since the current can be controlled from outside, steady-state (continuous) operation is possible. To achieve this, the shape of the coils must be complex, which causes problems from an engineering point of view. There is no axial symmetry anymore, as in the tokamak, and physics in a stellarator thus becomes fully three dimensional (3D), which poses a great challenge for theoretical calculations, and numerical codes. The short confinement time in early stellarator experiments, made the tokamak more popular, however, due to the problems (mainly disruptions and current drive) the tokamak poses, the stellarator concept has become again a subject of high interest.

Stellarators were first constructed [8] as a set of planar coils with additional

¹© Max-Planck-Institut für Plasmaphysik.

1. INTRODUCTION

helical coils (see Fig. 1.3 (left)). In recent years, they have been built using a set of modular planar and non-planar coils (see Fig. 1.3 (right)), which has proven to be a better way of construction.

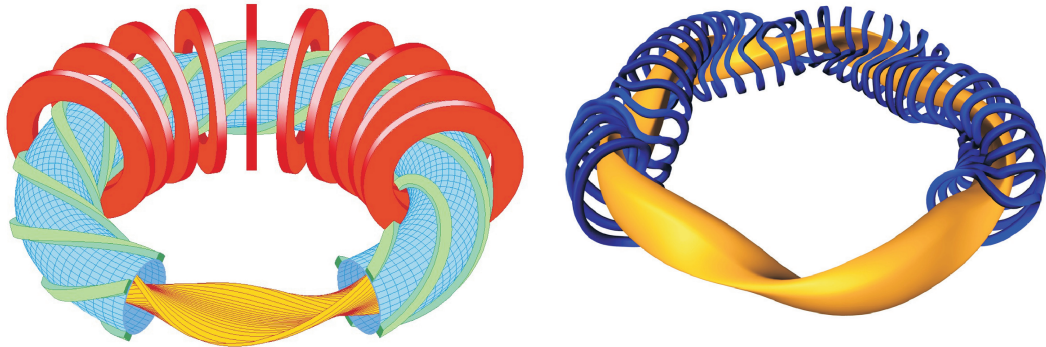


Figure 1.3: Stellarator devices diagrams: left, with planar (red) and helical (green) coils and right is stellarator with a set of modular non-planar coils.²

1.3 Collisional transport

Successful confinement and ignition conditions depend on the density, temperature and confinement time of the plasma. These parameters are limited by different transport processes. Among these processes is the scattering by Coulomb collisions between particles. Collisions induce diffusion which, in the case of charged particles gyrating around a field line, has a step-size of the order of the gyroradius, also called the Larmor radius. This type of diffusion is known as *classical* diffusion. However, in toroidal devices like tokamaks and stellarators, there are not only freely circulating particles but trapped particles as well, which oscillate between local maxima of the magnetic field instead of going around the torus. The trapped orbits that they describe (called banana orbits in a tokamak) have a step size much larger than the Larmor radius, thus, when suffering collisions, diffusion has a greater step-size than classical diffusion. This kind of transport is called *neoclassical transport* [9].

²© Max-Planck-Institut für Plasmaphysik.

Different neoclassical transport regimes can be found depending on the collisionality. In a tokamak, the following can be observed (see Fig.1.4): The *Pfirsch-Schlüter* regime, the *plateau regime* and the *banana regime*.

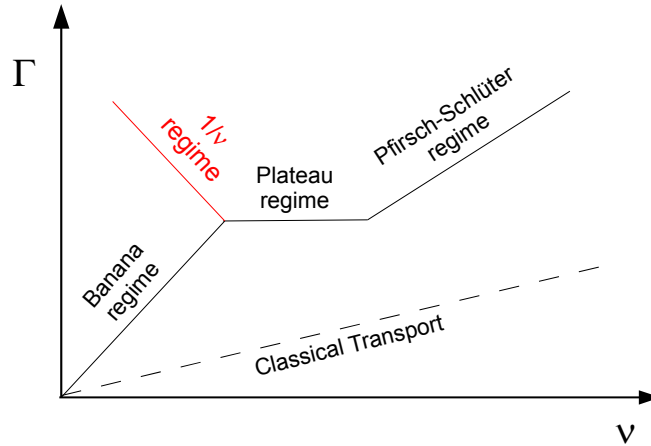


Figure 1.4: Neoclassical particle flux vs. collision frequency. Both axes are displayed in logarithmic scale.

In the Pfirsch-Schlüter regime, the collision frequency is much higher than the bounce frequency of the trapped particles, therefore, trapped and circulating particles cannot complete their orbits and become virtually indistinguishable. In this collisional regime, the diffusion is enhanced, in comparison to the classical diffusion, by a geometrical factor due to the magnetic configuration. In the plateau regime, the collisionality is low enough to allow circulating particle orbits to exist but trapped particle orbits are destroyed by collisions. It is important to note that a completely collision-independent plateau regime can only exist in theory, since the transition between regimes is smooth. In the banana regime, the collision frequency is much smaller than the bounce frequency. In this low-collisionality regime, trapped particles dominate the transport and they are able to complete a banana orbit, therefore enhancing the diffusion.

In a stellarator, this is different, since for low collisionalities, the transport that predominates comes from the helically trapped particles, which describe orbits with a very large radial width that can even reach the chamber walls. Bordering to the

1. INTRODUCTION

plateau regime is therefore a region with transport that is inversely proportional to the collision frequency ($1/\nu$ regime), hence the transport in stellarators is enhanced at lower collisionalities. In modern stellarators, this can be reduced by optimization, as it is the case with Wendelstein 7-X [10], currently under construction in IPP, Greifswald (see Fig. 1.3 (right)).

1.4 Anomalous transport and microinstabilities

Although neoclassical theory explains several phenomena, particle and heat transport measured in existing tokamaks still exceeds the neoclassical prediction. This difference is called *anomalous transport*. Its cause is ascribed to plasma turbulence [11] and, in turn, this is caused by microinstabilities, i.e. instabilities whose perpendicular wavelengths are of the order of the Larmor radius and whose frequencies are much smaller than the gyrofrequency. They are driven by the free sources of energy provided by the non-uniformity of the density and temperature of the plasma.

There are many different types of instabilities [12], but the ones that this work focuses on are the drift instabilities. They can be classified as the following: collisionless and collisional or *dissipative* instabilities, and instabilities where the trapping of the ions and electrons is essential. The most important microinstability is the ion-temperature-gradient (ITG) mode. It is a universal instability since there will always be a temperature gradient present in fusion devices. The ITG mode can be separated into a slab branch [13] and toroidal (curvature-driven) [14] branch. The main electron instability is the trapped-electron-mode (TEM) [15].

1.5 Contribution of this thesis

In classical stellarators, neoclassical effects dominate the transport in the core. In the edge, however, turbulence occurs [16] and can lead to anomalous transport. It is important, then, to have a mathematical tool available to treat neoclassical effects as well as microinstabilities, which can also be affected by collisions.

One of the numerical tools currently under development at IPP, is a gyrokinetic code called EUTERPE. It is a particle-in-cell (PIC [17]) code originally developed

in CRPP, Lausanne [18, 19]. It is the only global gyrokinetic code for computing instabilities in fully 3D magnetic configurations. This code allowed the study of ITG instabilities in quasisymmetric configurations such as QAS3 and HSX [20]. The development of the code was later taken over by IPP, where it was amended to make possible simulations using large Fourier filters [21], which was necessary for geometries such as W7-X. Also, finite pressure effects were included which change the drive of the ITG mode in W7-X [22]. Nonlinear effects were added and benchmarked [23], which allow the observation of zonal flow evolution [24]. Multiple species, electromagnetic effects and kinetic electrons were also implemented, the latter providing the possibility to simulate TEMs.

This work is concerned with the addition of collisions into EUTERPE, which was originally a collisionless code. The code was adapted to perform basic neoclassical calculations (e.g. radial particle flux) and collisional linear simulations of ITGs and TEMs for tokamaks and stellarators (LHD and W7-X configurations).

1.6 Outline

This work is organized as follows: Chapter 2 provides a theory background of gyrokinetics, collisions and neoclassical theory, as well as the theoretical considerations for the collision implementation and numerical schemes. In Chapter 3, the initial tests to check the collision implementation are addressed and discussed. They comprise the recovery of the eigenfunctions of the pitch-angle scattering collision operator (Legendre polynomials) and the determination of the current posed by the *Spitzer problem*. Chapter 4 examines the neoclassical calculations that were performed with the collision implementation. First, analytical calculations for the neoclassical radial particle fluxes are given, and subsequently, the results and benchmarking are shown and discussed for the tokamak as well as for the stellarator cases. Chapter 5 addresses the problem of microinstabilities. The first part of this chapter introduces the models used for the slab and toroidal ITG modes and the TEMs. The second part deals with the results and discusses the effects of collisions on these modes for the different configurations. Finally, Chapter 6 summarizes the findings of this work and provides an outlook.

Chapter 2

Theoretical framework

2.1 Coordinate systems

To study magnetic equilibria in tokamaks and stellarators it is important to work in a coordinate system that suits the toroidal geometry and shape of the magnetic field. In equilibrium, the magnetic field satisfies the following equations:

$$\nabla \cdot \mathbf{B} = 0, \quad (2.1)$$

$$\nabla \times \mathbf{B} = \mu_0 \mathbf{j}, \quad (2.2)$$

$$\mathbf{j} \times \mathbf{B} = \nabla p, \quad (2.3)$$

where \mathbf{B} is the magnetic field, \mathbf{j} is the current density and p is the plasma pressure. For a tokamak configuration, we have axisymmetry. In that case, if we choose a system of cylindrical coordinates (R, φ, z) (see Fig. 2.1) all the quantities we are interested in, will not depend on φ . This is not the case for stellarator geometry, which is not axisymmetric. Hence, it is more convenient to define a different set of coordinates; so-called magnetic coordinates. The magnetic field is then represented as (see, e.g. [25]):

$$\mathbf{B} = \nabla\psi \times \nabla\theta + \nabla\varphi \times \nabla\chi, \quad (2.4)$$

where θ is a poloidal angle and φ is a toroidal angle as shown in Fig. 2.1. The magnetic flux that passes through a poloidal cross-section ($\varphi = \text{constant}$) between

2. THEORETICAL FRAMEWORK

the magnetic axis and some surface $\psi = \text{constant}$ is $2\pi\psi$, therefore ψ is also called the flux surface label. In the same manner, $2\pi\chi$ is the magnetic flux that passes through a surface of $\theta = \text{constant}$, between the magnetic axis and a given flux surface ψ .

A coordinate s is defined to label the different flux surfaces:

$$s = \frac{\psi}{\psi_{\text{edge}}} , \quad (2.5)$$

and goes from 0 (magnetic axis) to 1 (the last flux surface at the edge labeled ψ_{edge}).

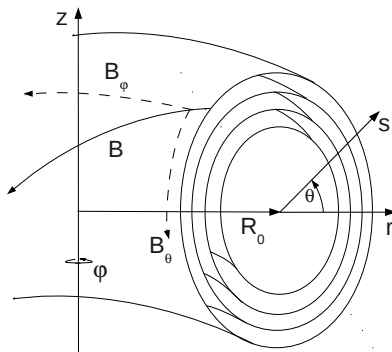


Figure 2.1: Magnetic coordinates

A property of this magnetic coordinate system is that χ is only a function of the flux-surface ψ . Next, we define a quantity that measures the number of poloidal turns a field line makes per toroidal turn:

$$\iota = \frac{d\theta}{d\varphi} = \frac{\mathbf{B} \cdot \nabla \theta}{\mathbf{B} \cdot \nabla \varphi} = \lim_{n \rightarrow \infty} \frac{\theta_n}{2\pi n} . \quad (2.6)$$

where n is the number of toroidal turns and θ_n is the increase of the poloidal angle in each toroidal turn. The quantity ι is called the rotational transform. For historical reasons, tokamak researchers use $q = 1/\iota$ which is called the safety factor, whereas stellarator scientists prefer ι . Using the coordinate χ we can rewrite the rotational transform as

$$\iota(\psi) = \frac{d\chi}{d\psi} . \quad (2.7)$$

2.2 Drift-kinetic and gyrokinetic model

With this definition of ι , the relationship between θ and φ can be written as

$$\theta - \iota\varphi = \text{constant} . \quad (2.8)$$

The advantage of this coordinate system is that the magnetic field lines are straight lines in the (θ, φ) plane.

Additionally, there is a quantity that we will widely use in this work, which is the aspect ratio $A = R_0/a$. It is simply the ratio between the major radius R_0 and the minor radius a (see Fig. 2.1), and is often employed because it defines some of the properties of the devices. The inverse aspect ratio is denoted by $\epsilon = a/R_0$.

2.2 Drift-kinetic and gyrokinetic model

To study particle and wave interactions it is necessary to employ a kinetic approach. In order to do so, a probability distribution function (PDF) is defined $f_s(\mathbf{z}(t), t)$, where $\mathbf{z} = (\mathbf{r}(t), \mathbf{v}(t))$ denotes the phase-space coordinates. This PDF is six-dimensional and gives the number of particles of species s in the phase space volume d^6z at a time t . The collisionless kinetic equation can be written as

$$\frac{\partial f_s}{\partial t} + \frac{\partial}{\partial \mathbf{z}} \cdot (\dot{\mathbf{z}} f_s) = 0 . \quad (2.9)$$

Because of Liouville's theorem, the phase-space volume is conserved in time. Therefore, we can rewrite the equation as

$$\frac{\partial f_s}{\partial t} + \dot{\mathbf{z}} \cdot \frac{\partial f_s}{\partial \mathbf{z}} = 0 . \quad (2.10)$$

It is useful to note that this equation is invariant under transformations $f_s(\mathbf{z}) \rightarrow f_s(\mathbf{w}(\mathbf{z}))$. For plasmas, the equation of motion that describes the evolution of the distribution function for each species, is called the Vlasov equation:

$$\frac{\partial f_s}{\partial t} + \mathbf{v} \cdot \nabla f_s + \frac{q_s}{m_s} (\mathbf{E} + \mathbf{v} \times \mathbf{B}) \cdot \frac{\partial f_s}{\partial \mathbf{v}} = 0 . \quad (2.11)$$

where q_s and m_s are the species charge and mass respectively. This equation is closed by the set of Maxwell equations, which provide the electric and magnetic field from the distribution function f_s . To be able to simplify it, we must first separate the different time and length scales involved.

2. THEORETICAL FRAMEWORK

In fusion plasmas, the gyroradius is much smaller than the length scale of the magnetic field variation $\rho \ll L_B$, therefore we can represent the motion of a particle as a guiding-center (GC) motion plus a fast gyration motion, as shown in Fig. 2.2.

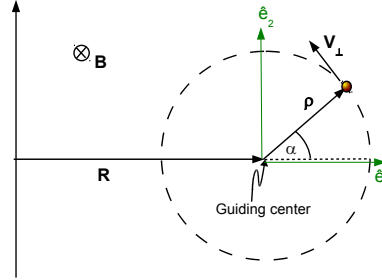


Figure 2.2: Gyrating positive ion in a magnetic field.

Then we can write the position as

$$\mathbf{x} = \mathbf{R} + \boldsymbol{\rho}, \quad (2.12)$$

$$\boldsymbol{\rho} = \frac{v_{\perp}}{\Omega_i} (\cos \alpha \hat{\mathbf{e}}_1 + \sin \alpha \hat{\mathbf{e}}_2), \quad (2.13)$$

where $(\hat{\mathbf{e}}_1, \hat{\mathbf{e}}_2)$ is a pair of unit vectors which are orthogonal and lie in the plane perpendicular to \mathbf{B} , $\Omega_i = q_i B / m_i$ is the ion cyclotron frequency, v_{\perp} is the magnitude of the velocity perpendicular to \mathbf{B} , and α is the gyroangle.

For fields that satisfy $\omega / \Omega_i \ll 1$ and $k_{\perp} \rho_i \ll 1$ where ω is the characteristic frequency of the fluctuation and k_{\perp} is their wave number perpendicular to the magnetic field \mathbf{B} , it is then possible to average over the gyroangle α . In the resulting model, the guiding-center motions appear and the problem is reduced from a 6D system to a 5D system, in which the distribution function is now described in terms of the guiding center coordinates $f_s(\mathbf{R}, v_{\parallel}, \mu)$. The equation describing the evolution of f_s is known as the *drift kinetic equation* (DKE):

$$\frac{df_s}{dt} = \frac{\partial f_s}{\partial t} + \dot{\mathbf{R}} \cdot \frac{\partial f_s}{\partial \mathbf{R}} + \dot{v}_{\parallel} \frac{\partial f_s}{\partial v_{\parallel}} = 0, \quad (2.14)$$

2.2 Drift-kinetic and gyrokinetic model

where the characteristics are the guiding-center trajectories [26, 27]:

$$\dot{\mathbf{R}} = v_{\parallel} \hat{\mathbf{b}} + \frac{1}{B^*} \left(\frac{\mu B + v_{\parallel}^2}{\Omega_i} \hat{\mathbf{b}} \times \nabla B + \frac{v_{\parallel}^2}{\Omega_i} (\nabla \times \mathbf{B})_{\perp} - \mathbf{E} \times \hat{\mathbf{b}} \right), \quad (2.15)$$

$$\begin{aligned} \dot{v}_{\parallel} = & -\mu \left(\hat{\mathbf{b}} + \frac{v_{\parallel}}{B^* \Omega_i} (\nabla \times \mathbf{B})_{\perp} \right) \cdot \nabla B \\ & - \frac{q_i}{m_i} \left(\hat{\mathbf{b}} + \frac{v_{\parallel}}{B^* \Omega_i} \left[\hat{\mathbf{b}} \times \nabla B + (\nabla \times \mathbf{B})_{\perp} \right] \right) \cdot \mathbf{E}, \end{aligned} \quad (2.16)$$

$$\dot{\mu} = 0. \quad (2.17)$$

Here we have defined the magnetic moment per unit mass as $\mu \stackrel{\text{def}}{=} v_{\perp}^2/(2B)$, the unit vector in the direction of the magnetic field $\hat{\mathbf{b}} \stackrel{\text{def}}{=} \mathbf{B}/B$ and the phase space Jacobian as $\mathbf{B}^* = \mathbf{B} + (m/q) v_{\parallel} \nabla \times \hat{\mathbf{b}}$. The terms in Eq. (2.15) are the parallel motion, the ∇B and curvature drifts, the finite β part of the curvature drift and the $\mathbf{E} \times \mathbf{B}$ drift. The terms on the right-hand side of Eq. (2.16) are: the acceleration due to the mirror force, contributions from the finite β effects (terms with $(\nabla \times \mathbf{B})_{\perp}$), the acceleration of free streaming particles due to the electric field and the fourth term which ensures conservation of energy. From Eq. (2.17) it follows that μ is a constant of motion. The DKE is useful to solve problems in transport theory when Coulomb collisions and toroidal magnetic geometries are present (neoclassical transport).

On the other hand, we also want to study microinstabilities and turbulence, which are adequately described by the interaction between the plasma particles and fluctuations with characteristic frequencies much smaller than the ion cyclotron frequency $\omega/\Omega_i \ll 1$, and characteristic wavelengths of the order of the Larmor radius $k_{\perp} \rho \sim O(1)$. An example of such fluctuations are ITGs, which arise due to a gradient in the temperature. To represent these interactions, we need the Larmor radius to be taken into account. The equation that follows from this new approximation is called *gyrokinetic equation*. The modern derivation [28] is done via the phase-space Lagrangian variation method and Lie perturbation theory to obtain an energy-conserving set of gyrokinetic Vlasov-Poisson equations in general geometry. The smallness parameters used in gyrokinetic ordering are the following:

2. THEORETICAL FRAMEWORK

$$\frac{\omega}{\Omega_i} \sim \frac{k_{\parallel}}{k_{\perp}} \sim \frac{e\phi}{T_e} \sim \frac{\rho}{L_n} \sim \frac{\rho}{L_T} \sim O(\epsilon_g) \ll 1, \quad (2.18)$$

where ϕ is the electrostatic potential, $L_n = n/|\nabla n|$ and $L_T = T/|\nabla T|$ are the density and temperature characteristic lengths. An additional small parameter is used: $\rho/L_B \sim O(\epsilon_B)$, with $L_B = B/|\nabla B|$ being the scale length of the magnetic variation.

The drift kinetic equation is used in cases where we have large scale perturbations, i.e. the scale of the Larmor radius is of no concern, such as neoclassical calculations, whereas the gyrokinetic equation is used in problems where the small scale effects (FLR effects) are of interest, such as the study of microinstabilities.

The gyrokinetic equation is similar in form to the drift-kinetic equation. The main difference is that now we treat particles as charged rings with a finite orbit radius. Also, the gyrocenters are affected by the gyroaveraged fields, defined as, e.g.

$$\langle \mathbf{E} \rangle = -\nabla \langle \phi \rangle \approx -\frac{1}{2\pi} \int_0^{2\pi} \nabla_{\mathbf{x}} \phi |_{\mathbf{x}=\mathbf{R}+\boldsymbol{\rho}} d\alpha. \quad (2.19)$$

This procedure allows us to still take into account the finite Larmor radius (FLR) effects. The gyrokinetic equation is still the same as Eqs. (2.14)-(2.17) but now the trajectories are affected by the gyroaveraged electric field; thus, it is necessary to replace the electric field by the gyroaveraged electric field $\mathbf{E} \rightarrow \langle \mathbf{E} \rangle$ in the trajectory Eqs. (2.15) and (2.16). The particle density is given by

$$n_s = \bar{n}_s + \frac{m_s}{q_s} \nabla \cdot \left(\frac{n_{0s}}{B^2} \nabla_{\perp} \phi \right), \quad (2.20)$$

where the gyroaveraged density is determined as

$$\bar{n}_s = \int f_s(\mathbf{R}, v_{\parallel}, v_{\perp}) \delta(\mathbf{R} + \boldsymbol{\rho} - \mathbf{x}) d\mathbf{R} dv. \quad (2.21)$$

Together with quasineutrality:

$$\sum_s q_s n_s = 0, \quad (2.22)$$

this gives an equation for the electrostatic potential. Due to the small mass of the electrons (in comparison to the ions), it is numerically expensive to follow them, therefore the approximation of adiabatic electrons is often used

$$n_e = \frac{n_{0e}\phi}{T_e} . \quad (2.23)$$

2.3 Short description of numerics in EUTERPE

In the following section, a short summary of the numerical features of EUTERPE is given. Since the main interest of this work is to include collisions in the code, we will review in detail only the parts of the numerics that are relevant for the collision implementation. For an in-depth description of the methods used by EUTERPE, beyond the scope of this thesis, we refer to the citations provided.

EUTERPE [20, 22] is a global code that uses the PIC method with a 3D grid for the potentials to solve the set of gyrokinetic equations. The equilibrium magnetic geometry is provided by the magnetohydrodynamic code VMEC [29]. It has the possibility of using different kinetic species such as electrons, ions, fast ions or impurities. It allows for electromagnetic perturbations and includes nonlinear terms. The code uses two systems of coordinates, one of them is a (s, θ^*, φ) system of coordinates, called PEST (Princeton Equilibrium, Stability and Transport) coordinates [30] for the representation of the fields and the other one is cylindrical coordinates (R, φ, z) for the particles. PEST coordinates use the cylindrical angle as the toroidal angle, therefore, both coordinate systems share the same toroidal angle φ . Here, θ^* is the straight-field-line poloidal coordinate. To go from one system to the other, a mapping is performed (see appendix of [20]).

The code utilizes the extraction of a phase factor, which improves the numerics by allowing high wave number modes to be simulated with a coarse grid. It consists of extracting a wave from the potential such that

$$\phi = \tilde{\phi} e^{iS} , \quad (2.24)$$

$$S = M_0 \theta^* + N_0 \varphi , \quad (2.25)$$

where $\tilde{\phi}$ is the amplitude of the wave, S is the phase factor and M_0 and N_0 are the poloidal and toroidal wave number respectively. The phase factor is also

2. THEORETICAL FRAMEWORK

extracted from the distribution function, analogously. This makes it possible to perform linear simulations for large values of M_0 and N_0 . During a run, only some specified wave numbers are extracted from the transformed potential (Fourier filter) in the poloidal and toroidal directions in order to reduce the noise. The Poisson equation is solved by using a finite element discretization for the extracted potential $\tilde{\phi}$. In EUTERPE, B -splines have been chosen as the finite elements. The solution of the field equations is found by using parallel iterative methods for sparse matrices (PETSc library [31, 32, 33]). EUTERPE is parallelized by domain decomposition in φ . It also allows domain cloning which scales almost linearly with the particle number [34].

EUTERPE uses the following quantities for the normalization: the flux-surface where the quantities are normalized s_0 , the mass of the ions m_i , the torus volume V , the number of ions in torus volume $N_{\text{ph},i}$, the temperature of electrons on the chosen flux-surface $T_{e0} = T_e(s_0)$ and the magnetic field at the axis $B_* = B(s = 0, \varphi = 0)$. Then,

$$r_* = \frac{\sqrt{m_i k_B T_{e0}}}{e B_*}, \quad \Omega_* = \frac{e B_*}{m_i}, \quad v_* = \sqrt{\frac{k_B T_{e0}}{m_i}}, \quad (2.26)$$

$$n_{\text{av}} = \frac{N_{\text{ph},i}}{V}, \quad \phi_* = \frac{k_B T_{e0}}{|e|}, \quad E_* = \frac{k_B T_{e0}}{|e| r_*}, \quad (2.27)$$

$$f_* = \frac{n_{\text{av}}}{v_*^3}, \quad j_* = |e| n_{\text{av}} v_*, \quad (2.28)$$

where r_* is used for lengths, Ω_* for frequencies (and its inverse for time), v_* for velocities, n_{av} for densities, ϕ_* for the electric potential, E_* for the electric field, f_* for the distribution functions and j_* for the currents. We define the normalized quantities $\bar{A} = A/A_*$ as barred quantities.

2.4 δf method and two-weight scheme

The PIC method is used in EUTERPE to numerically solve the gyrokinetic equation. It has the advantage that it is straightforward to parallelize but the drawback is that its error due to particle noise, scales only as $\sim \mathcal{O}(1/\sqrt{N})$, where N is the particle number. In order to reduce this noise inherent to the particle

2.4 δf method and two-weight scheme

discretization, EUTERPE uses the δf method [35] in which, for each species, the distribution function is separated into a time-independent background equilibrium and a time-dependent perturbation:

$$f = f_0 + \delta f . \quad (2.29)$$

The advantage over the full- f method is that the markers are only employed to simulate the perturbation, instead of the complete distribution function, making the code more efficient by avoiding the use of markers to represent the Maxwellian. If $\delta f \ll f_0$, the noise is reduced by orders of magnitude compared to the full- f method.

The discretization of δf is performed by

$$\delta f = \sum_{j=1}^N w_j(t) \delta^3(\mathbf{R} - \mathbf{R}_j) \delta(v_{\parallel} - v_{\parallel j}) \delta(\mu - \mu_j) / J_B , \quad (2.30)$$

where $w_j(t)$ is the weight of each marker j , and J_B is the phase space Jacobian, which is B^* .

The collisionless δf method will now be introduced. Next, collisions will be added and we will discuss the importance of using a two-weight scheme for collisional δf simulations.

2.4.1 δf method without collisions

We define the equilibrium distribution function as a local Maxwellian:

$$f_0 = \frac{n_0(s)}{(2\pi)^{3/2} v_{\text{th},i}^3(s)} \exp \left\{ -\frac{1}{2} \frac{v_{\parallel}^2 + v_{\perp}^2}{v_{\text{th},i}^2(s)} \right\} , \quad (2.31)$$

where the density and the temperature (therefore, the thermal velocity) depend only on the flux-surface label s . Here, we introduce the thermal velocity, which is defined as $v_{\text{th},s} = \sqrt{2T_s/m_s}$ for any species s .

We take the drift kinetic equation (2.14) and, using the δf separation of the distribution function, obtain:

$$\frac{d\delta f}{dt} = -\frac{df_0}{dt} = -\dot{\mathbf{z}} \cdot \frac{\partial f_0}{\partial \mathbf{z}} . \quad (2.32)$$

2. THEORETICAL FRAMEWORK

To calculate the relevant quantities such as density, momentum and energy, one needs to take the moments of the distribution function, which can be regarded as expectation values. The Monte Carlo discretization can be performed by using N markers with a marker distribution function $g(\mathbf{z}, t)$. The expectation value is replaced by a mean value as follows [36]

$$E[A] = \int A(\mathbf{z}) \frac{f(\mathbf{z})}{g(\mathbf{z})} g(\mathbf{z}) d\mathbf{z} \approx \frac{1}{N} \sum_{j=1}^N w_j A(z_j), \quad (2.33)$$

where A is an arbitrary function and the weight is now a function of the particle and marker distribution $w_j = f(z_j)/g(z_j)$. By using the method of characteristics [37] and noting that $dg/dt = 0$, the weight evolution can be written as

$$\frac{dw_j}{dt} = -\frac{1}{g_j} \dot{\mathbf{z}}_j \cdot \frac{\partial f_0}{\partial \mathbf{z}_j}. \quad (2.34)$$

In this equation the marker distribution function g_j appears in the denominator. Without collisions this is not a problem at all, since g does not evolve in time and, thus, $g(z_j(t)) = g(z_j(0))$. With collisions, however, the weight evolution of the Monte Carlo markers cannot be easily obtained, since $dg/dt \neq 0$. It is then necessary to use a generalized collisional δf scheme, known as the two-weight scheme [38, 39].

2.4.2 Collisional δf method

If we now take the drift kinetic equation (2.14), add a collision operator on the right hand side, and an arbitrary source term \mathcal{S} , we can use the definition in Eq. (2.29) and obtain:

$$\frac{d}{dt}(f_0 + \delta f) = C(f_0, f_0) + C(f_0, \delta f) + C(\delta f, f_0) + \underbrace{C(\delta f, \delta f)}_{\text{nonlinear}} + \mathcal{S}. \quad (2.35)$$

In the following derivations, we will neglect the nonlinear term. This means that we restrict our model to a linearized collision operator.

Defining the operator D/Dt for an arbitrary function f_A by

$$\frac{Df_A}{Dt} \stackrel{\text{def}}{=} \frac{df_A}{dt} - C(f_A, f_0), \quad (2.36)$$

2.4 δf method and two-weight scheme

we obtain our final equation to be solved:

$$\frac{D\delta f}{Dt} = C(f_0, f_0) + C(f_0, \delta f) + \mathcal{S} - \mathcal{S}_1 , \quad (2.37)$$

where

$$\mathcal{S}_1 \stackrel{\text{def}}{=} \frac{df_0}{dt} . \quad (2.38)$$

The term $C(f_0, \delta f)$ on the right hand side is the back reaction term from the collision operator and ensures that momentum and energy are conserved. This term is complicated, since, for the most used collision operators, the δf term appears inside integrals which cannot be solved analytically. Instead, this part of the operator is usually simplified by using a model [40].

Eq. (2.37) is a second order equation and, therefore the method of characteristics is no longer applicable. What we do instead is not to define the weight in terms of the local δf and g , but rather treat it as an additional dimension of phase space, i.e. we postulate an equation for the marker distribution function in an extended phase space in which we include two new dimensions represented by the weights w_1 and w_2 :

$$\frac{DF}{Dt} + \frac{\partial}{\partial w_1} (A_1 F) + \frac{\partial}{\partial w_2} (A_2 F) = 0 , \quad (2.39)$$

where $F(\mathbf{x}, \mathbf{v}, w_1, w_2, t)$ is the phase space distribution function in the extended phase space. We define the following moments of F :

$$g(\mathbf{x}, \mathbf{v}) \stackrel{\text{def}}{=} \int F dw_1 dw_2 , \quad (2.40a)$$

$$u(\mathbf{x}, \mathbf{v}) \stackrel{\text{def}}{=} \int w_1 F dw_1 dw_2 , \quad (2.40b)$$

$$h(\mathbf{x}, \mathbf{v}) \stackrel{\text{def}}{=} \int w_2 F dw_1 dw_2 . \quad (2.40c)$$

The distribution function of the markers in the non-extended phase space is still represented by g . To solve Eq. (2.39) we take the Kolmogorov forward differential equation [41, 42, 43] (which is equivalent to the Fokker-Planck equation) and obtain an expression in the covariant form for higher dimensions [42, 44] (see especially [41], but note that there the Stratonovich interpretation is used):

$$\frac{\partial}{\partial t} f(x^1, \dots, x^i, \dots, t) = -\frac{1}{\mathcal{J}} \frac{\partial}{\partial x^i} [\mu^i \mathcal{J} f] + \frac{1}{2\mathcal{J}} \frac{\partial^2}{\partial x^i \partial x^j} [(DD^T)^{ij} \mathcal{J} f] . \quad (2.41)$$

2. THEORETICAL FRAMEWORK

It can be shown that the distribution function f corresponds to the following stochastic processes (interpreted as an Ito stochastic differential equation), written also in covariant form:

$$dx^i = \mu^i dt + D^{ij} dW^j , \quad (2.42)$$

where \mathcal{J} is the Jacobian, μ^i are the drift coefficients, D^{ij} is a diffusion matrix and W denotes an n -dimensional Wiener process (standard Brownian motion). If we then use Eq. (2.41) to identify the terms on Eq. (2.39) we obtain the following stochastic trajectories:

$$\frac{d\mathbf{R}}{dt} = \dot{\mathbf{R}} , \quad (2.43a)$$

$$\frac{d\mathbf{v}}{dt} = \dot{\mathbf{v}} + \boldsymbol{\mu}(\mathbf{v}) + \mathbf{D}(\mathbf{v}) \cdot \frac{d\mathbf{W}}{dt} , \quad (2.43b)$$

$$\frac{dw_1}{dt} = A_1 , \quad (2.43c)$$

$$\frac{dw_2}{dt} = A_2 . \quad (2.43d)$$

By taking the moments of Eq. (2.39) we obtain the following set of equations:

$$\frac{Dg}{Dt} = 0 , \quad (2.44)$$

$$\frac{Du}{Dt} - \int A_1 F dw_1 dw_2 = 0 , \quad (2.45)$$

$$\frac{Dh}{Dt} - \int A_2 F dw_1 dw_2 = 0 . \quad (2.46)$$

To obtain these equations the distribution F in the new phase space must be continuous and continuously differentiable and the integral $\int F dw_1 dw_2$ must be bounded, which means that $F \rightarrow 0$ converges sufficiently fast at infinity. Given that F fulfills these properties, as a next step we compare Eq. (2.45) with Eq. (2.37) and identify u with δf . This gives a restriction for A_1 as follows

$$\int A_1 F dw_1 dw_2 = C(f_0, f_0) + C(f_0, \delta f) + \mathcal{S} - \mathcal{S}_1 . \quad (2.47)$$

We choose an Ansatz for A_1 :

2.4 δf method and two-weight scheme

$$A_1 \stackrel{\text{def}}{=} [C(f_0, f_0) + C(f_0, \delta f) + \mathcal{S} - \mathcal{S}_1] \frac{w_2}{h} . \quad (2.48)$$

Accordingly, the weight evolution equation for w_1 , Eq. (2.43c) takes the following form:

$$\frac{dw_1}{dt} = [C(f_0, f_0) + C(f_0, \delta f) + \mathcal{S} - \mathcal{S}_1] \frac{w_2}{h} . \quad (2.49)$$

For A_2 we take the following Ansatz (with a yet to be determined \mathcal{S}_2):

$$A_2 \stackrel{\text{def}}{=} -[C(h, f_0) - \mathcal{S}_2] \frac{w_2}{h} , \quad (2.50)$$

which results in the following equation for h :

$$\frac{Dh}{Dt} = \mathcal{S}_2 - C(h, f_0) \quad \Rightarrow \quad \frac{dh}{dt} = \mathcal{S}_2 . \quad (2.51)$$

Choosing $\mathcal{S}_2 = \mathcal{S}_1 = df_0/dt$ gives $dh/dt = df_0/dt$ which is solved by $h = f_0$. Accordingly, the coupled evolution equations for the weights are:

$$\frac{dw_1}{dt} = \left[C(f_0, \delta f) + C(f_0, f_0) + \mathcal{S} - \dot{\mathbf{z}} \frac{\partial f_0}{\partial \mathbf{z}} \right] \frac{w_2}{f_0} , \quad (2.52)$$

$$\frac{dw_2}{dt} = - \left[C(f_0, f_0) - \dot{\mathbf{z}} \frac{\partial f_0}{\partial \mathbf{z}} \right] \frac{w_2}{f_0} . \quad (2.53)$$

This scheme is the same as proposed by [45] which is also equivalent to the method proposed in [39]. The derivation given here follows [46].

In the linear case, we separate the trajectories $\dot{\mathbf{z}}$ into an unperturbed part $\dot{\mathbf{z}}^0$ and a perturbed part $\dot{\mathbf{z}}^1$. The linearization process makes the quantities $u = \delta f$ and h (see Eqs. (2.45) and (2.46)) evolve only along the unperturbed trajectories, i.e. the operator D/Dt defined in Eq. (2.36), reduces to:

$$\frac{Df_A}{Dt} \stackrel{\text{def}}{=} \frac{d^0 f_A}{dt} - C(f_A, f_0) , \quad (2.54)$$

where d^0/dt denotes the evolution along the unperturbed trajectories. If we additionally choose $\mathcal{S} = d^0 f_0/dt$, we are left with the following linearized equations for the evolution of the weights:

2. THEORETICAL FRAMEWORK

$$\frac{dw_1}{dt} = \left[C(f_0, \delta f) + C(f_0, f_0) - \dot{\mathbf{z}}^1 \frac{\partial f_0}{\partial \mathbf{z}} \right] \frac{w_2}{f_0}, \quad (2.55)$$

$$\frac{dw_2}{dt} = - \left[C(f_0, f_0) - \dot{\mathbf{z}}^0 \frac{\partial f_0}{\partial \mathbf{z}} \right] \frac{w_2}{f_0}. \quad (2.56)$$

We can see that when a local Maxwellian is used as the equilibrium function, the term $C(f_0, f_0)$ vanishes and we have that $\dot{\mathbf{z}}^0 \cdot \partial f_0 / \partial \mathbf{z} = 0$. Then we recover the original one-weight scheme, since the second weight does not evolve.

2.4.3 Initial conditions

We now have to specify the initial conditions for w_1 and w_2 at t_0 . Since we are using a marker discretization we can assume

$$F(\mathbf{z}, w_1, w_2) = \sum_j \delta(\mathbf{z} - \mathbf{z}_j) \delta(w_1 - w_{1,j}) \delta(w_2 - w_{2,j}) \mathcal{J}^{-1}(\mathbf{z}). \quad (2.57)$$

Inserting this into Eqs. (2.40) and taking into account $u = \delta f$ and $h = f_0$, this gives:

$$g = \sum_j \delta(\mathbf{z} - \mathbf{z}_j) \mathcal{J}^{-1}(\mathbf{z}), \quad (2.58a)$$

$$\delta f = \sum_j w_{1,j} \delta(\mathbf{z} - \mathbf{z}_j) \mathcal{J}^{-1}(\mathbf{z}), \quad (2.58b)$$

$$f_0 = \sum_j w_{2,j} \delta(\mathbf{z} - \mathbf{z}_j) \mathcal{J}^{-1}(\mathbf{z}), \quad (2.58c)$$

where j is the index over the markers. It is possible then to obtain the quantities g (marker density), δf and f_0 , by evaluating the sums over certain regions in phase space (*binning*). Accordingly, it is also possible to obtain velocity moments of δf such as the particle number and current density (charge-/current-assignment). It is important to note that the evaluation of f_0 by Eq. (2.58c) can be used as an intrinsic quality measure for the correctness and statistical convergence of the numerical scheme.

Integrating these relations over a small volume V_j centered around \mathbf{z}_j gives out:

$$g(\mathbf{z}_j)V_j = 1 \quad \Rightarrow \quad V_j = \frac{1}{g(\mathbf{z}_j)}, \quad (2.59a)$$

$$\delta f(\mathbf{z}_j)V_j = w_{1,j} \quad \Rightarrow \quad w_{1,j} = \frac{\delta f(\mathbf{z}_j)}{g(\mathbf{z}_j)}, \quad (2.59b)$$

$$f_0(\mathbf{z}_j)V_j = w_{2,j} \quad \Rightarrow \quad w_{2,j} = \frac{f_0(\mathbf{z}_j)}{g(\mathbf{z}_j)}. \quad (2.59c)$$

Since the initial values for g , δf and f_0 are known we get

$$w_{1,j}(t_0) = \frac{\delta f(\mathbf{z}_j, t_0)}{g(\mathbf{z}_j, t_0)}, \quad (2.60)$$

$$w_{2,j}(t_0) = \frac{f_0(\mathbf{z}_j, t_0)}{g(\mathbf{z}_j, t_0)}. \quad (2.61)$$

The two-weight scheme has the problem that its statistical error increases with time, so-called weight spreading. To avoid this issue, it is possible to formulate the collisionless and collisional schemes as a control-variate problem, and improve the scheme by employing an enhanced control-variate approach [46], in which the noise behaves like the δf scheme for early times and is bounded for later times by the noise of the full- f scheme.

2.5 Collision operator

To include collisions in the simulations we first need to find an adequate representation which is simple and also easily testable. So far, we have assumed a general collision operator $C_{ab}(f_a, f_{b0})$, but have not made any physical assumption about its form. As a starting point, we will introduce the Fokker-Planck operator which is the collision operator appropriate for the Coulomb interaction. From this operator, we will only use a simplified version called the pitch-angle-scattering operator, which only alters the direction of the velocity but not its modulus. Afterwards, the implementation in EUTERPE will be discussed.

2. THEORETICAL FRAMEWORK

2.5.1 Fokker-Planck operator

Following the calculations in [47] we write down the collision operator. As a starting point, we take the general Fokker-Planck collision operator for two arbitrary species a and b :

$$C_{ab}(f_a, f_b) = \frac{\partial}{\partial v_k} \left[A_k^{ab} f_a + \frac{\partial}{\partial v_l} (D_{kl}^{ab} f_a) \right], \quad (2.62)$$

where

$$A_k^{ab} \equiv -\frac{\langle \Delta v_k \rangle^{ab}}{\Delta t}, \quad D_{kl}^{ab} \equiv -\frac{\langle \Delta v_k \Delta v_l \rangle^{ab}}{2\Delta t}, \quad (2.63)$$

represent the advection and diffusion terms, respectively. Here, the angular brackets $\langle \dots \rangle$ represent the expectation value of the quantity and Δv is the change in velocity as a result of a collision during a time interval Δt . If we now consider collisions between a species a and a Maxwellian background (species b), then it is useful to employ the Rosenbluth potentials [44, 48]:

$$\varphi_b(\mathbf{v}) \equiv \frac{-1}{4\pi} \int \frac{f_b(\mathbf{v}')}{|\mathbf{v} - \mathbf{v}'|} d^3v', \quad (2.64)$$

$$\psi_b(\mathbf{v}) \equiv \frac{-1}{8\pi} \int |\mathbf{v} - \mathbf{v}'| f_b(\mathbf{v}') d^3v'. \quad (2.65)$$

It is important not to confuse the notation of these potentials with the magnetic coordinates. The Rosenbluth potentials will exclusively be used in this section.

Taking these potentials into account, A_k^{ab} and D_{kl}^{ab} are given by

$$A_k^{ab} = \left(1 + \frac{m_a}{m_b}\right) L^{ab} \frac{\partial \varphi_b}{\partial v_k}, \quad D_{kl}^{ab} = -L^{ab} \frac{\partial^2 \psi_b}{\partial v_k \partial v_l}, \quad (2.66)$$

where $L^{ab} \equiv (q_a q_b / (m_a \epsilon_0))^2 \ln \Lambda$. Here, q_a , q_b , m_a and m_b are the charges and masses of the species a and b respectively, and $\ln \Lambda$ is the Coulomb logarithm. The latter arises from a cut-off introduced in the integral of Coulomb collisions, since particles with impact parameters larger than the Debye sphere radius do not play a role in the collisions due to Debye shielding. With this, the collision operator becomes:

$$C_{ab}(f_a, f_b) = L^{ab} \frac{\partial}{\partial v_k} \left[\left(1 + \frac{m_a}{m_b}\right) \frac{\partial \varphi_b}{\partial v_k} f_a - \frac{\partial}{\partial v_l} \left(\frac{\partial^2 \psi_b}{\partial v_k \partial v_l} f_a \right) \right]. \quad (2.67)$$

2.5 Collision operator

Since we take the species b to be Maxwellian, the distribution function is isotropic and the Rosenbluth potentials only depend on $|\mathbf{v}|$. Therefore:

$$\frac{\partial \varphi_b}{\partial v_k} = \frac{\partial v}{\partial v_k} \frac{\partial \varphi_b}{\partial v} = \frac{v_k}{v} \frac{\partial \varphi_b}{\partial v} = \frac{v_k}{v} \varphi'_b, \quad (2.68)$$

$$\frac{\partial^2 \psi_b}{\partial v_k \partial v_l} = \frac{\partial}{\partial v_k} \left(\frac{v_k}{v} \frac{\partial \psi_b}{\partial v} \right) = W_{kl} \psi'_b + \frac{v_k v_l}{v^2} \psi''_b. \quad (2.69)$$

The primed quantities denote the derivative with respect to v , and W_{kl} is defined as

$$W_{kl} \equiv \frac{v^2 \delta_{kl} - v_k v_l}{v^3}. \quad (2.70)$$

Then,

$$A_k^{ab} = \left(1 + \frac{m_a}{m_b} \right) L^{ab} \frac{v_k}{v} \varphi'_b, \quad D_{kl}^{ab} = -L^{ab} \left(W_{kl} \psi'_b + \frac{v_k v_l}{v^2} \psi''_b \right). \quad (2.71)$$

To write the collision operator we use the following relations:

$$\varphi'_b(v) = \frac{m_b n_b}{4\pi T_b} G(x_b), \quad (2.72)$$

$$\psi'_b(v) = -\frac{n_b}{8\pi} [\phi(x_b) - G(x_b)], \quad (2.73)$$

$$\psi''_b(v) = -\frac{n_b}{4\pi v_{\text{th},b}} \frac{G(x_b)}{x_b}, \quad (2.74)$$

$$A_k^{ab} = -\left(1 + \frac{m_a}{m_b} \right) \frac{\partial D_{kl}^{ab}}{\partial v_l}, \quad (2.75)$$

where $x_b \equiv v/v_{\text{th},b}$ and $v_{\text{th},b}$ is the thermal velocity of species b . $\phi(x)$ is the error function defined as

$$\phi(x) = \frac{2}{\sqrt{\pi}} \int_0^x e^{-y^2} dy, \quad (2.76)$$

and $G(x)$ is the Chandrasekhar function defined as

$$G(x) = \frac{\phi(x) - x\phi'(x)}{2x^2}. \quad (2.77)$$

2. THEORETICAL FRAMEWORK

Finally, taking these definitions and Eqs. (2.62, 2.71, 2.75) we obtain an expression for the collision operator in terms of the Rosenbluth potentials as follows

$$C_{ab}(f_a, f_b) = L^{ab} \frac{\partial}{\partial v_k} \left[\frac{m_a v_k}{m_b v} \varphi'_b f_a - \left(W_{kl} \psi'_b + \frac{v_k v_l}{v^2} \psi''_b \right) \frac{\partial f_a}{\partial v_l} \right]. \quad (2.78)$$

We separate the operator into two parts: an angular part and a part which only modifies the magnitude of the velocity. In order to do so, we rewrite the middle term as

$$\frac{\partial}{\partial v_k} \left(W_{kl} \frac{\partial f_a}{\partial v_l} \right) = \frac{\partial}{\partial \mathbf{v}} \cdot \left[\frac{1}{v} \frac{\partial f_a}{\partial \mathbf{v}} - \frac{\mathbf{v}}{v^3} \left(\mathbf{v} \cdot \frac{\partial f_a}{\partial \mathbf{v}} \right) \right]. \quad (2.79)$$

If we use the definitions of the gradient and divergence in spherical coordinates, we obtain

$$\begin{aligned} \frac{\partial}{\partial v_k} \left(W_{kl} \frac{\partial f_a}{\partial v_l} \right) &= \frac{1}{v^2} \frac{\partial}{\partial v} \left(v \frac{\partial f_a}{\partial v} \right) + \frac{1}{v^3 \sin \theta} \frac{\partial}{\partial \theta} \left(\sin \theta \frac{\partial f_a}{\partial \theta} \right) + \\ &\quad + \frac{1}{v^3 \sin^2 \theta} \frac{\partial^2 f_a}{\partial \varphi^2} - \frac{1}{v^2} \frac{\partial}{\partial v} \left(v \frac{\partial f_a}{\partial v} \right) \\ &= \frac{1}{v^3 \sin \theta} \frac{\partial}{\partial \theta} \left(\sin \theta \frac{\partial f_a}{\partial \theta} \right) + \frac{1}{v^3 \sin^2 \theta} \frac{\partial^2 f_a}{\partial \varphi^2}. \end{aligned}$$

Defining the Lorentz operator as

$$\mathcal{L}(f) \equiv \frac{1}{2} \left[\frac{1}{\sin \theta} \frac{\partial}{\partial \theta} \left(\sin \theta \frac{\partial f}{\partial \theta} \right) + \frac{1}{\sin^2 \theta} \frac{\partial^2 f}{\partial \varphi^2} \right], \quad (2.80)$$

we get

$$\frac{\partial}{\partial v_k} \left(W_{kl} \frac{\partial f_a}{\partial v_l} \right) = \frac{2}{v^3} \mathcal{L}(f_a). \quad (2.81)$$

By using this relation and the vector identity

$$\nabla_v \cdot [\mathbf{v} f(v)] = \frac{1}{v^2} \frac{\partial (v^3 f(v))}{\partial v}, \quad (2.82)$$

we can write the collision operator as

$$C_{ab}(f_a, f_b) = -\frac{2L^{ab}}{v^3} \psi'_b \mathcal{L}(f_a) + \frac{L^{ab}}{v^2} \frac{\partial}{\partial v} \left[v^3 \left(\frac{m_a \varphi'_b}{m_b v} f_a - \frac{\psi''_b}{v} \frac{\partial f_a}{\partial v} \right) \right]. \quad (2.83)$$

Here, the collision operator has two distinct parts: the first term on the right hand side of the equation is the part of the operator which only changes the direction of the velocity of the incoming particles, while the second term affects the magnitude, thus changing the energy of the particles. For the collision implementation in EUTERPE, only the first part of the collision operator in Eq. (2.83) is considered, which is called the pitch-angle scattering operator or Lorentz collision operator.

2.5.2 Pitch-angle scattering

We define the pitch-angle λ as the angle of the velocity vector with the magnetic field

$$\cos \lambda = \frac{v_{\parallel}}{v} . \quad (2.84)$$

To simplify the collision operator, we will take only its angular part and write it as

$$C_{ab}(f_a, f_{b0}) = \nu(v) \mathcal{L}(f_a) , \quad (2.85)$$

where $\nu(v)$ is the deflection frequency between species a and a Maxwellian background of species b . It is important to note that this new collision operator is not momentum conserving.

At this stage, the operator still contains the gyroangle φ . In the transition to drift-kinetics or gyrokinetics, the operator is gyroaveraged. Then the term with the φ derivative disappears but, as a consequence, one gets an additional real space diffusion term which appears when using a gyrocenter coordinate system instead of using a particle phase space coordinate system. This is further explained in references [40] and [49], where a gyrocenter collision operator is derived using the Fokker-Planck method, which includes the diffusion of the gyrocenter. This additional diffusion term is usually neglected, since it describes classical diffusion, which is very small compared to its neoclassical or turbulent counterparts.

The gyro-averaged pitch-angle scattering operator can thus be written as:

$$\mathcal{L} = \frac{1}{2} \frac{\partial}{\partial \xi} (1 - \xi^2) \frac{\partial}{\partial \xi} , \quad (2.86)$$

2. THEORETICAL FRAMEWORK

with $\xi = \cos \lambda$.

Different numerical approaches exist to model collision operators by Monte Carlo methods ([1], [50], [51]). The main goal of each of these numerical methods is to recover the advection and diffusion coefficients statistically as shown in Eq. (2.63). A problem that arises when modeling the pitch-angle as a random number, is that its domain is limited to $\lambda \in [0, \pi]$. When a randomly assigned angle falls out of the domain it needs to either be discarded or recalculated, which can completely change the statistics. To avoid that problem, Takizuka et al. [1] propose the solution of simulating the diffusion process on a spherical shell (in velocity space), therefore, avoiding the boundary problem. The set of spherical coordinates, however, now needs two random numbers to simulate the azimuthal and inclination angles.

The numerical method used to model the collisions in this work is described in [2], which is an improvement of the procedure proposed by Takizuka et al. To further explain this method, let us take two coordinate systems. The first one, $(\mathbf{x}, \mathbf{y}, \mathbf{z})$ has the z -axis parallel to the magnetic field B . The second one, $(\mathbf{x}', \mathbf{y}', \mathbf{z}')$ has the z' -axis parallel to the incoming velocity \mathbf{v}_{in} of a particle. Both systems share the same x -axis and the angle between z and z' is the pitch-angle λ_{in} of the incoming particle before the collision as shown in Fig. 2.3.

Defining $\xi_{\text{in}} = \cos \lambda_{\text{in}}$ and $\sqrt{1 - \xi_{\text{in}}^2} = \sin \lambda_{\text{in}}$, the coordinate systems are related by the pitch-angle as follows

$$\mathbf{x}' = \mathbf{x}, \quad (2.87)$$

$$\mathbf{y}' = \xi_{\text{in}} \mathbf{y} + \sqrt{1 - \xi_{\text{in}}^2} \mathbf{z}, \quad (2.88)$$

$$\mathbf{z}' = -\sqrt{1 - \xi_{\text{in}}^2} \mathbf{y} + \xi_{\text{in}} \mathbf{z}, \quad (2.89)$$

which is a rotation about the x -axis. After one time step, the velocity has changed its angle with respect to the incoming velocity due to a collision. This variation of the angle is denoted by $\Delta\theta$. The magnitude of the velocity, however, remains the same as shown in Fig. 2.4.

Using spherical coordinates, the outgoing velocity can be written in this

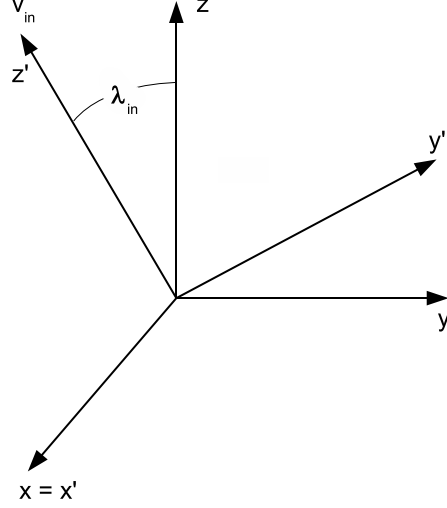


Figure 2.3: Incoming velocity \mathbf{v}_{in} of a particle in two coordinates systems: A non-primed system in which z is parallel to B and a primed system in which z' is parallel to \mathbf{v}_{in} .

system as

$$v_{\text{out},x'} = |v_{\text{in}}| \sin \Delta\theta \cos \varphi, \quad (2.90)$$

$$v_{\text{out},y'} = |v_{\text{in}}| \sin \Delta\theta \sin \varphi, \quad (2.91)$$

$$v_{\text{out},z'} = |v_{\text{in}}| \cos \Delta\theta. \quad (2.92)$$

To know the outgoing pitch-angle of the particle, we need to be in the $(\mathbf{x}, \mathbf{y}, \mathbf{z})$ frame. Using Eqs. (2.87)-(2.89), the outgoing velocity is then:

$$\mathbf{v}_{\text{out}} = v_{\text{out},x'} \mathbf{x}' + v_{\text{out},y'} \mathbf{y}' + v_{\text{out},z'} \mathbf{z}' \quad (2.93)$$

$$\begin{aligned} &= v_{\text{out},x'} \mathbf{x} + v_{\text{out},y'} \left(\xi_{\text{in}} \mathbf{y} + \sqrt{1 - \xi_{\text{in}}^2} \mathbf{z} \right) + \\ &+ v_{\text{out},z'} \left(-\sqrt{1 - \xi_{\text{in}}^2} \mathbf{y} + \xi_{\text{in}} \mathbf{z} \right) \end{aligned} \quad (2.94)$$

$$\begin{aligned} &= v_{\text{out},x'} \mathbf{x} + \left(v_{\text{out},y'} \xi_{\text{in}} - v_{\text{out},z'} \sqrt{1 - \xi_{\text{in}}^2} \right) \mathbf{y} + \\ &+ \left(v_{\text{out},z'} \xi_{\text{in}} + v_{\text{out},y'} \sqrt{1 - \xi_{\text{in}}^2} \right) \mathbf{z}. \end{aligned} \quad (2.95)$$

2. THEORETICAL FRAMEWORK

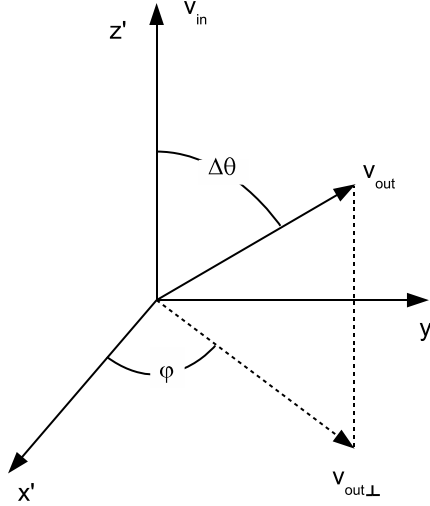


Figure 2.4: Outcoming velocity \mathbf{v}_{out} of a particle with respect to the incoming velocity \mathbf{v}_{in} .

By using the z component of the outcoming velocity and Eqs. (2.90)-(2.92) we can find the outcoming pitch-angle λ_{out} or $\xi_{out} = \cos \lambda_{out}$:

$$v_{out,z} = |v_{out}| \xi_{out} = v_{out,z'} \xi_{in} + v_{out,y'} \sqrt{1 - \xi_{in}^2} \quad (2.96)$$

$$= |v_{in}| \cos \Delta\theta \xi_{in} + |v_{in}| \sin \Delta\theta \sin \varphi \sqrt{1 - \xi_{in}^2}. \quad (2.97)$$

Since the velocity does not change in magnitude after a collision, we have $|v_{in}| = |v_{out}|$. Therefore,

$$\xi_{out} = \sin \Delta\theta \sin \varphi \sqrt{1 - \xi_{in}^2} + \xi_{in} \cos \Delta\theta, \quad (2.98)$$

where φ is a random number taken from a uniform distribution between 0 and 2π , and $\Delta\theta = R\sqrt{2\nu(v)\Delta t}$, where R is a random number from a Gaussian distribution with expectation value 0 and variance 1. It is computationally less expensive not to generate Gaussian distributed random numbers but instead use a uniform distribution with the same expectation value and variance, i.e. we take a random number r from a uniform distribution which goes from 0 to 1 and define $R = 2\sqrt{3}(r - 0.5)$.

2.5 Collision operator

To check that this implementation is consistent, we take the Lorentz operator and rewrite it in Fokker-Planck form as follows

$$\nu \mathcal{L}(f) = \frac{\nu}{2} \frac{\partial}{\partial \xi} (1 - \xi^2) \frac{\partial f}{\partial \xi} \quad (2.99)$$

$$= -\nu \xi \frac{\partial f}{\partial \xi} + \frac{\nu}{2} (1 - \xi^2) \frac{\partial^2 f}{\partial \xi^2} . \quad (2.100)$$

We can immediately relate the quantities with the advection and diffusion terms (Eq. (2.63)). If our scheme is consistent, then it must fulfill the following

$$\frac{\langle \Delta \xi \rangle}{\Delta t} = -\nu \xi , \quad (2.101)$$

$$\frac{\langle \Delta \xi^2 \rangle}{2\Delta t} = \frac{\nu}{2} (1 - \xi^2) . \quad (2.102)$$

In order to confirm this claim, we define $\Delta \xi = \xi_{\text{out}} - \xi_{\text{in}}$ and take the expectation values:

$$\langle \Delta \xi \rangle = \langle \sin \Delta \theta \rangle \langle \sin \varphi \rangle \sqrt{1 - \xi_{\text{in}}^2} + \xi_{\text{in}} \langle \cos \Delta \theta - 1 \rangle , \quad (2.103)$$

$$\begin{aligned} \langle \Delta \xi^2 \rangle &= \langle \sin^2 \Delta \theta \rangle \langle \sin^2 \varphi \rangle (1 - \xi_{\text{in}}^2) + \xi_{\text{in}}^2 \langle (\cos \Delta \theta - 1)^2 \rangle + \\ &+ 2 \langle \sin \Delta \theta \rangle \langle \sin \varphi \rangle \langle \cos \Delta \theta - 1 \rangle \xi_{\text{in}} \sqrt{1 - \xi_{\text{in}}^2} . \end{aligned} \quad (2.104)$$

But $\langle \sin \varphi \rangle = 0$ and $\langle \sin^2 \varphi \rangle = 1/2$ since φ is uniformly distributed. Given that individual collisions do not modify the trajectories significantly, i.e. $\Delta \theta \ll 1$ is assumed, we can perform a Taylor expansion:

$$\sin \Delta \theta \approx \Delta \theta , \quad (2.105)$$

$$\sin^2 \Delta \theta \approx (\Delta \theta)^2 , \quad (2.106)$$

$$\cos \Delta \theta - 1 \approx -\frac{(\Delta \theta)^2}{2} . \quad (2.107)$$

Remembering the definition of $\Delta \theta$ and that $\langle |\Delta \theta|^2 \rangle = 1$, we obtain

2. THEORETICAL FRAMEWORK

$$\langle \Delta \xi \rangle \approx -\xi_{\text{in}} \left\langle \frac{(\Delta \theta)^2}{2} \right\rangle = -\nu \xi_{\text{in}} \Delta t , \quad (2.108)$$

$$\langle \Delta \xi^2 \rangle = \langle (\Delta \theta)^2 \rangle \frac{1}{2} (1 - \xi_{\text{in}}^2) = \nu (1 - \xi_{\text{in}}^2) \Delta t , \quad (2.109)$$

which are consistent with Eqs. (2.101) and (2.102). Given an incoming parallel velocity $v_{\parallel, \text{in}}$ and an incoming perpendicular velocity $v_{\perp, \text{in}}$, the method to obtain the new quantities after a time step, then, consists in calculating ξ and the velocity magnitude by:

$$v_{\text{in}} = \sqrt{v_{\parallel, \text{in}}^2 + v_{\perp, \text{in}}^2} , \quad (2.110)$$

$$\xi_{\text{in}} = \frac{v_{\parallel, \text{in}}}{v_{\text{in}}} , \quad (2.111)$$

and using this to get the outgoing velocities $v_{\parallel, \text{out}}$ and $v_{\perp, \text{out}}$:

$$\xi_{\text{out}} = \sin \Delta \theta \sin \varphi \sqrt{1 - \xi_{\text{in}}^2} + \xi_{\text{in}} \cos \Delta \theta , \quad (2.112)$$

$$v_{\parallel, \text{out}} = v_{\text{in}} \xi_{\text{out}} , \quad (2.113)$$

$$v_{\perp, \text{out}} = \sqrt{v_{\text{in}}^2 - v_{\parallel, \text{out}}^2} . \quad (2.114)$$

2.5.3 Implementation in EUTERPE

For the preliminary tests, the study of ITGs and TEMs and as well as for the neoclassical benchmarking, we used a collision frequency independent of the particle velocity as well as the plasma parameters

$$\nu = \text{constant} . \quad (2.115)$$

The constant is given externally through the input files, therefore, it is not calculated self-consistently from the temperature or the density. During one time step, position and velocities are pushed by a Runge-Kutta method, as if there were no collisions. After the collisionless push, the particles are pushed using the scheme described in Eqs. (2.110)-(2.114). The angles φ and $\Delta \theta$ are assigned random values by a random number generator function that ensures they are independent of each other. Also implemented, but not used, is a more refined

2.5 Collision operator

collision frequency which is consistent with the density and temperature profiles initially provided. It represents a particle scattering model between incoming particles of the species a against a background composed of species b . It follows from using Eq. (2.73) in the first term of Eq. (2.83):

$$\nu_{ab}(v) = \frac{\hat{\nu}_{ab}}{x_a^3} [\phi(x_b) - G(x_b)] , \quad (2.116)$$

with

$$\hat{\nu}_{ab} = \frac{n_b e_a^2 e_b^2 \ln \Lambda}{4\pi \epsilon_0^2 m_a^2 v_{\text{th},a}^3} , \quad (2.117)$$

and

$$x_a \equiv \frac{v}{v_{\text{th},a}} , \quad (2.118)$$

where $\ln \Lambda$ is the Coulomb logarithm. For an electron-ion collision, the Coulomb logarithm is given by the following expression [52] for fusion-relevant temperatures:

$$\ln \Lambda = 32.2 - 1.15 \log_{10}(n_e) + 2.3 \log_{10}(T_e) . \quad (2.119)$$

The temperature is given in eV and the density in m^{-3} [53]. Next, using Eqs. (2.76) and (2.77) we can write:

$$G(x) = \frac{\phi(x)}{2x^2} - \frac{e^{x^2}}{\sqrt{\pi}x} , \quad (2.120)$$

where we have used:

$$\phi'(x) = \frac{2}{\sqrt{\pi}} e^{-x^2} . \quad (2.121)$$

Then the collision frequency can be rewritten as:

$$\nu_{ab}(v) = \frac{\hat{\nu}_{ab}}{x_a^3} \left[\phi(x_b) \left(1 - \frac{1}{2x_b^2} \right) + (\sqrt{\pi}x_b)^{-1} e^{-x_b^2} \right] , \quad (2.122)$$

which is the expression implemented in EUTERPE for the collision frequency that depends on the velocity and plasma parameters.

The collision frequency for each species is:

2. THEORETICAL FRAMEWORK

$$\nu_a \equiv \sum_b \nu_{ab}(v) . \quad (2.123)$$

In the code we have used a rational approximation for the error function ($0 \leq x < \infty$) [54]:

$$\phi(x) = 1 - (a_1 t + a_2 t^2 + a_3 t^3 + a_4 t^4 + a_5 t^5) e^{-x^2} + \epsilon(x) , \quad (2.124)$$

$$t = \frac{1}{1 + px} ,$$

$$|\epsilon(x)| \leq 1.5 \times 10^{-7} ,$$

$$p = 0.32759 , \quad a_1 = 0.25482 ,$$

$$a_2 = -0.28449 , \quad a_3 = 1.42141 ,$$

$$a_4 = -1.45315 , \quad a_5 = 1.06140 .$$

We have only used the the pitch-angle scattering operator. This is a limited model since it does not conserve momentum. Momentum conservation can be implemented using an additional step in which the marker weights are changed by a correction term which results from a simplified model for the momentum conserving part in the collision operator [3, 55, 56]. This item, however, is beyond the scope of this work.

Typical collision frequencies

Table 2.1 shows estimated typical values of the magnitude of the collisionality for different devices. These numbers are given for plasmas in the core and are only approximations, using similar temperatures for the electrons and the ions. At the edge of the devices, the collision frequency can increase by one or two orders of magnitude. In EUTERPE, the collision frequency is normalized to the ion cyclotron collision frequency, which is $\Omega_i \sim 10^8$ - 10^9 s⁻¹ for magnetic fields of order $B \sim 1$ -10 T.

Table 2.1: Estimated values of the collision frequencies for different devices.¹

device	n_e, n_i in m^{-3}	T_e, T_i in eV	ν_{ei} in s^{-1}	ν_{ii} in s^{-1}
JET	10^{19}	10^3	10^4	10^2
MAST, AUG	10^{20}	10^3	10^5	10^3
WEGA	10^{17}	1	10^6	10^4
W7-X, LHD	10^{20}	10^3	10^5	10^3
TJ-II	10^{19}	10^3	10^4	10^2
ITER	10^{20}	10^4	10^3	10^2

Complete Fokker-Planck operator

In the future, and as a next step it would be advisable to incorporate the whole Fokker-Planck collision operator including energy diffusion, into EUTERPE. In the following, we describe briefly how this could be implemented. A good approach is to follow the method proposed in reference [40]. In its simplest form, i.e. without momentum nor energy conservation, the Fokker-Planck collision operator is derived for the EUTERPE velocity coordinate system $(v_{\parallel}, v_{\perp})$.

We take the equation for the collision operator in terms of the Rosenbluth potentials (Eq. (2.78)) and obtain:

$$\begin{aligned}
 C_{ab}(f_a, f_{b0}) = & \frac{\partial}{\partial v_{\parallel}} [v_{\parallel} F f_a] + \frac{1}{v_{\perp}} \frac{\partial}{\partial v_{\perp}} \left[\left(v_{\perp}^2 F + G + 2 \frac{v_{\perp}^2}{v^2} H \right) f_a \right] + \\
 & + \frac{2}{v_{\perp}} \frac{\partial^2}{\partial v_{\perp} \partial v_{\parallel}} \left[\frac{v_{\perp}^2 v_{\parallel}}{v^2} H f_a \right] + \frac{\partial^2}{\partial v_{\parallel}^2} \left[\left(G + \frac{v_{\parallel}^2}{v^2} H \right) f_a \right] + \\
 & + \frac{\partial^2}{(\partial v_{\perp})^2} \left[\left(G + \frac{v_{\perp}^2}{v^2} H \right) f_a \right] + \frac{1}{v_{\perp}^2} \frac{\partial^2}{\partial \varphi^2} [G f_a] ,
 \end{aligned} \tag{2.125}$$

where

¹obtained from [57, 58, 59, 60, 61, 62] and personal communications with P. Drewelow and J. García.

2. THEORETICAL FRAMEWORK

$$F = \frac{L^{ab}n_b}{4\pi v_{\text{th},b}^3} \left(1 + \frac{m_a}{m_b}\right) 2 \frac{G(x_b)}{x_b}, \quad (2.126)$$

$$G = \frac{L^{ab}n_b}{4\pi v_{\text{th},b}} \frac{1}{2x_b} [\phi(x_b) - G(x_b)], \quad (2.127)$$

$$H = \frac{L^{ab}n_b}{4\pi v_{\text{th},b}} \frac{1}{2x_b} [3G(x_b) - \phi(x_b)]. \quad (2.128)$$

These relations are equivalent to the ones in [40]. This expression is still, however, not in the form which is needed to be able to solve it with the Kolmogorov forward differential equation. To avoid this problem, we can choose v_{\perp}^2 instead of v_{\perp} , and then the equation becomes:

$$\begin{aligned} C_{ab}(f_a, f_b) = & \frac{\partial}{\partial v_{\parallel}} [v_{\parallel} F f_a] + \frac{\partial}{\partial v_{\perp}^2} \left[\left(2v_{\perp}^2 F - 4G - 2\frac{v_{\perp}^2}{v^2} H \right) f_a \right] + \\ & + \frac{\partial^2}{\partial v_{\perp}^2 \partial v_{\parallel}} \left[4\frac{v_{\perp}^2 v_{\parallel}}{v^2} H f_a \right] + \frac{\partial^2}{\partial v_{\parallel}^2} \left[\left(G + \frac{v_{\parallel}^2}{v^2} H \right) f_a \right] + \\ & + \frac{\partial^2}{(\partial v_{\perp}^2)^2} \left[\left(4v_{\perp}^2 G + 4\frac{v_{\perp}^4}{v^2} H \right) f_a \right] + \frac{1}{v_{\perp}^2} \frac{\partial^2}{\partial \varphi^2} [G f_a], \end{aligned} \quad (2.129)$$

which has the standard Fokker-Planck form from the reference [40]. The φ dependence goes away after gyroaveraging. Here, as well as in the pitch-angle scattering operator, the space diffusion resulting from the gyroaveraging process, is neglected.

2.6 Neoclassical formalism

Collisions play an important role in magnetized plasmas, especially by affecting its transport properties. Neoclassical theory [9, 63] studies the transport processes of hot, magnetically confined plasmas, which undergo Coulomb collisions in the presence of curvature and gradient drifts. By solving the Fokker-Planck equation, it is possible to calculate the transport coefficients, which linearly relate the flux of particles and energy to the thermodynamic forces (pressure gradient, temperature gradient and electric field). It is in our interest to study these properties, since

for stellarators, in the long-mean-free-path (LMFP) regime, neoclassical transport is dominant [64].

In this work, we studied radial particle transport as a method to test the collision implementation and used EUTERPE to perform simulations of neoclassical transport. Even though longer computing times are required to reach the same steady-state results as mono-energetic codes², a Monte Carlo code has the advantage of providing the possibility of including energy scattering and the electric field, which is not necessarily constant on a flux surface, as is invariably assumed in other codes. This field could be important for impurity transport. In the following sections, some basic concepts about trapped particles and neoclassical transport will be introduced, which is based on the more detailed discussions in Ref. [47, 65, 66].

2.6.1 Particle orbits

Classical diffusion arises when particles with finite gyroradius collide with each other and change their circular orbits, therefore performing a random walk with a length scale of the order of the Larmor radius. If we add an inhomogeneous, curved magnetic field, a part of the particle population can get trapped due to the magnetic mirror effect. Such particles are called *trapped particles* and particles which are not reflected are called *circulating particles* (or *passing particles*). In neoclassical diffusion, as opposed to classical diffusion, the dominant effect comes from these trapped particles, which have a diffusion step length of the order of the trapped orbit width, which is larger than the Larmor radius, hence enhancing the transport compared to classical diffusion. In a tokamak, for example, a curved magnetic field B is present, which is inversely proportional to the major radius R_0 . Therefore, there are trapped particles on the outboard side of the torus, or the Low Field Side (LFS). These trapped particles describe so-called *banana orbits* (see Fig. 2.5(left)). In stellarators, due to a more complex magnetic field geometry, there are helically trapped particles which bounce between local field maxima, in the rippled magnetic field. These helically trapped particles can dominate the neoclassical transport by drifting radially to even leave the toroidal

²A brief explanation of the mono-energetic assumptions is described in section 4.2.2.

2. THEORETICAL FRAMEWORK

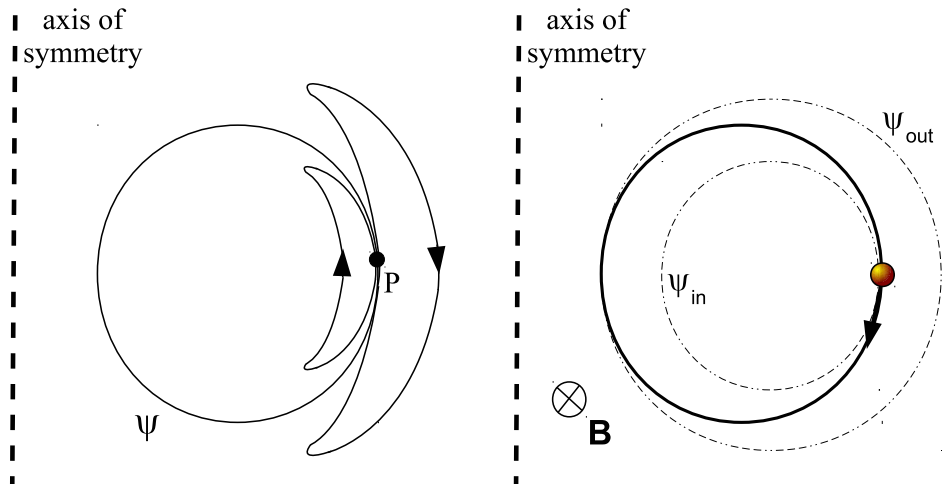


Figure 2.5: Poloidal projection of orbits. Left: Two different banana orbits that intersect in a point P on a flux-surface ψ . Right: a positively charged passing particle and its shifted trajectory due to drifts.

chamber. Collisionality affects the transport by preventing circulating and/or trapped particles from finishing their orbits and by detrapping particles.

2.6.2 Characteristic parameters

In tokamaks, the width of the trapped orbits is called the banana width and can be estimated as

$$\Delta_{\text{ban}} = \frac{\rho_{\theta}}{\sqrt{\epsilon}} = \frac{\rho}{\iota\sqrt{\epsilon}}, \quad (2.130)$$

where $\rho_{\theta} \equiv mv/(qB_{\theta})$ is the poloidal Larmor radius. The rotational transform ι and ϵ are usually lower than one, and therefore the diffusion step size is longer than ρ , thus enhancing the transport. Passing particles, on the other hand, describe complete circulating orbits, but these are displaced from the flux surfaces as shown in Fig. 2.5 (right) due to the gradient and curvature drifts.

Let us consider a particle moving on a flux surface. We define its pitch-angle-like variable $\lambda = v_{\perp}^2 B_0 / (v^2 B)$ where $B_0 = \langle B^2 \rangle^{1/2}$. This quantity should not to be confused with the previously defined pitch angle λ . Here, the angular brackets

$\langle \dots \rangle$ denote a flux-surface average, which is defined as the volume between two neighboring flux surfaces ψ and $\psi + d\psi$,

$$\langle A \rangle \equiv \frac{\int A(\psi, \theta, \varphi) dV}{\int dV} = \frac{\oint A(\psi, \theta, \varphi) \frac{dS}{|\nabla\psi|}}{\oint \frac{dS}{|\nabla\psi|}}. \quad (2.131)$$

where dS is the surface element defined as $dS = \sqrt{g} |\nabla\psi| d\theta d\varphi$ and g is the Jacobian. It is important not to confuse the flux-surface average notation with the gyroaverage. They will be explicitly stated when mentioned, to avoid confusion.

If the energy and magnetic moment are conserved, then we obtain the following condition: if $0 \leq \lambda \leq B_0/B_{min}$ for when a particle is passing, otherwise it is trapped. Here, B_{min} is the minimum value of the magnetic field on the flux-surface (usually located on the outboard side of the surface for a tokamak). Consequently, passing particles have small pitch-angles and circulate freely in the poloidal and toroidal direction following a magnetic field line. If we follow a field line until it closes poloidally, its length is $2\pi R_0/\iota$. Therefore, we can define the poloidal transit time and frequency as:

$$\tau_{tr} = \frac{2\pi R_0}{\iota v_{\parallel}} = \frac{2\pi}{\omega_{tr}}, \quad \omega_{tr} = \frac{\iota v_{\parallel}}{R_0}. \quad (2.132)$$

The displacement of the GC of circulating particles from a flux surface is due to the gradient and curvature drift. If we take the curvature drift at a point in which the pitch angle $\lambda = 0$, then $v_{\parallel} = v$, $v_{\perp} = 0$ and the drift velocity can be written as $v_D = mv^2/(qR_0B_{\varphi})$. The displacement of the particle can, therefore, be expressed as

$$\Delta_{pass} \approx \frac{v_D}{\omega_{tr}} = \rho_{\theta} \epsilon. \quad (2.133)$$

Using Eq. (2.130) we see that $\Delta_{ban} = \Delta_{pass}/\sqrt{\epsilon}$. This means that the displacement from the flux surface is bigger for trapped particles than for passing particles. It is also possible to calculate the bounce time, which is defined as the time it takes for the particle to travel between two reflections:

$$\tau_b \approx 2\pi \frac{\Delta_{ban}}{v_D} = \frac{2\pi}{\omega_{tr}\sqrt{\epsilon}} = \frac{2\pi}{\omega_b}, \quad (2.134)$$

where ω_b is the bounce frequency.

2. THEORETICAL FRAMEWORK

2.6.3 Neoclassical transport equations

In this section expressions for the neoclassical transport are derived, with emphasis on the radial particle flux, which has been implemented in EUTERPE. The calculations follow the steps performed in [47, 55]. We begin by considering a single species plasma in static magnetic field \mathbf{B} . The drift kinetic equation for a distribution function $f(\mathbf{R}, \mu, \mathcal{E}, t)$ in terms of the energy \mathcal{E} is:

$$\frac{\partial f}{\partial t} + \left(v_{\parallel} \hat{\mathbf{b}} + \mathbf{v}_d \right) \cdot \frac{\partial f}{\partial \mathbf{R}} + \dot{\mu} \cdot \frac{\partial f}{\partial \mu} + \dot{\mathcal{E}} \cdot \frac{\partial f}{\partial \mathcal{E}} = C(f). \quad (2.135)$$

For neoclassical phenomena, processes are generally slow, therefore we can assume that the electric and magnetic fields are time-independent, and neglect $\partial f / \partial t$. Consequently, the energy is conserved:

$$\mathcal{E} = \frac{mv_{\parallel}^2}{2} + m\mu B + Zq\phi, \quad (2.136)$$

$$\dot{\mathcal{E}} = 0. \quad (2.137)$$

The magnetic moment (per unit mass) is also a conserved quantity, thus $\dot{\mu} = 0$.

We use the ordering defined by the small parameter $\delta = \rho / R_0$,

$$\frac{\mathbf{v}_D}{v_{\parallel}} \sim \delta \quad (2.138)$$

to perform an expansion of the distribution function in an equilibrium and perturbed part:

$$f = f_0 + f_1. \quad (2.139)$$

The zeroth order equation is

$$v_{\parallel} \nabla_{\parallel} f_0 = C(f_0). \quad (2.140)$$

The solution to this equation is a Maxwellian dependent on the flux surface variable ψ :

$$f_0 = F_m(\psi) = N(\psi) \left(\frac{m}{2\pi T(\psi)} \right)^{3/2} \exp \left\{ -\frac{mv^2/2 + q\phi}{T(\psi)} \right\}. \quad (2.141)$$

This also implies that the electrostatic potential is approximately constant on each flux-surface $\phi \approx \phi_0(\psi)$.

The DKE equation to the first order is written as:

$$v_{\parallel} \nabla_{\parallel} f_1 + \mathbf{v}_d \cdot \nabla f_0 = C(f_1). \quad (2.142)$$

We want to rewrite the second term on the LHS of the above equation. The cross-field drift can be expressed as

$$\mathbf{v}_d \cdot \nabla \psi = v_{\parallel} (\mathbf{b} \times \nabla \psi) \cdot \nabla \left(\frac{v_{\parallel}}{\Omega} \right), \quad (2.143)$$

where $\Omega \equiv ZeB/m$ is the cyclotron frequency and the gradient is taken at a constant energy and μ . Thus, we obtain the following expression for $\mathbf{v}_d \cdot \nabla f_0$,

$$\mathbf{v}_d \cdot \nabla F_m = \left[v_{\parallel} \nabla \left(\frac{v_{\parallel}}{\Omega} \right) \times \mathbf{b} \right] \cdot \nabla \psi \frac{\partial F_m}{\partial \psi} = I v_{\parallel} \nabla_{\parallel} \left(\frac{v_{\parallel}}{\Omega} \right) \frac{\partial F_m}{\partial \psi}, \quad (2.144)$$

where we have used $I = RB_{\varphi}$ and

$$\frac{\mathbf{B} \times \nabla \psi}{B^2} = \frac{I}{B} \mathbf{b} - R \hat{\varphi}, \quad (2.145)$$

where $\hat{\varphi} = R \nabla \varphi$ is the unit vector in the toroidal direction. We define

$$\frac{\partial F_m}{\partial \psi} = -\kappa F_m, \quad (2.146)$$

where

$$\kappa = - \left[\frac{1}{n} \frac{\partial n}{\partial \psi} + \left(\frac{v^2}{v_{\text{th}}^2} - \frac{3}{2} \right) \frac{1}{T} \frac{\partial T}{\partial \psi} \right]. \quad (2.147)$$

In the following we will sometimes write $\kappa_n = -\frac{1}{n} \frac{\partial n}{\partial \psi}$, $\kappa_T = -\frac{1}{T} \frac{\partial T}{\partial \psi}$ as a measure of the inverse of density and temperature scale lengths, respectively. The first order equation (Eq. (2.142)) now becomes:

2. THEORETICAL FRAMEWORK

$$v_{\parallel} \nabla_{\parallel} f_1 - C(f_1) = I \kappa v_{\parallel} F_m \nabla_{\parallel} \left(\frac{v_{\parallel}}{\Omega} \right) . \quad (2.148)$$

From this equation we will later (in Chapter 4) proceed to solve the drift kinetic equation for each collisionality regime (Pfirsch-Schlüter, banana, etc.). Once f_1 is found, it is possible to take moments and obtain the neoclassical fluxes:

$$\Gamma = \langle \mathbf{\Gamma} \cdot \nabla \psi \rangle = \left\langle \int d^3 v \mathbf{v}_{\mathbf{D}} \cdot \nabla \psi f_1 \right\rangle , \quad (2.149)$$

$$Q = \langle \mathbf{Q} \cdot \nabla \psi \rangle = \left\langle \int d^3 v \frac{1}{2} m v^2 \mathbf{v}_{\mathbf{D}} \cdot \nabla \psi f_1 \right\rangle , \quad (2.150)$$

$$j_b = \left\langle \int d^3 v \frac{v_{\parallel}}{h} f_1 \right\rangle , \quad (2.151)$$

where Γ is the radial particle flux, Q is the energy flux and j_b is the bootstrap current [67].

2.6.4 General considerations for EUTERPE

EUTERPE is a code designed to study gyrokinetic instabilities and turbulence. To adapt it to perform neoclassical calculations, several important considerations must be taken into account. First, the self consistent electric fields obtained from solving the gyrokinetic field equation, must be suppressed. A consequence of this is that the density is just the one specified by the profiles, also the electric field (if present) is given externally.

An essential consideration is that the ordering of the DKE (2.14) in the neoclassical picture is different from the gyrokinetic ordering. In neoclassics, as remarked in Eq. (2.138), the drift velocity $\mathbf{v}_{\mathbf{D}}$ (i.e. the ∇B and curvature drifts) is assumed to be of higher order than the parallel velocity, thus the linearized trajectory equations (without external electric fields) are:

$$\dot{\mathbf{R}} = v_{\parallel} \hat{\mathbf{b}} , \quad (2.152)$$

$$\dot{v}_{\parallel} = -\mu \left(\hat{\mathbf{b}} + \frac{v_{\parallel}}{B^* \Omega_i} (\nabla \times \mathbf{B})_{\perp} \right) \cdot \nabla B , \quad (2.153)$$

$$\dot{\mu} = 0 , \quad (2.154)$$

and the evolution of δf is:

$$\frac{d\delta f}{dt} = -\frac{1}{B^*} \left(\frac{\mu B + v_{\parallel}^2}{\Omega_i} \hat{\mathbf{b}} \times \nabla B + \frac{v_{\parallel}^2}{\Omega_i} (\nabla \times \mathbf{B})_{\perp} \right) \cdot \frac{\partial f_0}{\partial \mathbf{R}}. \quad (2.155)$$

The main difference with the full gyrokinetic equation is that the drift velocity does not appear in the zeroth-order trajectory (Eq. (2.152)) and the driving source term in Eq. (2.155) does not contain the gyroaveraged electric field $\langle \mathbf{E} \rangle$, but the curvature and gradient of the magnetic field. From Eq. (2.152) we see that the neoclassical ordering prevents the particles from leaving the flux-surface in lowest order.

These considerations will be used for all the neoclassical numerical calculations with EUTERPE. If other terms are introduced (e.g. an external electric field) they will be explicitly specified in the corresponding section.

2.7 Stellarator geometries used

In the following chapters, results of the collision implementation will be shown. In them, different magnetic configurations are employed. Stellarator geometries are of special interest, due to their complex 3D nature, hence we will briefly describe the types of stellarator devices that will be encountered. Specific details of the magnetic geometries used for the simulations will be given for each configuration.

2.7.1 Large Helical Device (LHD)

The Large Helical Device (LHD) is a heliotron-type superconducting stellarator, located at the National Institute for Fusion Science in Toki, Japan, which has been in operation since 1998. It possesses two continuous superconducting helical coils and three pairs of superconducting poloidal coils. The periodicity of the magnetic field geometry is ten. The major and minor radii of the machine are 3.9 m and 0.6 m, respectively. Its main objective is to investigate steady-state and high-beta plasmas. In Fig. 2.6 the magnetic flux surface of LHD at $s = 0.5$ is shown. In Fig. 2.7 different cross sections from half a field period of LHD are depicted.

2. THEORETICAL FRAMEWORK

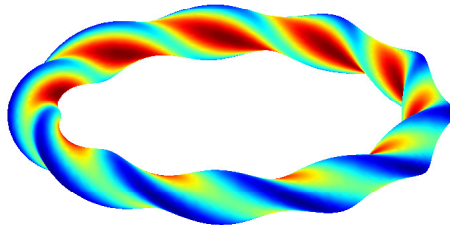


Figure 2.6: Magnetic flux surface of LHD at $s = 0.5$. The color indicates the magnitude of the magnetic field. Red color is used for higher values and blue for lower values.³

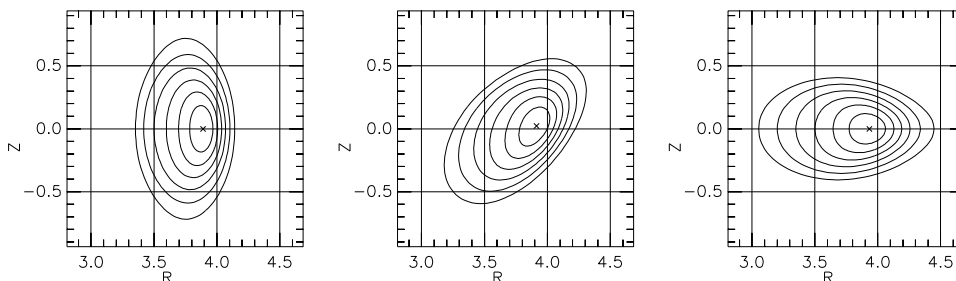


Figure 2.7: Three cross sections of the flux surfaces over a half field period of LHD. From left to right: $\varphi = 0$, $\varphi = 2\pi/40$, $\varphi = 2\pi/20$.³

2.7.2 Wendelstein 7-X (W7-X)

The Wendelstein 7-X (W7-X) stellarator is the latest step in the line of Wendelstein stellarators (W7-A, W7-AS) at the Max-Planck-Institut für Plasmaphysik. It is currently under construction in Greifswald, Germany. It has a modular coil system which is helium-cooled and superconducting. The number of coils is divided into fifty non-planar coils (five different types) and twenty planar coils. The configuration has five field periods and the magnetic field strength will reach up to 3 T. Its major and minor radii are 5.5 m and 0.53 m respectively.

In Fig. 2.8 the magnetic flux surface of W7-X at $s = 0.5$ is shown. In Fig. 2.9 different cross sections from half a field period of W7-X are depicted.

The configuration is the result of an optimization procedure which included the following criteria:

³courtesy of R. Kleiber

2.7 Stellarator geometries used

- small Shafranov shift,
- MHD stability,
- small neoclassical transport, especially in the $1/\nu$ regime,
- small bootstrap current,
- good α -particle confinement.

In the results section of the following chapters we will discuss the collision implementation and its effect on neoclassical transport and microinstabilities for the different geometries: cylinder, tokamak and stellarators.

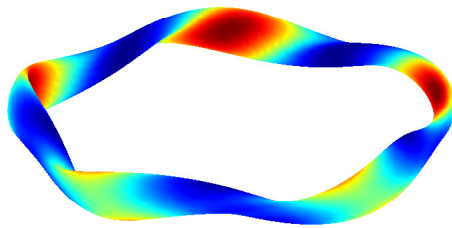


Figure 2.8: Magnetic flux surface of W7-X at $s = 0.5$. The color indicates the magnitude of the magnetic field. Red color is used for higher values and blue for lower values.⁴

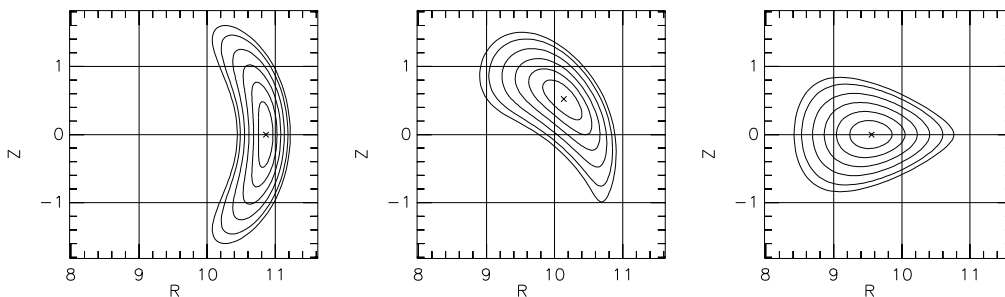


Figure 2.9: Three cross sections of the flux surfaces over a half field period of W7-X. From left to right $\varphi = 0$, $\varphi = 2\pi/20$, $\varphi = 2\pi/10$.⁴

⁴courtesy of R. Kleiber

Chapter 3

Collision implementation tests

Once the collisions were implemented, the logical next step was to test whether the implementation was correct, and if we could recover the physics correctly as well as to estimate the numerical limits of the collisional simulations. Two main tests were performed, which are described in the following sections.

3.1 Legendre polynomials

We want to test collisions added to EUTERPE by using the pitch angle scattering operator. Let us remember from the previous chapter, that the operator only involves the pitch angle, since the magnitude of the electron velocity v is conserved. This makes the operator automatically energy conserving. In this section, we mainly follow the procedure in [2].

A simple initial test was to set the evolution of the guiding center positions equal to zero and let the velocity evolve only according to collisions:

$$\frac{\partial f}{\partial t} = \nu \mathcal{L}(f) , \quad (3.1)$$

where $\mathcal{L}(f)$ is the pitch-angle scattering operator described in Eq. (2.86). As can be noted, this collision operator is equal to the angular part of the Laplace operator, whose eigenfunctions are the Legendre polynomials $P_l(\xi)$ defined by:

$$P_l(\xi) = \frac{1}{2^l l!} \frac{d^l}{d\xi^l} (\xi^2 - 1)^l , \quad (3.2)$$

3. COLLISION IMPLEMENTATION TESTS

since

$$\frac{\partial}{\partial \xi} \left[(1 - \xi^2) \frac{\partial P_l(\xi)}{\partial \xi} \right] = -l(l+1)P_l(\xi) . \quad (3.3)$$

Let us now consider a distribution function in pitch angle space and decompose it over the Legendre polynomials:

$$f(\xi, t) = c_l(t)P_l(\xi) , \quad (3.4)$$

where $c_l(t)$ is the part of the distribution function that carries the time dependence. Substituting $f(\xi, t)$ in Eq. (3.1) gives

$$c_l(t) = c_l(t=0) e^{-l(l+1)\nu t/2} . \quad (3.5)$$

Setting $c_l(t=0) = 1$, we obtain an expression for the time-dependent distribution function:

$$f(\xi, t) = e^{-l(l+1)\nu t/2} P_l(\xi) . \quad (3.6)$$

In the δf method, we separate the distribution function in a local Maxwellian and perturbation part, $f = f_0 + \delta f$. Since the equilibrium part is time-independent and isotropic $\mathcal{L}(f_0) = 0$, f_0 plays no role in the evolution equation. Hence, we only have to deal with the time-dependent part δf .

When the initial loading is such that δf is the eigenmode of the operator, then it evolves as

$$l = 1 \quad \delta f(\xi, t) = e^{-\nu(v)t} \xi , \quad (3.7)$$

$$l = 2 \quad \delta f(\xi, t) = \frac{1}{2} e^{-3\nu(v)t} (3\xi^2 - 1) . \quad (3.8)$$

In Eq. (2.55), it can be seen that if f_0 is a Maxwellian then $C(f_0, f_0) = 0$. Also, we are not considering the back reaction term $C(f_0, \delta f)$, and we chose to consider only collisions as the source term for the evolution of the distribution function, i.e. $\dot{\mathbf{z}}_1 = 0$. Assuming these conditions makes $dw_j/dt = 0$, where j is the marker index. In other words, the weights do not evolve in time. According to Eqs. (2.60) and (2.61), the initial perturbation is:

$$l = 1 \quad w_j(t = 0) = \frac{\delta f(\xi_j, t = 0)}{g(\xi_j, t = 0)} = V_j \xi_j, \quad (3.9)$$

$$l = 2 \quad w_j(t = 0) = \frac{\delta f(\xi_j, t = 0)}{g(\xi_j, t = 0)} = V_j \frac{1}{2} (3 \xi_j^2 - 1). \quad (3.10)$$

We tested this case in EUTERPE by changing the initialization of the weights according to Eqs. (3.9) and (3.10) and switching off the evolution of the real space trajectories and the parallel velocity, leaving only the time evolution of the distribution function as in Eq. (3.1). This means that the parallel and perpendicular velocity are only pushed according to Eqs. (2.112-2.114). We measured the δf evolution by binning the weights into ξ bins. Fig. 3.1 (top) shows the initially loaded δf as the first Legendre polynomial and its evolution with a time step $\Delta t = 0.1 \Omega_*^{-1}$. We can see that as times advances, δf drops, in agreement with the exponential decay behavior described in Eq. (3.7). If we now load the initial δf as the second Legendre polynomial, shown in Fig. 3.1 (bottom) we see that the numerical results are also in good agreement with the theoretical prediction done in Eq. (3.8). We also used different time steps of the same order of magnitude with no important changes in the results, which means that the time step chosen is adequate to resolve the collisional effects on δf . It is relevant to note that this scheme is of first order, therefore, when combined with previously implemented higher order methods used for collisionless particle pushing, such as Runge-Kutta (4th order), the numerical errors will be given by the collisional pushing scheme.

3. COLLISION IMPLEMENTATION TESTS

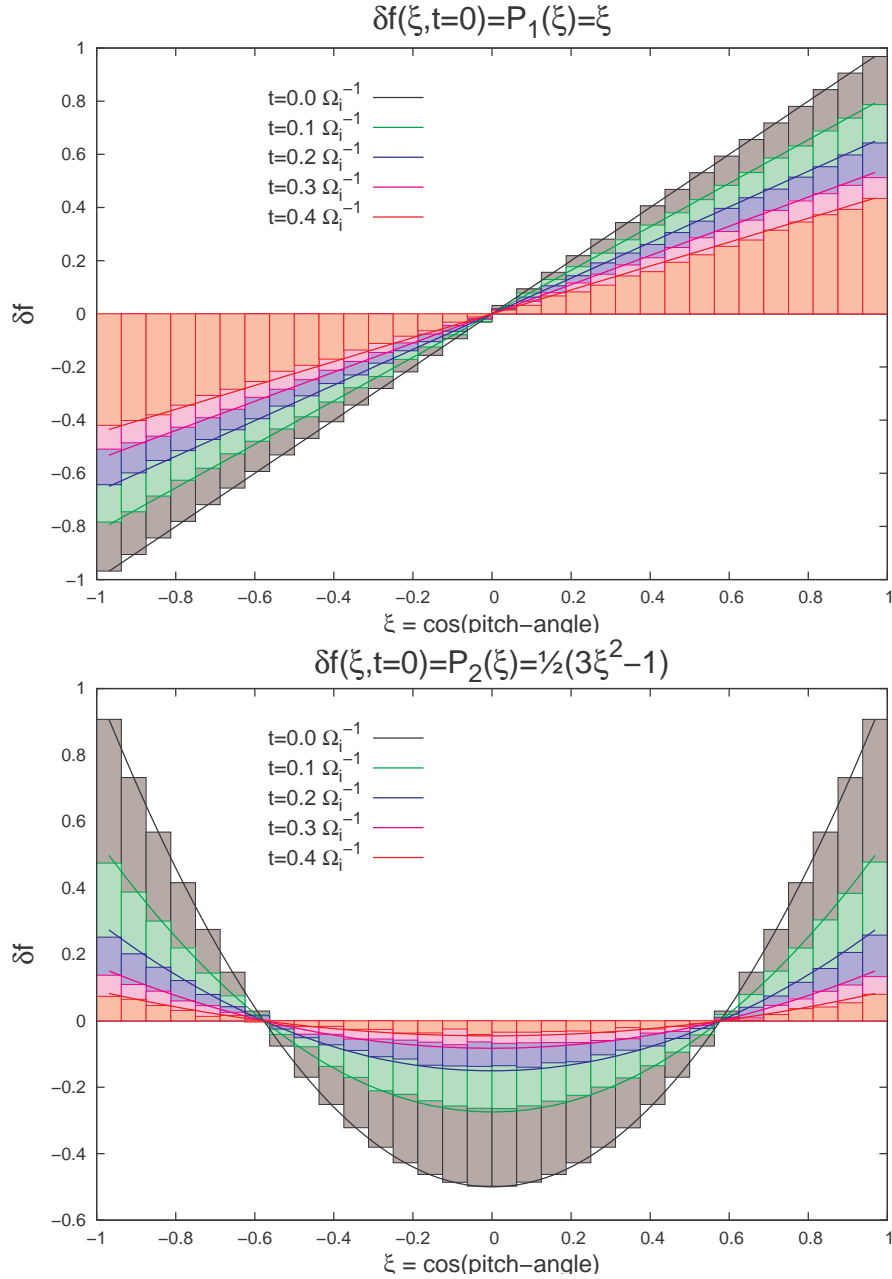


Figure 3.1: Analytical (lines) and numerical (bars) time evolution of δf initially loaded as the first Legendre polynomial (top) and second Legendre polynomial (bottom). The time step was taken as $\Delta t = 0.1 \Omega_*^{-1}$.

3.2 Spitzer problem

3.2.1 Formulation

We now consider a single species plasma with collisions and an external electric field in a tokamak. To model the collisions we again use the pitch angle scattering operator.

We use the same approximations as we did for the neoclassical theory in the previous chapter, but now take the electric field into account. We follow the derivation from [47].

The zeroth order equation (Eq. (2.140)) remains the same, therefore the solution for f_0 is a Maxwellian. The first order drift kinetic equation (Eq. (2.142)) in the neoclassical approximation with the added parallel electric field becomes:

$$v_{\parallel} \nabla_{\parallel} f_1 + \mathbf{v}_{\mathbf{d}} \cdot \nabla f_0 + \frac{eE_{\parallel}}{m} \frac{\partial f_0}{\partial v_{\parallel}} = C(f_1), \quad (3.11)$$

where E_{\parallel} is considered to be of order δ . Currently, we are only interested in the parallel transport, hence for simplicity we have chosen $\kappa_{n,T} = -\partial \ln(n, T)/\partial \psi = 0$, i.e. we use flat density and temperature profiles. Using this, the first order equation becomes:

$$v_{\parallel} \nabla_{\parallel} f_1 - \frac{eE_{\parallel}}{m} \frac{\partial f_0}{\partial v_{\parallel}} = C(f_1), \quad (3.12)$$

which is often referred to as the *Spitzer problem* [68]. Knowing that f_0 is a Maxwellian, one obtains

$$v_{\parallel} \nabla_{\parallel} f_1 - \frac{ev_{\parallel} E_{\parallel}}{k_B T} f_0 = C(f_1). \quad (3.13)$$

We use the Lorentz operator in the following form:

$$\mathcal{L} = \frac{2hv_{\parallel}}{v^2} \frac{\partial}{\partial \lambda} \lambda v_{\parallel} \frac{\partial}{\partial \lambda}, \quad (3.14)$$

with

$$h \equiv \frac{B_0}{B}, \quad \lambda = \frac{v_{\perp}^2 B_0}{v^2 B} \quad \text{and} \quad v_{\parallel} = v(1 - \lambda/h)^{1/2}. \quad (3.15)$$

Here the magnetic field normalization has been defined as $B_0 \equiv \langle B^2 \rangle^{1/2}$, see Eq. (2.131).

3. COLLISION IMPLEMENTATION TESTS

We now perform a subsidiary expansion on f_1 in the smallness of the collision frequency. For the low collisionality regime (banana regime) we have that $\nu_* = \nu_{\text{eff}}/\omega_b \ll 1$, where $\nu_{\text{eff}} = \nu/\epsilon$. Applying this subsidiary expansion, one can define:

$$\frac{f_1^{(1)}}{f_1^{(0)}} \sim \frac{\nu_{\text{eff}}}{\omega_b}. \quad (3.16)$$

We neglect the higher order terms

$$v_{\parallel} \nabla_{\parallel} f_1^{(0)} + v_{\parallel} \nabla_{\parallel} f_1^{(1)} - \frac{ev_{\parallel} E_{\parallel}}{k_B T} f_0 = C(f_1^{(0)}) + \underbrace{C(f_1^{(1)})}_{\text{higher order}}, \quad (3.17)$$

and by this new ordering, we obtain

$$v_{\parallel} \nabla_{\parallel} f_1^{(0)} = 0, \quad (3.18)$$

$$v_{\parallel} \nabla_{\parallel} f_1^{(1)} - \frac{ev_{\parallel} E_{\parallel}}{k_B T} f_0 = C(f_1^{(0)}). \quad (3.19)$$

To find $f_1^{(0)}$ we multiply Eq. (3.19) by B/v_{\parallel} and take the flux-surface average. The term with the parallel gradient vanishes and we are left with:

$$\left\langle -\frac{eB E_{\parallel}}{k_B T} f_0 \right\rangle = \left\langle \frac{B}{v_{\parallel}} C(f_1^{(0)}) \right\rangle. \quad (3.20)$$

Remembering that $C(f_1^{(0)}) = \nu \mathcal{L}(f_1^{(0)})$ then we have

$$\frac{2B_0}{v^2} \frac{\partial}{\partial \lambda} \lambda \langle v_{\parallel} \rangle \frac{\partial}{\partial \lambda} f_1^{(0)} = -\frac{e}{\nu k_B T} f_0 \langle E_{\parallel} B \rangle, \quad (3.21)$$

$$\frac{\partial}{\partial \lambda} \lambda \langle v_{\parallel} \rangle \frac{\partial}{\partial \lambda} f_1^{(0)} = -\frac{v^2}{2} \underbrace{\frac{e}{\nu k_B T}}_S f_0 \left\langle \frac{E_{\parallel}}{h} \right\rangle. \quad (3.22)$$

Eq. (3.22) can be solved by integrating twice over λ . The function $f_1^{(0)}$ vanishes in the trapped domain, so we only need to solve $f_1^{(0)}$ in the passing domain, $0 \leq \lambda \leq \lambda_c$. Here we have defined $\lambda_c = B_0/B_{\text{max}}$ as the trapped-passing boundary and $B_{\text{max}}(\psi)$ is the maximum magnetic field strength on the flux surface ψ . The solution for $f_1^{(0)}$ is then

$$f_1^{(0)} = H(\lambda_c - \lambda) V_{\parallel} S f_0 \left\langle \frac{E_{\parallel}}{h} \right\rangle, \quad (3.23)$$

where

$$V_{\parallel} = \frac{v^2}{2} \int_{\lambda}^{\lambda_c} \frac{d\lambda'}{\langle v_{\parallel}(\lambda') \rangle} = \frac{\sigma v}{2} \int_{\lambda}^{\lambda_c} \frac{d\lambda'}{\langle \sqrt{1 - \lambda'/h} \rangle}. \quad (3.24)$$

Here we have defined $\sigma = v_{\parallel}/|v_{\parallel}|$. H is the Heaviside step function.

Since $f_1^{(0)}$ is now known, we can calculate the parallel Spitzer current:

$$j_{\parallel} = e \int v_{\parallel} f_1^{(0)} d^3v = e \left\langle \frac{E_{\parallel}}{h} \right\rangle \int S v_{\parallel} H V_{\parallel} f_0 d^3v. \quad (3.25)$$

If we use the volume element as

$$d^3v = \sum_{\sigma=\pm 1} \frac{\pi v^3 B}{B_0 v_{\parallel}} dv d\lambda, \quad (3.26)$$

then the current becomes

$$j_{\parallel} = e \left\langle \frac{E_{\parallel}}{h} \right\rangle \frac{\pi}{h} \sum_{\sigma} \int S H V_{\parallel} f_0 v^3 dv d\lambda \quad (3.27)$$

$$= e \left\langle \frac{E_{\parallel}}{h} \right\rangle \frac{\pi}{h} \int_0^{\infty} S v^4 f_0 dv \int_0^{\lambda_c} d\lambda \int_{\lambda}^{\lambda_c} \frac{d\lambda'}{\langle \sqrt{1 - \lambda'/h} \rangle}. \quad (3.28)$$

If we assume that $\nu = \text{constant}$, i.e. independent of the velocity, then

$$j_{\parallel} = e S \left\langle \frac{E_{\parallel}}{h} \right\rangle \frac{\pi}{h} \frac{3}{8\pi} n v_{\text{th}}^2 \int_0^{\lambda_c} \frac{\lambda d\lambda}{\langle \sqrt{1 - \lambda/h} \rangle}. \quad (3.29)$$

Defining the effective fraction of trapped particles [69] f_t as

$$f_t = 1 - \frac{3}{4} \int_0^{\lambda_c} \frac{\lambda d\lambda}{\langle \sqrt{1 - \lambda/h} \rangle} = 1 - f_c, \quad (3.30)$$

where f_c is the fraction of circulating particles, and replacing S , the parallel current can be written as

3. COLLISION IMPLEMENTATION TESTS

$$j_{\parallel} = \frac{e^2 n}{\nu m} (1 - f_t) \left\langle \frac{E_{\parallel}}{h} \right\rangle \frac{1}{h}. \quad (3.31)$$

Taking the flux-surface average and assuming E_{\parallel} is constant, we obtain

$$\langle j_{\parallel} \rangle = \frac{e^2 n E_{\parallel}}{\nu m} (1 - f_t) \left\langle \frac{1}{h} \right\rangle^2. \quad (3.32)$$

If the aspect ratio is large, then $\epsilon \rightarrow 0$. Consequently, and from the definition of h in Eq. (3.15), we have that $h \approx 1 + O(\epsilon)$. Then $\langle 1/h \rangle \approx 1$ and the final expression for the parallel current in the **banana regime** is:

$$\boxed{\langle j_{\parallel} \rangle = \frac{e^2 n E_{\parallel}}{\nu m} (1 - f_t)}. \quad (3.33)$$

In the **Pfirsch-Schlüter regime**, the current can be again calculated resulting in

$$\boxed{\langle j_{\parallel} \rangle = \frac{e^2 n E_{\parallel}}{\nu m}}. \quad (3.34)$$

Due to the high collisionality, trapped particles play no role in this case, which is equivalent to the case in which the geometry is a cylinder.

3.2.2 Velocity dependence

We make the collision frequency dependent on the velocity $\nu \rightarrow \tilde{\nu}/v^3$, where $\tilde{\nu}$ represents the quantity $\hat{\nu}_{ab} v_{\text{th}}^3$, where $\hat{\nu}_{ab}$ is given in Eq. (2.117). Replacing this in the calculation of the current, we get that the first integral in Eq. (3.28) is no longer $\int_0^{\infty} v^4 f_0 dv = \frac{3}{8\pi} n v_{\text{th}}^2$, but $\int_0^{\infty} v^7 f_0 dv = \frac{3}{\pi^{3/2}} n v_{\text{th}}^5$. Then the parallel current becomes

$$\langle j_{\parallel} \rangle = \frac{8v_{\text{th}}^3}{\sqrt{\pi}} \frac{e^2 n E_{\parallel}}{\tilde{\nu} m} (1 - f_t) \left\langle \frac{1}{h} \right\rangle^2. \quad (3.35)$$

In the Pfirsch-Schlüter regime it becomes

$$\boxed{\langle j_{\parallel} \rangle = \frac{8v_{\text{th}}^3}{\sqrt{\pi}} \frac{e^2 n E_{\parallel}}{\tilde{\nu} m}}. \quad (3.36)$$

3.2.3 Time dependence

We now calculate the time-dependent parallel current in cylindrical geometry.

To solve the time-dependent Spitzer problem for a cylinder, then we need to find the time-dependent Spitzer function f_s , which now solves the following equation:

$$\frac{\partial f_s}{\partial t} + \frac{eE_{\parallel}}{m} \frac{\partial f_0}{\partial v_{\parallel}} = C(f_s), \quad (3.37)$$

which is equivalent to

$$\frac{\partial f_s}{\partial t} - \nu \mathcal{L}(f_s) = \frac{ev_{\parallel} E_{\parallel}}{k_B T} f_0. \quad (3.38)$$

If we assume that the Spitzer function is proportional to the parallel velocity $f_s = v_{\parallel} g(\mathbf{R})$, then $\mathcal{L}(f_s) = -f_s$ and

$$\frac{\partial f_s}{\partial t} + \nu f_s = \frac{ev_{\parallel} E_{\parallel}}{k_B T} f_0. \quad (3.39)$$

The solution to the full equation is then, with zero initial conditions

$$f_s = \frac{ev_{\parallel} E_{\parallel}}{\nu k_B T} f_0 [1 - \exp(-\nu t)]. \quad (3.40)$$

We use this solution to obtain the current (in the cylindrical case):

$$\boxed{\langle j_{\parallel} \rangle = \frac{e^2 n E_{\parallel}}{\nu m} [1 - \exp(-\nu t)]}. \quad (3.41)$$

3.2.4 Implementation in EUTERPE

To comply with Eqs. (2.152-2.154), we load the particles in one flux surface and suppress the radial spatial drifts. We take only one flux surface because it is numerically less expensive, since it takes a great number of particles to reduce the statistical noise. For the diagnostic quantities it is then important to keep in mind that instead of using the average over the whole volume to determine the density, the flux-surface integral should be used. In our case E_{\parallel} is fixed and externally given.

3. COLLISION IMPLEMENTATION TESTS

The equations of motion, together with the equation for δf are:

$$\frac{d\mathbf{R}}{dt} = v_{\parallel} \hat{\mathbf{b}}, \quad (3.42a)$$

$$\frac{dv_{\parallel}}{dt} = -\mu \hat{\mathbf{b}} \cdot \nabla B \quad \text{with trapped particles,} \quad (3.42b)$$

$$\frac{dv_{\parallel}}{dt} = 0 \quad \text{without trapped particles,} \quad (3.42c)$$

$$\frac{d\delta f}{dt} = -f_0 \frac{ev_{\parallel} E_{\parallel}}{T}. \quad (3.42d)$$

The current in Eq. (3.34) is expressed in normalized quantities as the following:

$$\langle \bar{j}_{\parallel} \rangle = \frac{\bar{n}}{\bar{\nu}} \bar{E}_{\parallel}. \quad (3.43)$$

In this case the normalized density is always $\bar{n} = 1$. Then, for the Pfirsch-Schlüter regime we get:

$$\boxed{\langle \bar{j}_{\parallel} \rangle = \frac{\bar{E}_{\parallel}}{\bar{\nu}}}. \quad (3.44)$$

For the banana regime we need to know the effective fraction of trapped particles. This is given by expanding Eq. (3.30) for a small inverse aspect ratio ϵ and circular flux surfaces:

$$f_t(r) \approx 1.469 \sqrt{\frac{r}{R}} \left(1 - 0.325 \frac{r}{R} \right), \quad (3.45)$$

but $r = a\sqrt{s}$, therefore,

$$f_t(s) \approx 1.469 \sqrt{\epsilon} \sqrt[4]{s} (1 - 0.325 \epsilon \sqrt{s}). \quad (3.46)$$

Then the current is:

$$\boxed{\langle \bar{j}_{\parallel} \rangle = \frac{\bar{E}_{\parallel}}{\bar{\nu}} (1 - f_t(s))}. \quad (3.47)$$

For the velocity dependent collision frequency in the Pfirsch-Schlüter regime, we perform the normalization and take into account that the normalized thermal velocity in EUTERPE is $v_* = \sqrt{T/m} = v_{\text{th}}/\sqrt{2}$, then

$$\langle \bar{j}_{\parallel} \rangle = \frac{16\sqrt{2}}{\sqrt{\pi}} \frac{v_*^3 \bar{E}_{\parallel}}{\tilde{\nu}}, \quad (3.48)$$

where here, $\tilde{\nu}$ is a constant quantity given from the input file.

3.2.5 Results

In this section we use two different geometries for the simulations: a cylinder and a tokamak. The cylinder configuration had a radius of $a = 0.4$ m and the tokamak geometry had an aspect ratio of $A = 5$ with a major radius of $R_0 = 8$ m.

As a first test, the parallel current in a cylinder is calculated; a scan for different normalized external electric fields $\bar{E} = 0.01-0.04$ is performed. The collisionality is chosen to be $\nu = 10^{-2} \Omega_*$. The number of particles used is $N = 10^5$ and the time step is $\Delta t = 0.5$. The results are shown in Fig. 3.2 for different collision frequencies. Solid lines represent the analytical values calculated from Eq. (3.44) and the symbols show the numerical results.

The next test consisted in adding the velocity dependence to the collision frequency in the code and comparing the numerical results (in the Pfirsch-Schlüter regime) with the analytical saturation value of the current expressed in Eq. (3.48). For this we considered a tokamak configuration and took the following parameter values: $\bar{E} = 10^{-2}$, $\nu = 10^{-2} \Omega_*$, $\Delta t = 10$ and $N = 10^5$. Fig. 3.3 shows the numerical results for the current evolution for the case when a constant frequency was used (red) and the case with velocity-dependent frequency (green). Since the current saturates much faster for the case with constant ν than for the case with velocity dependent ν , time has been multiplied by ten in the case of constant ν , for the sake of comparison. Also, the analytical saturated current values are shown in solid lines. The saturated current value for the case of a constant frequency is shown in magenta and the case with a velocity-dependent frequency in blue. We can see that the simulations (points) are in good agreement with the analytical currents (solid lines) and that the saturation current changes, as predicted by the theory, when a velocity-dependent collision frequency is used.

Finally, we test the effects of trapped particles on the current. For this purpose, we considered a tokamak configuration in the banana regime. To ensure that the

3. COLLISION IMPLEMENTATION TESTS

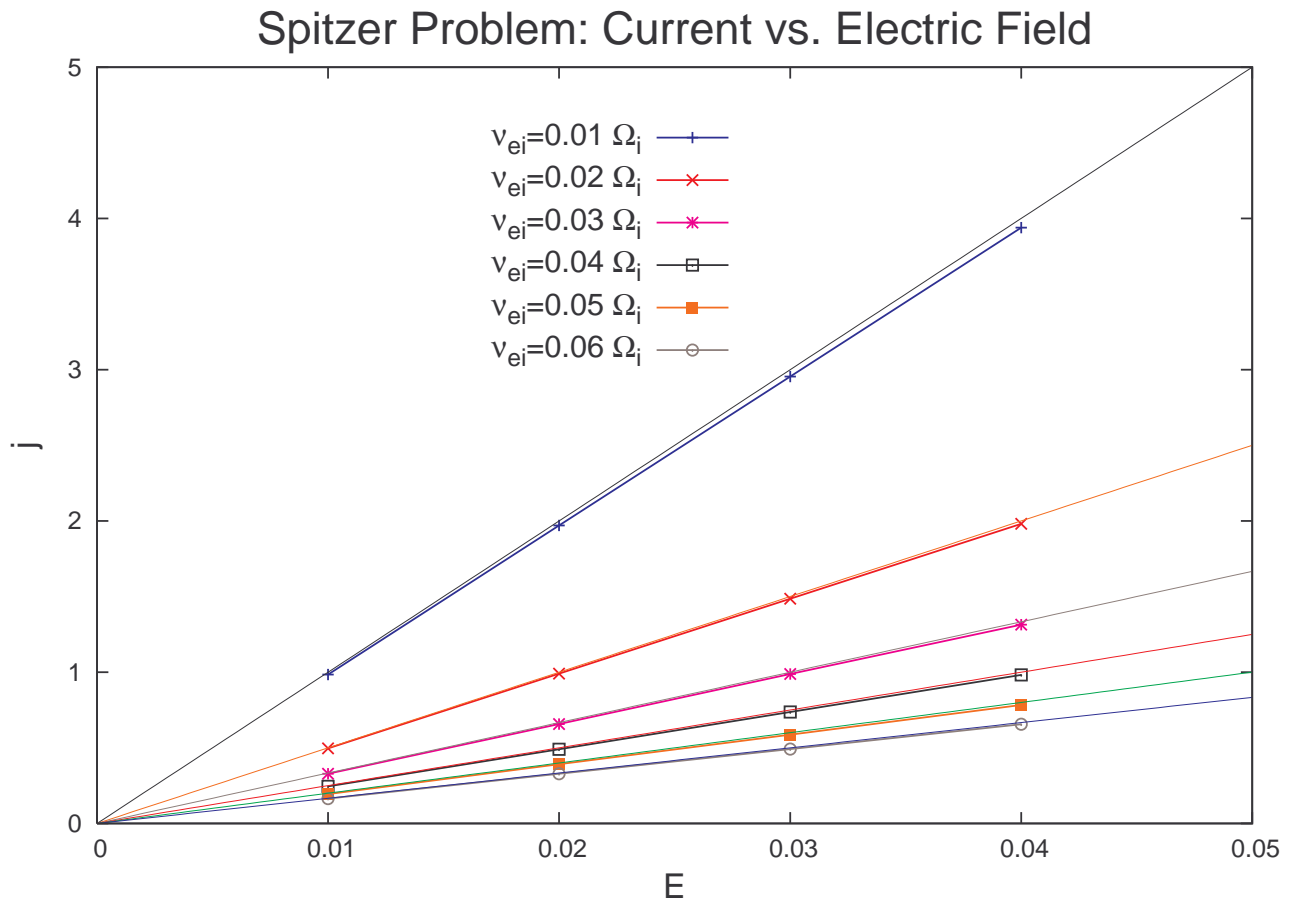


Figure 3.2: Collision frequency and electric field dependence of the Spitzer current in a cylinder. The collisionalities correspond to the Pfirsch-Schlüter regime. Solid lines show the analytical values and the symbols show the numerical results.

3.2 Spitzer problem

particles are deep in this regime, we chose a collisionality of $\nu = 1 \times 10^{-6} \Omega_*$. We set the value of the normalized external electric field to $\bar{E} = 10^{-2}$, used the time step $\Delta t = 50$ and the number of particles was $N = 5 \times 10^4$. In Fig. 3.4 we observe the flux-surface averaged parallel current evolution for the case without trapped particles (red) and the case with trapped particles (blue). In green, the analytical time-dependent current obtained from Eq. (3.41) is shown, where trapped particles are neglected. In magenta, we can observe the analytical saturation value for the current in the case with trapped particles, which is taken from Eq. (3.47).

We observe that when trapped particles are taken into account, the flux-surface averaged current decreases. This is due to the fact that, in a tokamak, for the low-collisionality banana regime, trapped particles dominate the transport and they do not carry any current.

From these results it is possible to conclude that the numerical implementation and results of the collisional effects are in good agreement with the theoretical predictions for the simple collision operator that was implemented.

It is important to remark that the collision operator $\nu\mathcal{L}$ uses a generic expression for the collision frequency. The currently implemented scheme solves the Lorentz operator numerically with the value of the collision frequency fixed from the input. The physical interpretation of the collision frequency varies depending on the case assumptions.

For example, in the case of neoclassical calculations in a tokamak, the process simulated was ion-ion collisions. Self collisions should not cause particle transport if momentum is conserved in an axisymmetric system. If momentum conservation is not implemented, however, a radial particle flux appears. We decided to simulate this radial particle flux because it is the simplest numerical case. The analytical fluxes were also calculated consistently with these assumptions (self collisions with no momentum conservation) in order to be able to compare the numerical and analytical results. If one would like to relate the ion particle flux resulting from these assumptions, to the electron particle flux caused by electron-ion collisions, which is the usual physical flux that is measured, one obtains (e.g. for the Pfirsch-Schlüter regime):

3. COLLISION IMPLEMENTATION TESTS

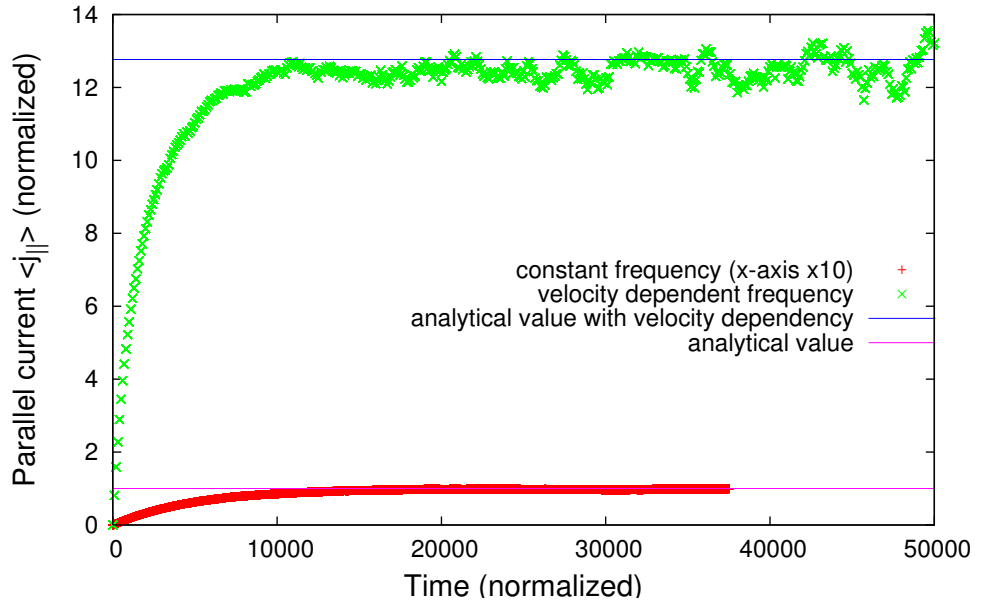


Figure 3.3: Saturation of the parallel current with $\nu = 10^{-2} \Omega_*$ and $\bar{E}_{\parallel} = 10^{-2}$ in a tokamak. In red is the current calculated with a constant collision frequency. In green, the current is calculated with a velocity dependent collision frequency. Since the current saturates much faster for the case with constant ν than for the case with velocity dependent ν , time has been multiplied by ten in the case of constant ν for the sake of comparison. The solid lines are the analytical saturation values for currents with a velocity independent (magenta) and velocity dependent (blue) collision frequencies.

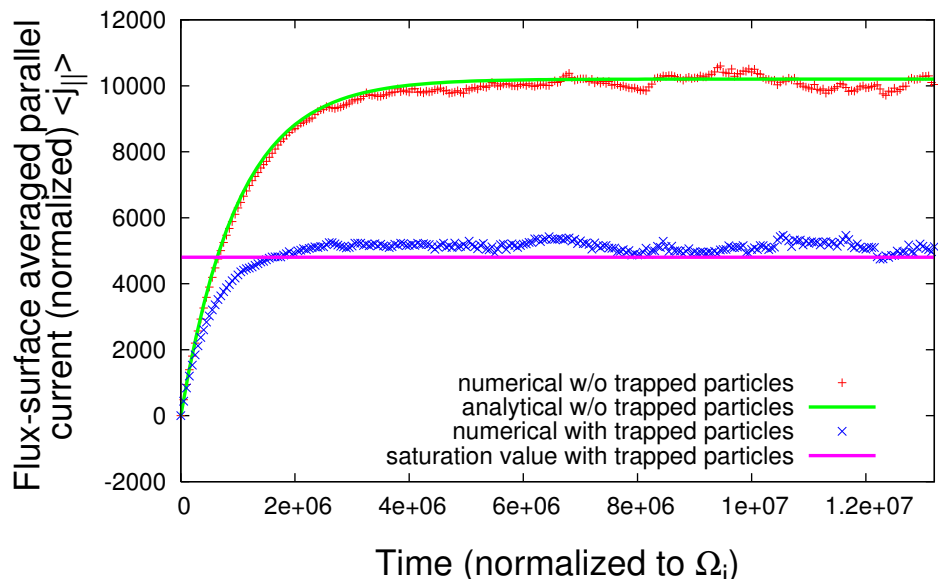


Figure 3.4: Current saturation in a tokamak: analytical (green, magenta) and numerical (red, blue) results ($\bar{E}_{\parallel} = 10^{-2}$ and $\nu = 10^{-6} \Omega_*$).

$$\frac{\Gamma_i}{\Gamma_e} \sim \sqrt{\frac{m_i}{m_e}}. \quad (3.49)$$

In the case of neoclassical calculations in a stellarator, we simulated ion-ion collisions without momentum conservation. Since stellarators are not axisymmetric, fluxes due to self collisions will always be present, with or without momentum conservation. We also compared the numerical results with the analytical calculations taking these assumptions into account.

In the case of microinstabilities calculations, we assumed the following: for ITGs (whether in tokamak or stellarator configurations) we simulated ion-ion collisions. For TEMs, electron-ion collisions were used.

Chapter 4

Neoclassical transport in EUTERPE

With the successful implementation of collisions in EUTERPE, it is now possible to perform neoclassical calculations. In the cases studied, we were only interested in the radial particle fluxes for the different collisional regimes. We calculate them, following the procedures in [55]. Since the main quantity investigated was the radial particle flux, we first derive analytical expressions for the flux in the different collisionality regimes. Then, the results obtained with EUTERPE are presented and compared with the analytical expressions.

4.1 Analytical fluxes in neoclassical regimes

4.1.1 Banana regime

In this regime, the collisionality is not high enough to interrupt the trapped orbits and f_1 can be expanded

$$f_1 = f_1^{(0)} + f_1^{(1)} + \dots , \quad (4.1)$$

in the way already discussed in Sec. 3.2.1. We then obtain the zeroth order equation,

$$\nabla_{\parallel} f_1^{(0)} = I \kappa F_m \nabla_{\parallel} \left(\frac{v_{\parallel}}{\Omega} \right) . \quad (4.2)$$

4. NEOCLASSICAL TRANSPORT IN EUTERPE

By integrating, we find that

$$f_1^{(0)} = \frac{I\kappa F_m}{\Omega_c} \left(h v_{\parallel} + \hat{f}_1 \right), \quad (4.3)$$

where \hat{f}_1 is such that

$$\frac{\partial \hat{f}_1}{\partial \theta} = 0, \quad (4.4)$$

and we have used $\Omega = \Omega_c/h$, where $\Omega_c \equiv ZeB_0/m$. In first order, the expansion gives

$$v_{\parallel} \nabla_{\parallel} f_1^{(1)} = C(f_1^{(0)}). \quad (4.5)$$

Now we use the same procedure that we used for the Spitzer problem: if $f(\psi, \theta)$ is any periodic function in θ , then,

$$\langle \mathbf{B} \cdot \nabla f(\psi, \theta) \rangle = 0. \quad (4.6)$$

Using this flux-surface average property in Eq. (4.5) and also $\mathcal{L}(v_{\parallel}) = -v_{\parallel}$ we arrive at the following expression:

$$\hat{f}_1 = -H(\lambda_c - \lambda)V_{\parallel}. \quad (4.7)$$

Remembering that λ_c is the trapped-passing boundary defined in the previous chapter before Eq. (3.23) and V_{\parallel} was defined in Eq. (3.24), then the complete solution is:

$$f_1^{(0)} = \frac{I\kappa F_m}{\Omega_c} (h v_{\parallel} - H V_{\parallel}). \quad (4.8)$$

Since f_1 is now known in lowest order, it is possible to calculate the radial particle flux:

$$\Gamma = \left\langle \int f_1 \mathbf{v}_{\mathbf{d}} \cdot \nabla \psi d^3 v \right\rangle \quad (4.9)$$

$$= - \left\langle \frac{I}{\Omega} \int v_{\parallel}^2 \nabla_{\parallel} f_1 d^3 v \right\rangle. \quad (4.10)$$

4.1 Analytical fluxes in neoclassical regimes

We recall that $f_1 = f_1^{(0)} + f_1^{(1)} + \dots$, but the contribution of $f_1^{(0)}$ is zero, so we take the next order and use Eq. (4.5) to finally obtain an expression for the flux as a function of $f_1^{(0)}$:

$$\Gamma = - \left\langle \frac{Ih}{\Omega_c} \int v_{\parallel} C(f_1^{(0)}) d^3v \right\rangle . \quad (4.11)$$

Using that $C(v_{\parallel}) = -\nu v_{\parallel}$ together with Eq. (4.8) we obtain

$$\Gamma = \frac{I^2}{\Omega_c^2} \left(\left\langle h^2 \int v_{\parallel}^2 \nu \kappa F_m d^3v \right\rangle - \left\langle h \int v_{\parallel} \nu \kappa F_m H V_{\parallel} d^3v \right\rangle \right) . \quad (4.12)$$

We define the following average operation in velocity space using the notation in [47],

$$\{F(v)\} \equiv \int F(v) \frac{mv_{\parallel}^2}{nT} F_m d^3v = \frac{8}{3\sqrt{\pi}} \int_0^{\infty} F(x) e^{-x^2} x^4 dx , \quad (4.13)$$

where $x^2 = mv^2/(2T) = v^2/v_{\text{th}}^2$ and the effective fraction of trapped particles is given by Eqs. (3.30) and (3.45). Using these definitions, and the assumption that ν is independent of the velocity, the terms on the right-hand side of Eq. (4.12) are:

$$\left\langle h^2 \int v_{\parallel}^2 \kappa F_m d^3v \right\rangle = \langle h^2 \rangle \cdot \frac{nT}{m} \{ \kappa(v) \} , \quad (4.14)$$

$$\left\langle h \int v_{\parallel} \kappa F_m H V_{\parallel} d^3v \right\rangle = \frac{nT}{m} f_c \{ \kappa(v) \} . \quad (4.15)$$

From the definition of $\kappa(v)$ in Eq. (2.147) we have

$$\{ \kappa(v) \} = - \left[\frac{1}{n} \frac{\partial n}{\partial \psi} + \frac{1}{T} \frac{\partial T}{\partial \psi} \right] = \kappa_n + \kappa_T . \quad (4.16)$$

Then the radial particle flux is

$$\Gamma = \frac{I^2 \nu n v_{\text{th}}^2}{\Omega_c^2} \frac{1}{2} (\kappa_n + \kappa_T) (\langle h^2 \rangle - f_c) . \quad (4.17)$$

Since $h \approx 1 + \epsilon \cos \theta$ for high aspect ratio devices with circular cross section, then we get $\langle h^2 \rangle \simeq 1 + \mathcal{O}(\epsilon^2)$.

4. NEOCLASSICAL TRANSPORT IN EUTERPE

We now notice that the thermal Larmor radius is $\rho_{th} = v_{th}/\Omega_c$ and that $\kappa_n = -\frac{1}{n} \frac{\partial n}{\partial r} / |\nabla\psi| = \tilde{\kappa}_n / |\nabla\psi|$, $\kappa_T = -\frac{1}{T} \frac{\partial T}{\partial r} / |\nabla\psi| = \tilde{\kappa}_T / |\nabla\psi|$. If we also make use of the identity:

$$\frac{I^2}{|\nabla\psi|^2} \approx \frac{q^2}{\epsilon^2}, \quad (4.18)$$

and

$$\langle \mathbf{\Gamma} \cdot \nabla r \rangle \simeq \frac{\langle \mathbf{\Gamma} \cdot \nabla\psi \rangle}{|\nabla\psi|}, \quad (4.19)$$

then the radial particle flux in the banana regime is

$$\Gamma_{\text{banana}} = \langle \mathbf{\Gamma} \cdot \nabla r \rangle \simeq \frac{\nu f_t n}{2} \left(\frac{\rho_{th} q}{\epsilon} \right)^2 (\tilde{\kappa}_n + \tilde{\kappa}_T). \quad (4.20)$$

4.1.2 Pfirsch-Schlüter regime

In the Pfirsch-Schlüter regime [70] the high collisionality prevents the particles from completing their orbits.

We take Eq. (2.148) and perform another subsidiary expansion of f_1 now taking into account the high collisionality,

$$f_1 = f_1^{(-1)} + f_1^{(0)} + f_1^{(1)} + \dots, \quad (4.21)$$

this time using the following smallness parameter:

$$\frac{f_1^{(0)}}{f_1^{(-1)}} \sim \frac{\omega_b}{\nu}. \quad (4.22)$$

It is important to note that since the collision operator is of the order of the collisionality ($\sim \mathcal{O}(\nu)$), a $f_1^{(-1)}$ term is necessary in the expansion of f_1 . The lowest order equation, then becomes

$$C(f_1^{(-1)}) = 0, \quad (4.23)$$

which means $f_1^{(-1)} = f_1^{(-1)}(\mathcal{E}, r, \theta)$ does not depend on λ . The zeroth order equation is

4.1 Analytical fluxes in neoclassical regimes

$$v_{\parallel} \nabla_{\parallel} f_1^{(-1)} - C(f_1^{(0)}) = 0, \quad (4.24)$$

which is solved by using the properties of the Lorentz operator:

$$f_1^{(0)} = -\frac{v_{\parallel}}{\nu} \nabla_{\parallel} f_1^{(-1)}. \quad (4.25)$$

The first order equation is

$$v_{\parallel} \nabla_{\parallel} f_1^{(0)} - C(f_1^{(1)}) = I \kappa v_{\parallel} F_m \nabla_{\parallel} \left(\frac{v_{\parallel}}{\Omega} \right). \quad (4.26)$$

Dividing by v_{\parallel} , integrating over λ and using that $v_{\parallel} = v \sqrt{1 - \lambda/h}$ we realize that the second term on the left-hand side gives zero. We use the fact that $\nabla_{\parallel} f = 0$ implies that $f = \mathcal{K}(\psi)$, where $\mathcal{K}(\psi)$ is an arbitrary function that depends only on ψ . Then we obtain

$$\int_0^h f_1^{(0)} d\lambda - \frac{I \kappa F_m h}{\Omega_c} \int_0^h v_{\parallel} d\lambda = \mathcal{K}(\psi). \quad (4.27)$$

Using Eq. (4.25) and remembering that $f_1^{(-1)}$ does not depend on λ , we arrive at the following expression:

$$h \frac{v}{\nu} \nabla_{\parallel} f_1^{(-1)} + \frac{I v \kappa F_m h^2}{\Omega_c} = -\frac{3}{2} \mathcal{K}(\psi). \quad (4.28)$$

We multiply by $\nu/(h^2 v)$ and take the flux-surface average to find the constant of integration

$$\mathcal{K}(\psi) = -\frac{2}{3} \frac{I v \kappa F_m}{\Omega_c} \frac{1}{\langle h^{-2} \rangle}. \quad (4.29)$$

Then the first order equation (4.26) is

$$\nabla_{\parallel} f_1^{(-1)} = \frac{I \kappa F_m \nu}{\Omega_c} \left(\frac{1}{h \langle h^{-2} \rangle} - h \right). \quad (4.30)$$

As before, with the banana-regime calculation, we need this result in order to calculate the radial particle flux. In the subsidiary expansion of f_1 , the term $f_1^{(0)}$ does not contribute to the flux, and $f_1^{(1)}$ is of higher order. Therefore, the only relevant term is $f_1^{(-1)}$. By using Eqs. (4.10) and (4.16) we obtain

4. NEOCLASSICAL TRANSPORT IN EUTERPE

$$\langle \mathbf{\Gamma} \cdot \nabla \psi \rangle = - \left\langle \frac{I^2 \nu h}{\Omega_c^2} \left(\frac{1}{h \langle h^{-2} \rangle} - h \right) \int v_{\parallel}^2 \kappa F_m d^3 v \right\rangle \quad (4.31)$$

$$= \frac{I^2 \nu n v_{th}^2}{\Omega_c^2} (\kappa_n + \kappa_T) \left(\langle h^2 \rangle - \frac{1}{\langle h^{-2} \rangle} \right). \quad (4.32)$$

The approximation of $h \approx 1 + \epsilon \cos \theta$ gives

$$\langle h^2 \rangle - \frac{1}{\langle h^{-2} \rangle} \approx 2 \epsilon^2, \quad (4.33)$$

and finally we arrive at

$$\boxed{\Gamma_{PS} = \langle \mathbf{\Gamma} \cdot \nabla r \rangle \simeq \nu \rho_{th}^2 q^2 n (\tilde{\kappa}_n + \tilde{\kappa}_T)}. \quad (4.34)$$

4.1.3 Plateau regime

For frequencies $\omega_t \epsilon^{3/2} \ll \nu \ll \omega_t$, we have an intermediate transport regime, which is almost independent of collisions, thus named plateau regime, referring to its flat shape in a Γ vs. ν graph. Here, the circulating particles with collision frequency similar to the transit frequency experience resonance. The solution to the kinetic equation when assuming $\epsilon \ll 1$ will not depend on the collision frequency, so the radial particle flux in this regime is [47]:

$$\boxed{\Gamma_{\text{plateau}} = \langle \mathbf{\Gamma} \cdot \nabla r \rangle \simeq \frac{\sqrt{\pi}}{4} \frac{\rho_{th}^2 v_{th} q n}{R_0} (\tilde{\kappa}_n + \frac{3}{2} \tilde{\kappa}_T)}. \quad (4.35)$$

Experimentally and numerically, the plateau regime is not so distinguishable from the other regimes since the transition from banana regime to plateau (or from $1/\nu$ to plateau in the stellarator case) occurs gradually due to the population of resonant particles increasing or decreasing with collisionality.

4.1.4 Stellarator $1/\nu$ regime

For axisymmetric magnetic fields, the Lagrangian does not depend on the toroidal angle φ , thus the toroidal canonical momentum p_φ is conserved. In stellarators, due to the complex 3D nature of the field geometry, there is no axisymmetry. So,

the toroidal canonical momentum is no longer conserved, which causes the radial excursion of the drift orbits not to be necessarily bounded, as in the axisymmetric case. Particles trapped in the helical wells are no longer confined and can leave the plasma. Collisions can then impede the radial motion, so that with lower collision rates, the particle transport is enhanced. As a consequence, in stellarators it is possible to observe a regime called the $1/\nu$ regime for low collisionalities, in which the radial particle flux increases as the collisionality decreases, as opposed to the tokamak banana regime. The flux is derived semi-analytically in [71]. If we take Eq. (26) from the mentioned reference, the particle flux across the flux surfaces is

$$\Gamma_{1/\nu} = -\frac{\sqrt{8}}{9\pi^{3/2}} \frac{v_{\text{th}}^2 \rho_{\text{th}}^2}{\nu R_0^2} \epsilon_{\text{eff}}^{3/2} \int_0^\infty \frac{e^{-z} z^{5/2}}{A(z)} \frac{n}{f_0} \frac{\partial f_0}{\partial r} dz, \quad (4.36)$$

where $z = v^2/v_{\text{th}}^2$, ν is assumed independent of the velocity and $A(z)$ is the factor that precedes the velocity-independent collision frequency in the Lorentz scattering operator. For the pitch-angle scattering operator, it is $A = 1/2$. After performing the integral, the flux in the $1/\nu$ regime is:

$$\Gamma_{1/\nu} = \langle \mathbf{\Gamma} \cdot \nabla r \rangle \simeq \frac{5}{12\pi} \frac{\rho_{\text{th}}^2 v_{\text{th}}^2 n (2\epsilon_{\text{eff}})^{3/2}}{\nu R_0^2} (\tilde{\kappa}_n + 2\tilde{\kappa}_T), \quad (4.37)$$

where all the geometry is implicit in the effective ripple ϵ_{eff} . Here, we have not considered the radial electric field ($E_r = 0$). In the core of most stellarators the electrons are often in this regime. If we approximate the velocity dependence of the collision frequency as $\nu \propto v_{\text{th}}^{-3}$, then the flux scales unfavorably with temperature as $\Gamma_{1/\nu} \propto T^{7/2}$. Therefore a great amount of research has focused on the optimization of the geometry with the goal of minimizing the losses in this regime.

4.2 Results and discussion

Monte Carlo simulations of neoclassical transport can be carried out mono-energetically as well as with particles having an arbitrary energy (velocity) distribution. The drawback of the latter is that it takes more computing time than

4. NEOCLASSICAL TRANSPORT IN EUTERPE

standard mono-energetic neoclassical codes. This is due to the presence of just a few particles carrying most of the energy. To be able to resolve these highly energetic particle orbits, the time step must be reduced. Moreover, neoclassical calculations only aim for steady-state results, whereas EUTERPE is an initial value code that calculates the entire time evolution. To arrive at a steady state, we need, at least, to run a simulation for a few collision times. We also need a high number of particles to reduce the statistical noise. These factors turn the calculation into a very time consuming procedure, since the particle flux is calculated by letting the simulation run until the saturation is clearly visible, and then performing an average (in time) from the saturation time until the end of the run. For example, in the Pfirsch-Schlüter regime (for tokamaks), since the collisionality is high (for the case below, $\nu = 3.3 \times 10^{-3} \Omega_*$), it takes less time to arrive at a steady state, thus, the calculation is not so costly. From Fig. 4.1 (left) we can see that the saturation time is around $t \sim 3 \times 10^4 \Omega_*^{-1}$ s, so the average is taken from this point until the end of the simulation ($t = 1 \times 10^5 \Omega_*^{-1}$ s). The value of this average is the saturated particle flux.

In the banana regime, however, the collisionality is low. Therefore it takes at least one to two orders of magnitude more time, in comparison with the highly collisional regime, to reach saturation (see Fig. 4.1 (right)) with the same time step. We can see that the saturation point is around $t \sim 8 \times 10^5 \Omega_*^{-1}$ s, which is almost two orders of magnitude more than in the Pfirsch-Schlüter case. This becomes an even greater problem when the calculations are performed in stellarator geometry, since the lack of axisymmetry adds complexity to the geometry, which requires higher resolution and, consequently, the simulation time increases even more.

For all the neoclassical simulations, the employed collision frequency was constant and a single species plasma with no electric field was used. All the particles were loaded in one bin (approximately equivalent to $s = 0.5$) to improve statistics and taking advantage of the local nature of the parameters. For simplicity, only a radial density gradient was considered, i.e. no temperature gradient. Also, to be consistent with the ordering of the drift-kinetic equation as discussed in section 2.6.4, the radial spatial drifts were suppressed from the trajectory equation, but retained as driving terms in the evolution of the distribution function. This has the effect of preventing the particles from leaving the flux-surface. It is relevant

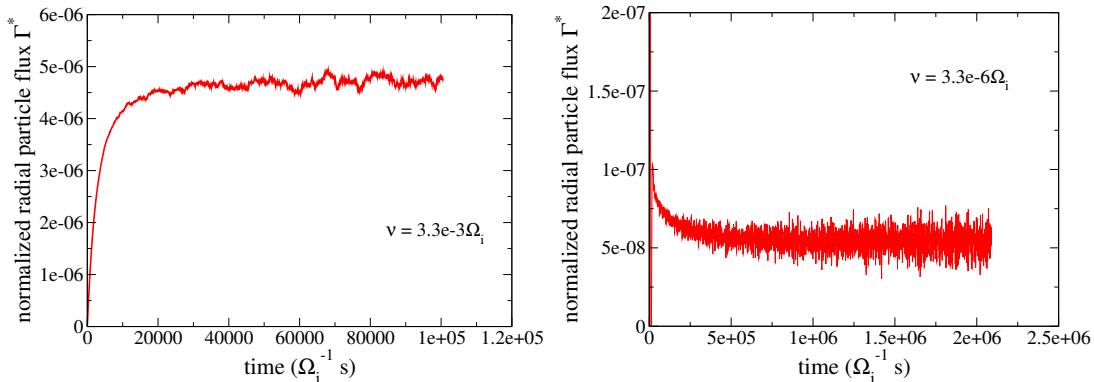


Figure 4.1: Time evolution of the normalized radial particle flux in the Pfirsch-Schlüter (left) and banana (right) regime in a tokamak.

to note that the particles in EUTERPE are not mono-energetic, therefore it is necessary to perform a convolution over the mono-energetic results in order to be able to make the comparison.

4.2.1 Implementation in EUTERPE

Adapting the gyrokinetic code to perform neoclassic calculations requires some care. In the neoclassical simulations done here, there is no external (nor self-consistent) electric field, hence all the electric field associated terms in the DKE are set to zero.

Next, since the particles are loaded in the r - z coordinates, mapping from one system of coordinates to the other is necessary. For these simulations we load all the markers in one bin, which is roughly equivalent to load them on a small volume between two neighboring flux-surfaces. The loading is done with a uniform distribution function f . We used 32 bins to represent the s direction and loaded the particles in the bin corresponding to $s_0 = 0.51$. This number was chosen to ensure that all the markers fall into one bin. If the number of bins is even, then at $s_0 = 0.5$ markers are loaded right between two bins, which is not desirable.

Let us recall that the drift velocity \mathbf{v}_d is not present in the trajectories, since in the neoclassical ordering it is of higher order. Even though this prevents the particles from leaving the selected flux-surface from the physical point of view, there are small numerical errors, e.g. in the field integration, that can force a small

4. NEOCLASSICAL TRANSPORT IN EUTERPE

number of particles to leave the defined flux-surface. It is, therefore, important to choose the time step correctly to be able to resolve trajectories with high velocities, thus avoiding this error. Fig. 4.2 shows how markers leave the flux-surface in the LHD stellarator. Initially, the markers are all in one bin. As time goes by, we can see that markers start to drift away from the middle flux-surface and start filling other bins, if the time step is not small enough.

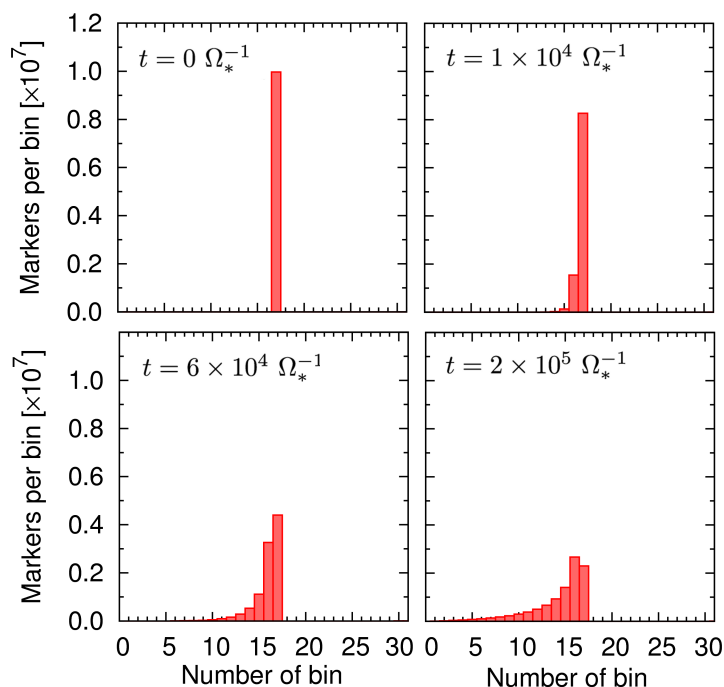


Figure 4.2: Time evolution of the marker distribution along the s direction, when the time step chosen is too large. Here, markers can be seen leaving the flux-surface in LHD.¹

For the diagnostics, the neoclassical flux was implemented in the following way: The Monte Carlo discretization of integrals over the distribution function is performed as

$$\int A f d^3 R d^3 v = \frac{1}{N_m} \sum_j A_j (V_j f_{0,j} + w_j) , \quad (4.38)$$

¹courtesy of J. García

where A is any quantity, N_m is the total number of markers and j is the label for each marker. Remembering the definition of the neoclassical radial transport in Eq. (2.149), we write

$$\langle \mathbf{\Gamma} \cdot \nabla \psi \rangle_{\text{neo}} = \left\langle \int \mathbf{v}_{\mathbf{D}} \cdot \nabla \psi \delta f d^3v \right\rangle = \frac{\int \int \mathbf{v}_{\mathbf{D}} \cdot \nabla \psi \delta f d^3v d^3r}{\int_{\Delta V} d^3r}. \quad (4.39)$$

Comparing with the Monte Carlo discretization, the discretized form for the radial particle flux is

$$\Gamma = \frac{\frac{1}{N_m} \sum_j (\mathbf{v}_{\mathbf{D}} \cdot \nabla \psi)_j w_j}{V_{\text{bin}}}, \quad (4.40)$$

where V_{bin} is the volume of the bin where the particles are loaded. The bin size (in s) must be small enough to avoid large variations of density and temperature through it. Another important point to consider is the addition of an external electric field to the neoclassical calculations. If an electric field were present, then it would not be possible to neglect the drift velocity without violating energy conservation. Calculations with electric fields, however, are outside of the scope of this work, and will not be discussed further.

It is also important to let the simulations run at least two or more collision times, which is especially time consuming when the collisionality is small, and the time step cannot be larger than a certain limit imposed by numerical stability.

4.2.2 Benchmark

We wish to compare the results of the Monte Carlo simulation and the neoclassical formalism. For that purpose, we compare the numerical results of the radial particle flux against the analytical values for a tokamak and a stellarator. In order to do so, we need the analytical quantities in their normalized form. The following parameters are required: the flux-surface where all the particles are loaded s_0 , the minor radius a , the major radius R_0 , the rotational transform value at the flux-surface $\iota(s_0)$, κ_n and κ_T respectively, and the Larmor radius r_* as defined in EUTERPE (see Eqs. (2.26-2.28)). In the case of a stellarator, the minor

4. NEOCLASSICAL TRANSPORT IN EUTERPE

radius a is calculated from the average cross section, and the major radius R_0 is calculated from the averaged volume and cross section. The effective ripple ϵ_{eff} is also needed for the stellarator calculations. This value is obtained with MCView [72] directly from the equilibrium, using the procedure in [71]. Normalizing the values in the different regimes described in the previous section, one obtains:

$$\Gamma_{\text{PS}} = \frac{4\bar{\nu}\bar{n}r_*\sqrt{s_0}}{a^2} (\kappa_n + \kappa_T) , \quad (4.41)$$

$$\Gamma_{\text{banana}} = \frac{2f_t\bar{\nu}\bar{n}r_*\sqrt{s_0}}{a^2\epsilon^2} (\kappa_n + \kappa_T) , \quad (4.42)$$

$$\Gamma_{1/\nu} = \frac{10}{3\pi} \frac{(2\epsilon_{\text{eff}})^{3/2}\bar{n}r_*^3\sqrt{s_0}}{a\bar{\nu}R_0^2} (\kappa_n + 2\kappa_T) , \quad (4.43)$$

$$\Gamma_{\text{plateau}} = \frac{\sqrt{2\pi}\bar{n}r_*^2\sqrt{s_0}}{aR_0} \left(\kappa_n + \frac{3}{2}\kappa_T \right) , \quad (4.44)$$

where $\kappa_n = -1/n \partial n / \partial s$ and $\kappa_T = -1/T \partial T / \partial s$.

We also compare the simulation results with the results from DKES (Drift Kinetic Equation Solver) code [73, 74]. DKES is a numerical tool which calculates the mono-energetic transport coefficients for a plasma based on the Fourier-Legendre expansion of the linearized drift kinetic equation. By mono-energetic, DKES assumes that the kinetic energy $\mathcal{K} = mv_{\parallel}^2/2 + m\mu B$ is conserved, therefore it becomes only a parameter in the kinetic equation. It also assumes that the density, temperature and electrostatic potential depend only on the local flux-surface ψ .

Once the mono-energetic coefficients are known from DKES, the flux-surface-averaged fluxes can be calculated by energy convolution and compared with the fluxes obtained by EUTERPE, as well as with the analytical values. Before the comparison, it is necessary to introduce the basics of the formalism used by DKES [75], to be able to calculate the particle flux from the mono-energetic coefficients. The thermodynamic forces A_i ,

$$A_1 = \frac{1}{n} \frac{dn}{dr} - \frac{qE_r}{T} - \frac{3}{2} \frac{1}{T} \frac{dT}{dr} , \quad (4.45)$$

$$A_2 = \frac{1}{T} \frac{dT}{dr} , \quad (4.46)$$

$$A_3 = - \frac{qB_0 \langle \mathbf{E} \cdot \mathbf{B} \rangle}{T \langle B^2 \rangle} , \quad (4.47)$$

drive the flux-surface-averaged fluxes I_i according to the linear relations

$$I_i = -n \sum_{j=1}^3 L_{ij} A_j, \quad (4.48)$$

where the term $\langle \mathbf{E} \cdot \mathbf{B} \rangle$ describes the effects of the parallel electric field, and

$$I_1 = \langle \mathbf{\Gamma} \cdot \nabla r \rangle, \quad (4.49)$$

$$I_2 = \left\langle \frac{\mathbf{Q}}{T} \cdot \nabla r \right\rangle, \quad (4.50)$$

$$I_3 = \frac{\langle \mathbf{J} \cdot \mathbf{B} \rangle}{qB_0}, \quad (4.51)$$

are the radial particle flux, the radial energy flux and the parallel current density respectively. The difference with Eqs. (2.149 - 2.151) is that the above mentioned equations are expressed in terms of the radius r instead of the flux surface ψ . The values for the fluxes, can be obtained by convolving the mono-energetic transport coefficients D_{ij} with the local Maxwellian distribution function:

$$L_{ij} = \frac{2}{\sqrt{\pi}} \int_0^{\infty} dK \sqrt{K} e^{-K} D_{ij}(K) h_i h_j, \quad (4.52)$$

where $h_1 = h_3 = 1$, $h_2 = K$, $K = mv^2/2T$. Since we are only interested in the radial particle flux I_1 and we assume no temperature gradient ($A_2 = 0$) and no electric field ($A_3 = 0$), the only coefficient of interest is D_{11} . The analytical form of these, is given by:

$$D_{11,PS} = \frac{2}{3} \frac{\rho^2 \nu}{\iota^2}, \quad (4.53)$$

$$D_{11,ban} = \frac{f_t}{3\epsilon^2 s} \frac{\rho^2 \nu}{\iota^2}, \quad (4.54)$$

$$D_{11,1/\nu} = \frac{(2\epsilon_{\text{eff}})^{3/2}}{9\pi} \frac{\rho^2 \nu^2}{\nu R_0^2}, \quad (4.55)$$

$$D_{11,PL} = \frac{\pi}{16} \frac{\rho^2 \nu}{\iota R_0}. \quad (4.56)$$

4. NEOCLASSICAL TRANSPORT IN EUTERPE

These coefficients, when convolved under the assumed conditions, give the analytical fluxes for each regime, which were quoted in the previous section.

DKES returns the coefficients normalized to the value in the plateau regime, $D_{11}^* = D_{11}/D_{11\text{PL}}$, therefore we normalize the analytical coefficients similarly:

$$D_{11,\text{PS}}^* = \frac{32}{3\pi}\nu_* , \quad (4.57)$$

$$D_{11,\text{ban}}^* = \frac{16}{3\pi} \frac{f_t}{\epsilon^2 S} \nu_* , \quad (4.58)$$

$$D_{11,1/\nu}^* = \left(\frac{4}{3\pi}\right)^2 \frac{(2\epsilon_{\text{eff}})^{3/2}}{\nu_*} , \quad (4.59)$$

$$D_{11,\text{PL}}^* = 1 , \quad (4.60)$$

where the frequency has been normalized to the transit frequency for a particle with pitch-angle $\lambda = 0$: $\nu_* = \nu/\omega_{\text{tr}}(v)$.

From DKES, we obtain the normalized mono-energetic coefficients D_{11}^* calculated numerically in terms of ν_* . It is possible to compare these values straightforward with the analytical values given above, however, the main interest here is to compare them with the results obtained by EUTERPE for the different regimes. The problem is that EUTERPE does not calculate mono-energetic coefficients, but it gives out the value of the particle flux in terms of $\nu_{\text{th}*} \equiv \nu R_0/(v_{\text{th}}\iota)$ instead. Therefore, we have to transform the data from EUTERPE to be able to compare then with the results from DKES. Formally, we should numerically convolve the data (D_{11}^*) but this is not necessary, since there is a simpler method of comparison. However, it is important to point out that this method only works when no temperature gradient is present.

As a first step, we write the analytical fluxes calculated from the convolution of the D_{11} coefficients, Eqs. (4.41-4.44), normalized to their plateau value $\Gamma^* = \Gamma/\Gamma_{\text{PL}}$:

$$\Gamma_{\text{PS}}^* = \frac{4}{\sqrt{\pi}} \nu_{\text{th}*} , \quad (4.61)$$

$$\Gamma_{\text{ban}}^* = \frac{2f_t}{\sqrt{\pi} \epsilon_{\text{eff}}^2} \nu_{\text{th}*} , \quad (4.62)$$

$$\Gamma_{1/\nu}^* = \frac{5}{3} \left(\frac{2\epsilon_{\text{eff}}}{\pi} \right)^{3/2} \frac{1}{\nu_{\text{th}*}} , \quad (4.63)$$

$$\Gamma_{\text{PL}}^* = 1 . \quad (4.64)$$

We see here that the density gradients cancel out with the normalization. We want to compare the results of $D_{11}(\nu_*)$ and $\Gamma^*(\nu_{\text{th}*})$, so we have to set $\nu_* \rightarrow 3\sqrt{\pi}\nu_{\text{th}*}/8$ in the normalized mono-energetic coefficients so that

$$\Gamma_{\text{PS}}^* = \frac{32}{3\pi} \left(\frac{3\sqrt{\pi}}{8} \nu_{\text{th}*} \right) , \quad (4.65)$$

$$\Gamma_{\text{ban}}^* = \frac{16}{3\pi} \frac{f_t}{\epsilon_{\text{eff}}^2} \left(\frac{3\sqrt{\pi}}{8} \nu_{\text{th}*} \right) . \quad (4.66)$$

Comparing these two equations with Eqs. (4.57) and (4.58) we see that by only changing this factor in the frequency it is now possible to directly compare the data. This works for both the Pfirsch-Schlüter and the banana regime since they depend linearly on the collision frequency ν . However, it does not work in the stellarator case where, for low collisionality, the flux is proportional to the inverse of the frequency ($1/\nu$ regime). We can now apply this method to the numerical data, multiplying the normalized frequency ν_* from DKES, by the factor $3\sqrt{\pi}/8$ and compare with the numerical results from EUTERPE in a tokamak. This is shown in Fig. 4.3 along with the analytical values calculated from Eqs. (4.65) and (4.66).

The plateau value for the particle flux is equal to unity. The parameters used in the simulation are: total number of particles $N = (1 - 10) \times 10^6$ and a time step $\Delta t = 100$ for low collisionality. For high collisionality, we used fewer particles and a shorter time step of $N = (1 - 3) \times 10^5$ and $\Delta t = 10$. For all the tokamak runs (both high and low collisionality) we used the flux-surface $s_0 = 0.51$, and the density and temperature profiles were defined by the values of $\kappa_n = 0.02$,

4. NEOCLASSICAL TRANSPORT IN EUTERPE

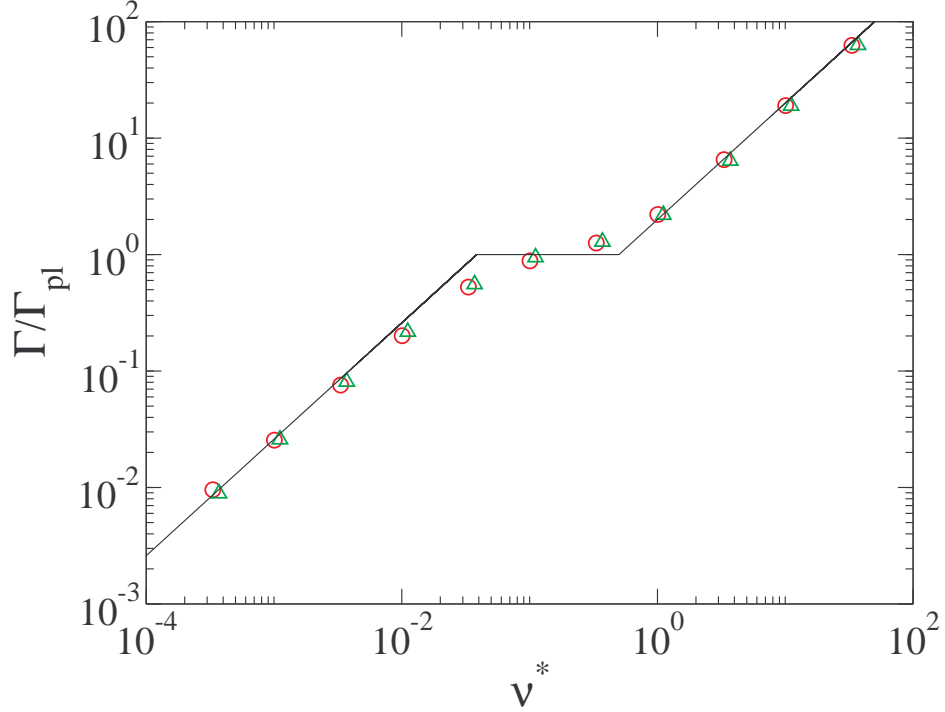


Figure 4.3: Neoclassical radial particle flux at $s = 0.51$ for a circular tokamak of aspect ratio $A = 5$ obtained with EUTERPE (red), DKES (green) and the analytical values (black). The flux is normalized to the analytical flux in the plateau regime and the collision frequency is normalized to the transit frequency.

$\kappa_T = 0.0$, respectively. The device used is a circular tokamak of aspect ratio $A = 5$ and major radius $R = 4$ m.

We observe a very good agreement between DKES and EUTERPE for a tokamak configuration in all the regimes. This prompts us to study the particle flux in a stellarator configuration.

4.2.2.1 Stellarator results

A benchmark was also performed for the case of a stellarator with no radial electric field ($E_r = 0$) as shown in Fig. 4.4. The equilibrium configuration is the magnetic geometry given by the *standard* LHD case with $R = 3.75$ m. The parameters used were: Total number of particles $N = 10^6$, time step $\Delta t = 5$, flux-surface $s_0 = 0.51$, and the density and temperature profiles are $\kappa_n = 0.582$, $\kappa_T = 0.0$, respectively. The run-times depend highly on the collisionality and they get more costly as the collision frequency decreases, or, on the other hand if it is too high. One run takes 24 CPU-hours on 512 processors for both extremes (low collisionality and high collisionality). For each point in the plot, the flux was calculated in time, until it saturated and from the approximate saturation time, a time average was performed to reduce the noise and obtain a single value. This value was taken as a data point. Stellarator cases are much more time-costly than the tokamak runs, since they require a smaller time step to be numerically stable. For the analytical results in the $1/\nu$ regime, the effective ripple value used for this flux-surface was $\epsilon_{\text{eff}} = 0.11152$. It can be seen that EUTERPE is in good agreement with the analytical theory [76].

4. NEOCLASSICAL TRANSPORT IN EUTERPE

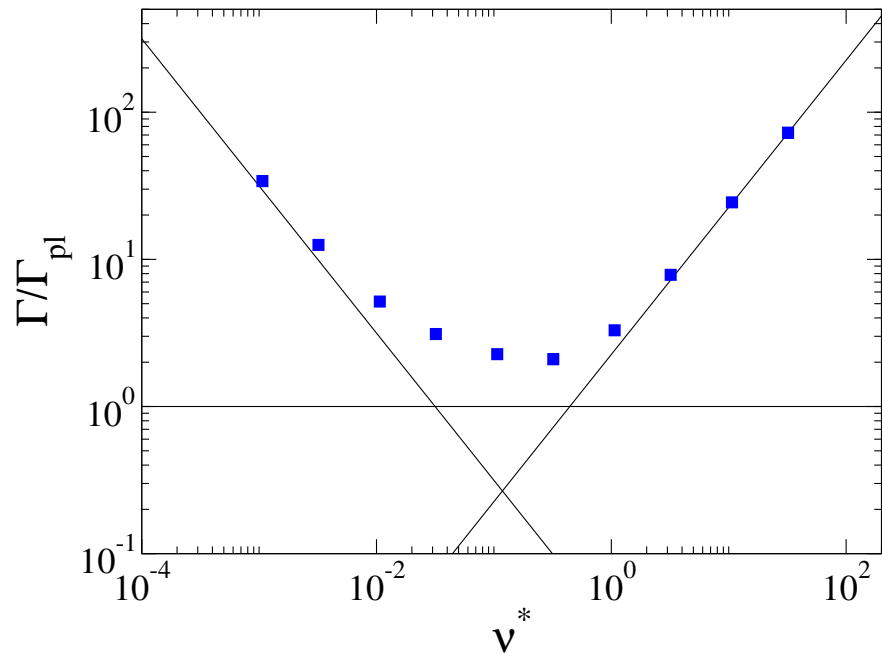


Figure 4.4: Neoclassical radial particle flux at $s = 0.51$ for the LHD stellarator with the *standard* magnetic configuration for $R = 3.75$ m with no radial electric field $E_r = 0$. Results shown for EUTERPE (blue) and the analytical values (black).

Chapter 5

Microinstabilities

In the next sections we will discuss ion-temperature-gradient instabilities (ITG) and trapped-electron-mode (TEM) instabilities, the latter known for being strongly influenced by collisions. In the results we will show the effects of collisions on these instabilities in cylinder, tokamak and stellarator geometry.

5.1 Gyrokinetic model for slab ITGs

Following the calculations done in V. Kornilov's thesis [21], we take the gyrokinetic equation and apply it for cylinder geometry. The distribution function is separated into an equilibrium and a perturbed part, $f = f_0 + f_1$, so that

$$\frac{\partial f_1}{\partial t} + \dot{\mathbf{R}} \cdot \frac{\partial f_1}{\partial \mathbf{R}} + v_{\parallel} \frac{\partial f_1}{\partial v_{\parallel}} = -\frac{\langle \mathbf{E} \rangle \times \mathbf{B}}{B^2} \cdot \frac{\partial f_0}{\partial \mathbf{R}} - \frac{q}{m} \langle \mathbf{E} \rangle \cdot \mathbf{b} \frac{\partial f_0}{\partial v_{\parallel}}, \quad (5.1)$$

where we have used the definition for the gyroaveraged field in (2.19). For the cylinder geometry, we choose Cartesian coordinates as shown in Fig. 5.1 left. The axes have been named r , θ and φ . Note that in this case, φ is a variable that measures a distance and has the dimension of length. This is done in order to look at a straight part of a plasma that is embedded in a toroidal geometry (Fig. 5.1, right). We also define the magnetic field as having only one component in the φ direction: $\mathbf{B} = B \hat{\varphi}$.

As before, we assume that the equilibrium distribution f_0 is a local Maxwellian as in (2.31), so that

5. MICROINSTABILITIES

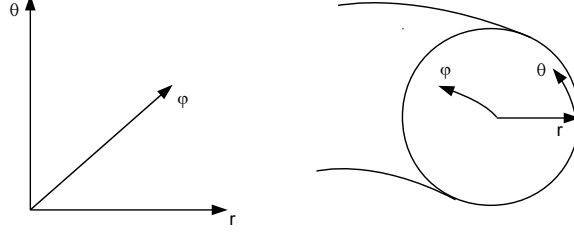


Figure 5.1: Coordinate system for slab ITGs.

$$f_0 = \frac{n_0(r)}{\pi^{3/2} v_{\text{th}}^3(r)} e^{-(v_{\parallel}^2 + v_{\perp}^2)/v_{\text{th}}^2}, \quad (5.2)$$

where now the density and temperature depend only on r . On the left-hand side, only the zeroth order terms of $\dot{\mathbf{R}}$ and $\dot{\mathbf{v}}_{\parallel}$ are present:

$$\dot{\mathbf{R}} = v_{\parallel} \hat{\mathbf{b}}, \quad \dot{\mathbf{v}}_{\parallel} = 0. \quad (5.3)$$

Hence, the gyrokinetic equation becomes

$$\frac{\partial f_1}{\partial t} + v_{\parallel} \frac{\partial f_1}{\partial \varphi} = -\frac{1}{B} \frac{\partial \langle \phi \rangle}{\partial \theta} \frac{\partial f_0}{\partial r} + \frac{q}{m} \frac{\partial \langle \phi \rangle}{\partial \varphi} \frac{\partial f_0}{\partial v_{\parallel}}. \quad (5.4)$$

The derivatives of the equilibrium distribution function can be calculated:

$$\frac{\partial f_0}{\partial r} = \frac{n'}{n} \left(1 - \frac{3}{2} \eta_i + \frac{v_{\parallel}^2 + v_{\perp}^2}{v_{\text{th}}^2} \eta_i \right) f_0, \quad (5.5)$$

$$\frac{\partial f_0}{\partial v_{\parallel}} = -2 \frac{v_{\parallel}}{v_{\text{th}}^2} f_0, \quad (5.6)$$

where $\eta_i \equiv d(\ln T)/d(\ln n)$ is the ratio between the scale lengths of density and ion temperature gradients. The prime here denotes the derivative with respect to r . Using a plane wave decomposition for the electric potential:

$$\phi(\mathbf{x}, t) = \tilde{\phi}(\mathbf{k}, \omega) e^{i\mathbf{k} \cdot \mathbf{x}}, \quad (5.7)$$

and the definition of the gyroaverage in Eq. (2.19), the gyroaveraged potential, in this case, can be written as

5.1 Gyrokinetic model for slab ITGs

$$\langle \phi \rangle (\mathbf{R}, t) = \int d\mathbf{k} J_0(k_\perp \rho_i) \tilde{\phi}(\mathbf{k}, \omega) e^{i(-\omega t + k_\parallel \varphi + k_r r + k_\theta \theta)}, \quad (5.8)$$

where J_n is the Bessel function of the first kind. We have also used the following identity:

$$J_0(z) = \frac{1}{\pi} \int_0^\pi e^{iz \cos \alpha} d\alpha. \quad (5.9)$$

We note that it is this Bessel function that accounts for the FLR effects in the evolution equation for the perturbed part of the distribution function, f_1 .

We apply a Fourier transform to Eq. (5.4) and replace the values given in Eqs. (5.5) and (5.6). For convenience, we drop the tilde on the Fourier-transform quantities and the equation becomes:

$$f_1 = \frac{1}{\omega - v_\parallel k_\parallel} \left[\frac{k_\theta n'}{B n} \left(1 - \frac{3}{2} \eta_i + \frac{v_\parallel^2 + v_\perp^2}{v_{\text{th}}^2} \eta_i \right) + 2 \frac{q}{m} k_\parallel \frac{v_\parallel}{v_{\text{th}}^2} \right] J_0(k_\perp \rho_i) \phi f_0. \quad (5.10)$$

On the other hand, by using the definition in Eq. (2.20), we obtain the ion density:

$$n_i = \bar{n}_i + \frac{n_0 e \phi}{T_{e0}} \left[\Lambda_0 \left(\frac{k_\perp^2 T}{m \Omega_c^2} \right) - 1 \right], \quad (5.11)$$

where

$$\bar{n} = \int f_1 \delta(\mathbf{R} - \mathbf{x} + \boldsymbol{\rho}) B d\alpha d v_\parallel d\mu. \quad (5.12)$$

We have used the definition $\Lambda_n(x) \equiv I_n(x) e^{-x}$ and the following identity [77]:

$$\int_0^\infty J_n(px) J_n(qx) e^{-x^2} x dx = \frac{1}{2} I_n \left(\frac{pq}{2} \right) e^{-(p^2 + q^2)/4}, \quad (5.13)$$

where I_n is the modified Bessel function of the first kind. By using the adiabaticity of electrons it is possible to find, after some algebra, the gyrokinetic dispersion relation:

5. MICROINSTABILITIES

$$\begin{aligned}
2 + \Lambda_0(\zeta) \left\{ -1 + \chi_n \eta_i \left(\chi + \chi^2 Z(\chi) - \frac{Z(\chi)}{2} \right) + \chi_n Z(\chi) + \right. \\
\left. + \frac{1}{\tau} [1 + \chi Z(\chi)] \right\} + \chi_n \eta_i \zeta Z(\chi) [\Lambda_1(\zeta) - \Lambda_0(\zeta)] = 0,
\end{aligned} \tag{5.14}$$

where

$$\begin{aligned}
\chi &= \frac{\omega}{k_{\parallel} v_{\text{th}}}, & \chi_n &= \frac{\omega_n}{k_{\parallel} v_{\text{th}}}, & \omega_n &= \frac{T_{e0}}{eB} k_{\theta} \frac{n'}{n}, \\
\tau &= T_{i0}/T_{e0}, & \zeta &= \left(\frac{k_{\perp} v_{\text{th}}}{\sqrt{2}\Omega_c} \right)^2 = (k_{\perp} \rho_i)^2,
\end{aligned}$$

and $Z(\chi)$ is the plasma dispersion function. Since we are interested in the growth rate of the instability, we use the dispersion function definition for $\text{Im}(\chi) > 0$:

$$Z(\chi) = \frac{1}{\sqrt{\pi}} \int_{-\infty}^{+\infty} \frac{e^{-t^2}}{t - \chi} dt. \tag{5.15}$$

If $k_{\perp} \rho_{\text{th}} \ll 1$ (i.e. $\zeta \ll 1$) then we can approximate:

$$\Lambda_0(\zeta) \approx 1 - \zeta + \frac{3}{4}\zeta^2 + O(\zeta^3), \tag{5.16}$$

$$\Lambda_1(\zeta) \approx \frac{\zeta}{2} - \frac{\zeta^2}{2} + O(\zeta^3). \tag{5.17}$$

If we evaluate Eq. (5.14) to zeroth order in ζ we obtain

$$1 + \chi_n \eta_i \left(\chi + \chi^2 Z(\chi) - \frac{Z(\chi)}{2} \right) + \chi_n Z(\chi) + \frac{1}{\tau} [1 + \chi Z(\chi)] = 0, \tag{5.18}$$

which is exactly the drift-kinetic dispersion relation. The recovery of the drift-kinetic equation from the gyrokinetic equation by assuming $k_{\perp} \rho_{\text{th}} \ll 1$ is expected, since when taking this limit, we are neglecting the FLR effects. If we further take the fluid limit, $\chi \gg 1$, we can expand Z to second order in χ . Here, we neglect the Landau damping term. By also considering a flat density profile, we obtain

$$1 - \frac{k_{\parallel}^2 v_{\text{th}}^2}{\omega^2} \left(1 - \frac{\omega_T}{\omega}\right) = 0, \quad (5.19)$$

where $\omega_T \equiv k_{\theta} T' / (eB)$. To solve this equation, it is necessary to separate the frequency into a real and an imaginary part $\omega = \omega_r + i\gamma$, where γ is the growth rate of the instability. Making the assumption that $k_{\parallel} v_{\text{th}} \ll \omega_T$ one can obtain an estimate for γ :

$$\gamma = \frac{\sqrt{3}}{2} |(k_{\parallel} v_{\text{th}})^2 \omega_T|^{1/3}. \quad (5.20)$$

This shows that the instability depends on the ion temperature gradient. However, this example is not accurate since the observed maximal instability growth rates occur for $k_{\perp} \sim \rho_i$, therefore it becomes essential to solve Eq. (5.14). It is possible to show that an instability can arise only when either [78]

$$\eta_i > 2 \left(1 - 2\zeta \frac{\Lambda_1(\zeta) - \Lambda_0(\zeta)}{\Lambda_0(\zeta)}\right)^{-1}, \quad (5.21)$$

or

$$\eta_i < 0, \quad (5.22)$$

for any value of ζ . An additional condition for the instability to arise is that $k_{\parallel} < k_{\parallel \text{lim}}$, which in the limit for $\zeta \ll 1$ becomes

$$k_{\parallel \text{lim}} = \frac{1}{2} \left(1 - \frac{2}{\eta_i}\right)^{1/2} \frac{|\omega_T|}{v_{\text{th}}}. \quad (5.23)$$

If we neglect the FLR effects in (5.21), this equation reduces to $\eta_i > 2$.

5.2 Toroidal ITGs

In the case of a toroidal system, drifts are introduced due to the curved geometry of the magnetic field, as well as trapped particle effects. In the following calculations, the trapped particle effects will be neglected, $\dot{v}_{\parallel} = 0$. Following the procedure of [79] we take the ion DKE, but now with the ∇B and curvature drifts $\dot{\mathbf{R}} = v_{\parallel} \hat{\mathbf{b}} + \mathbf{v}_d$,

5. MICROINSTABILITIES

$$\begin{aligned} \frac{\partial f_1}{\partial t} + \dot{\mathbf{R}} \cdot \frac{\partial f_1}{\partial \mathbf{R}} + \dot{v}_{\parallel} \frac{\partial f_1}{\partial v_{\parallel}} = & -\frac{\mathbf{E} \times \mathbf{B}}{B^2} \cdot \frac{\partial f_0}{\partial \mathbf{R}} - \frac{q}{m} \mathbf{E} \cdot \mathbf{b} \frac{\partial f_0}{\partial v_{\parallel}} \\ & - \left(v_{\parallel} \frac{\partial f_0}{\partial v_{\parallel}} + \frac{v_{\perp}}{2} \frac{\partial f_0}{\partial v_{\perp}} \right) \left(\frac{\hat{\mathbf{b}} \times \nabla B}{B^2} \right) \cdot \mathbf{E} , \end{aligned} \quad (5.24)$$

with the drift velocity (at low β):

$$\mathbf{v}_d = \frac{1}{B\Omega_i} \left(\frac{v_{\perp}^2}{2} + v_{\parallel}^2 \right) \left(\hat{\mathbf{b}} \times \nabla B \right) . \quad (5.25)$$

We can then again apply a Fourier transform and obtain the following relation:

$$f_1 = \left\{ -1 + \frac{1}{(\omega - v_{\parallel} k_{\parallel} - \mathbf{k} \cdot \mathbf{v}_d)} \left[\omega - \frac{T k_{\theta} n'}{q B n} \left(1 - \frac{3}{2} \eta_i + \frac{v_{\parallel}^2 + v_{\perp}^2}{v_{\text{th}}^2} \eta_i \right) \right] \right\} \frac{q}{T} \phi f_0 , \quad (5.26)$$

where \mathbf{v}_d is assumed to be independent of the poloidal angle. Using quasineutrality with adiabatic electrons, we get

$$\frac{1}{\tau} + 1 - \int \frac{f_0}{n_0 (\omega - k_{\parallel} v_{\parallel} - \mathbf{k} \cdot \mathbf{v}_d)} \left[\omega - \frac{T k_{\theta} n'}{q B n} \left(1 - \frac{3}{2} \eta_i + \frac{v_{\parallel}^2 + v_{\perp}^2}{v_{\text{th}}^2} \eta_i \right) \right] d^3 v = 0 . \quad (5.27)$$

In order to obtain the dispersion relation in the fluid limit, the following assumptions are made: $|k_{\parallel} v_{\text{th}}/\omega| \ll 1$ and $|\mathbf{k} \cdot \mathbf{v}_d/\omega| \ll 1$. Then, for $T_{e0} = T_{i0}$ the following is obtained [80, 81]:

$$1 + \frac{\omega_n}{\omega} - \left[\frac{k_{\parallel}^2 v_{\text{th}}^2}{\omega^2} + \frac{\omega_d}{\omega} \right] \left[1 - \frac{\omega_n}{\omega} (1 + \eta_i) \right] = 0 , \quad (5.28)$$

where

$$\omega_d = -\frac{2T k_{\theta}}{q B L_B} = 2\epsilon_n \omega_n , \quad (5.29)$$

is the drift frequency. Also we have defined $L_B \equiv |\partial \ln B / \partial r|^{-1}$ and $\epsilon_n = L_n / L_B$. If one additionally neglects density gradients, we arrive at

$$1 - \left[\frac{k_{\parallel}^2 v_{\text{th}}^2}{\omega^2} + \frac{\omega_d}{\omega} \right] \left(1 - \frac{\omega_T}{\omega} \right) = 0, \quad (5.30)$$

which results in an instability even when $k_{\parallel} = 0$, due to the term ω_d which contains the influence of the magnetic field curvature. In the limit $k_{\parallel} = 0$ and $\omega_d \ll \omega_T$ the solution is

$$\omega = \pm (-\omega_d \omega_T)^{1/2}. \quad (5.31)$$

From this relation we can see that, for $k_{\parallel} = 0$, an instability appears if L_B is positive. This means that, due to the ∇B drift, the instabilities appear on the low-field side of the torus (the unfavorable curvature region). On the contrary, the mode is stable if ω_d is larger than zero (favorable curvature region).

If we now solve Eq. (5.28) for $k_{\parallel} = 0$ we obtain the following solution:

$$\omega = \frac{1}{2} \left[(\omega_d - \omega_n) \pm \sqrt{(\omega_d - \omega_n)^2 - 4\omega_d \omega_n (1 + \eta_i)} \right]. \quad (5.32)$$

Thus, the threshold for the toroidal ITG instability in this (quite crude) approximation is

$$\eta_i > \frac{(2\epsilon_n - 1)^2}{8\epsilon_n} - 1. \quad (5.33)$$

This equation shows that, in a similar manner to the slab ITG instabilities, the toroidal ITGs have a threshold for the onset of the instability, but in the latter case, it depends on the ratio between the characteristic length of the density and the scale length of the magnetic variation. If $\epsilon_n < 1/2$, the ITG mode propagates in the electron diamagnetic direction.

It is important to note that this result has been derived in a very naive fluid approximation and therefore represents just a very rough estimate of the instability threshold. The kinetic approach, on the other hand, is quite different since for the same values of ϵ_n the η_i critical value is much higher (see example in Fig. 2.8 in [79]). The main reason why the fluid treatment given here yields such a pessimistic result, is the expansion in $|\mathbf{k} \cdot \mathbf{v}_d/\omega| \ll 1$, which neglects the possibility of a drift resonance in Eq. (5.27).

5. MICROINSTABILITIES

5.3 Trapped electron mode instabilities

This mode is present when the frequency ω of a perturbation is between the ion bounce frequency and the electron bounce frequency, so the majority of the electrons are trapped and perform complete banana orbits. As opposed to the ITG instability, the TEM instability persists even for low values of η_i , where a *pure* ITG instability would be absent. TEMs are coupled with the ITG modes, so there is no *pure* TEM mode (unless $\eta_i = 0$), and we can only speak about dominant effects. The coupling occurs especially in the region of the onset of the adiabatic ITG instability. However, if we find instabilities at low values of η_i with kinetic electrons (where the adiabatic electrons case would give $\gamma = 0$) we can assume that these instabilities are mainly driven by trapped electrons.

We now want to solve the bounce-averaged DKE for electrons following the procedure of [79, 82]. We start from Eq. (5.24) and similarly to the ITG case, apply the Fourier transform to obtain

$$\frac{dg_1}{dt} = \frac{\partial g_1}{\partial t} + \dot{\mathbf{R}} \cdot \frac{\partial g_1}{\partial \mathbf{R}} + \dot{v}_{\parallel} \frac{\partial g_1}{\partial v_{\parallel}} = \left[\omega - \frac{T k_{\theta} n'}{q B n} \left(1 - \frac{3}{2} \eta_i + \frac{v_{\parallel}^2 + v_{\perp}^2}{v_{\text{th}}^2} \eta_i \right) \right] \frac{q}{T} \phi f_0, \quad (5.34)$$

where d/dt is the total time derivative along the unperturbed trajectories and $g_1 \equiv f_1 + q\phi f_0/T$. This equation will now be expanded in the order of the small parameter $\epsilon_b = \omega/\omega_b \ll 1$. We assume $\omega \sim \omega^*$, where

$$\omega^* = \frac{T k_{\theta} n'}{q B n} \left(1 - \frac{3}{2} \eta_i + \frac{v_{\parallel}^2 + v_{\perp}^2}{v_{\text{th}}^2} \eta_i \right), \quad (5.35)$$

and subtract the slow toroidal precessional drift $\langle \dot{\varphi} \rangle$ from the fast periodic trapping motion. To the lowest order in ϵ_b , we get

$$\left(\dot{\mathbf{R}} \cdot \frac{\partial}{\partial \mathbf{R}} - \langle \dot{\varphi} \rangle \frac{\partial}{\partial \varphi} \right) g_1^{(0)} = 0, \quad (5.36)$$

with

$$\langle \dot{\varphi} \rangle = \frac{1}{\tau_b} \int_0^{\tau_b} \frac{d\varphi}{dt} dt, \quad (5.37)$$

5.3 Trapped electron mode instabilities

where τ_b is the bounce time as defined in Eq. (2.134). This means that $g_1^{(0)}$ is constant along the (non-drifting) banana orbits. In first order in ϵ_b we get

$$\left(\dot{\mathbf{R}} \cdot \frac{\partial}{\partial \mathbf{R}} - \langle \dot{\varphi} \rangle \frac{\partial}{\partial \varphi} \right) g_1^{(1)} + i(\omega - N \langle \dot{\varphi} \rangle) g_1^{(0)} = \frac{q}{T} \phi f_0 (\omega - \omega^*) , \quad (5.38)$$

where we have assumed perturbations with the form $\exp -i(\omega - N \langle \dot{\varphi} \rangle)$, where N is the toroidal wave number. If we average this expression over a banana trajectory, we obtain the bounce-averaged equation:

$$(\omega - N \langle \dot{\varphi} \rangle) g_1^{(0)} = (\omega - \omega^*) \frac{q f_0}{T} \langle \phi \rangle_b , \quad (5.39)$$

with

$$\langle \phi \rangle_b = \frac{1}{\tau_b} \int_0^{\tau_b} \phi dt . \quad (5.40)$$

For g_1 , one obtains

$$g_1 = \frac{(\omega - \omega^*)}{(\omega - N \langle \dot{\varphi} \rangle)} \frac{q f_0}{T} \langle \phi \rangle_b \quad (5.41)$$

Next, we approximate $\langle \phi \rangle_b \simeq \phi$ and calculate the non-adiabatic density fluctuation of the trapped electrons \bar{n}_b by integrating g_1 over the velocity space and multiplying by the fraction of trapped particles α_b , resulting in:

$$\bar{n}_b = \alpha_b \int d^3v g_1 , \quad (5.42)$$

where the fraction of trapped particles is estimated as

$$\alpha_b \simeq \sqrt{1 - \frac{B}{B_{\max}}} . \quad (5.43)$$

It can be shown [79] that the density fluctuation is

$$\bar{n}_b = -2\alpha_b n_0 \frac{q\phi}{T} \frac{1}{\omega_\varphi} \left\{ \left[\omega - \omega_n \left(1 - \frac{3}{2}\eta \right) \right] (1 + z_b Z(z_b)) - \omega_n \eta \left[\frac{\omega}{\omega_\varphi} (1 + z_b Z(z_b)) + \frac{1}{2} \right] \right\} , \quad (5.44)$$

5. MICROINSTABILITIES

where ω_φ is

$$\omega_\varphi \approx \omega_n \epsilon_n, \quad (5.45)$$

and $z_b = \text{sign}(\omega_\varphi) \sqrt{\omega/\omega_\varphi}$, where it is assumed that the electrons that contribute the most to the instability are deeply trapped.

In the case of a large aspect ratio tokamak, it is possible to find an expression for the toroidal precession drift as

$$N \langle \dot{\varphi} \rangle = -\frac{1}{2\Omega_i} \frac{q}{\rho_i} \frac{v^2}{R}. \quad (5.46)$$

To obtain the pure TEM mode, we have to make further assumptions such as neglecting the parallel ($k_{\parallel} = 0$) and perpendicular ($\mathbf{k} \cdot \mathbf{v}_D = 0$) ion drive in Eq. (5.26). Hence, we obtain that the ion perturbed density is just $\bar{n}_i = n_0 e \omega_{ni} / (T_{i0} \omega) \phi$. Using this, we arrive at the dispersion relation for TEMs:

$$0 = \frac{1}{\tau} + \frac{1}{\tau} \frac{2\alpha_b}{\omega_{\varphi e}} \left\{ \left[\omega - \omega_{ne} \left(1 - \frac{3}{2} \eta_e \right) \right] (1 + z_{be} Z(z_{be})) - \omega_{ne} \eta_e \left[\frac{\omega}{\omega_{\varphi e}} (1 + z_{be} Z(z_{be})) + \frac{1}{2} \right] \right\} + \frac{\omega_{ni}}{\omega}. \quad (5.47)$$

In order to get a rough estimate for the growth rate, we assume $|\omega/\omega_{\varphi e}| \gg 1$, $\tau = 1$ and expand the plasma dispersion function to the lowest order terms to obtain

$$0 = 1 + \alpha_b \left[-1 + \frac{\omega_{ne} - 3\omega_{\varphi e}/2}{\omega} + \frac{3}{2} \frac{\omega_{\varphi e} \omega_{ne} (1 + \eta_e)}{\omega^2} \right] - \frac{\omega_{ne}}{\omega}. \quad (5.48)$$

For values of $\eta_e \gg 1$, this equation yields a growth rate for the trapped electron mode instability:

$$\gamma \simeq \sqrt{\frac{3}{2} \frac{\alpha_b}{1 - \alpha_b} \omega_{\varphi e} \omega_{ne} (1 + \eta_e)}. \quad (5.49)$$

We note that the growth rate of the TEM instability depends on the fraction of trapped electrons.

5.4 Results and discussion

With collisions now implemented in EUTERPE, we want to investigate their effects on instabilities. First, the overall effects of collisions on ITG instabilities for different geometries will be shown. Secondly, collisional effects for TEM instabilities will be presented for a tokamak configuration. Finally, collisional ITG instabilities results will be illustrated in more detail for two stellarator cases: the LHD and the W7-X devices.

5.4.1 ITG instabilities with collisions

As a first test case, we vary the collision frequency to observe how it influences the growth rate of the ITG mode. We study this for different geometries: cylinder, tokamak and stellarator. The cylinder configuration is a particularly simple case in which only slab ITG modes can be found. Tokamak geometry, on the other hand, produces mainly curvature driven modes. The stellarator has a more complex geometry that produces a mixture of slab and toroidal ITG modes, which we want to investigate. For all these cases we have assumed a single species plasma and adiabatic electrons. The temperature profile is defined as:

$$\frac{1}{T} \frac{dT}{ds} = -\frac{\kappa_T}{1-C} \left[\cosh^{-2} \left(\frac{s-s_0}{\Delta s} \right) - C \right] \quad \text{with} \quad C = \cosh^{-2} \left(\frac{s_0}{\Delta s} \right), \quad (5.50)$$

where Δs is the width of the profile in s . The density profile $n^{-1}dn/ds$ is defined in the same way, but using the corresponding density parameters. It is important to note that, although the notation of κ_n and κ_T is the same as for the neoclassical calculations, here it has a different meaning: They now provide a tanh-like profile for all flux-surfaces, with κ_n and κ_T representing the maximum of the logarithmic gradient at s_0 of the density and the temperature, respectively.

The density profile was initially chosen to be flat, $\kappa_n = 0.0$, so that η_i is infinite throughout the plasma. Also, $\kappa_T = 3.5$ was chosen with a profile width $\Delta s_T = 0.2$.

We perform a scan for frequency values, starting from $\nu = 0$ to values near $\nu = 1 \times 10^{-2} \Omega_*$. Larger values of ν are unimportant in fusion experiments. For

5. MICROINSTABILITIES

reference, typical values of frequency are given in Table 2.1. If we take $\Omega_i \sim 10^8 \text{ s}^{-1}$ then the typical collision frequency values in terms of the ion cyclotron frequency are $\nu \sim 10^{-6} - 10^{-2} \Omega_i$.

For the circular tokamak configuration, an aspect ratio $A = 5$ was used with minor radius $a = 0.8 \text{ m}$. The Fourier filter was characterized by $M_0 = 70$, $N_0 = -38$, with Fourier filter widths of $\Delta m = 15$, $\Delta n = 0$. These define the size of the filter that contains the Fourier spectrum. There is no need for an n filter width since the tokamak is symmetric in the toroidal direction and different toroidal modes therefore evolve independently of one another. The grid size is $64 \times 32 \times 32$ in s, θ, φ and the particle number is $N = 1 \times 10^6$. The time step was chosen as $\Delta t = 20$. An equivalent geometry was used for the analytical cylinder configuration: this means that the radius of the cylinder is equal to the minor radius of the tokamak and the length of the cylinder is $2\pi R$, where R is the major radius of the tokamak. This is done to be able to compare with the tokamak configuration. Additionally, the cylinder configuration has no rotational transform.

For the stellarator, the LHD configuration was used, with $R = 3.75 \text{ m}$ and $\beta = 1.5\%$. In all LHD stellarator cases studied in this section, the following phase factor and filter values were used: $M_0 = -37$, $N_0 = -33$, $\Delta m = 50$, $\Delta n = 4$. The grid size was $64 \times 128 \times 128$ in s, θ, φ and the number of particles was $N = 16 \times 10^6$. The time step was chosen as $\Delta t = 5$. In general, higher particle numbers, finer grids and smaller time steps are needed for stellarator simulations in comparison with tokamak simulations, which make them much more costly. Also, a longer simulation time is needed to measure a growth rate. As an example, for these particular results, one tokamak (and cylinder) simulation with 64 processors took less than one CPU-hour, while the stellarator, in the high-collisional case, with 128 processors took 24 CPU-hours. It is also important to note that the stellarator results here cannot be quantitatively compared with the tokamak and cylindrical cases, since the rotational transform and other quantities such as phase factors and filter values were different. They are plotted together for the purpose of qualitative analysis only. It is crucial for the stellarator simulations to use an appropriate particle reinsertion method (stellarator symmetric) for particles leaving the computational domain. The method changes the poloidal

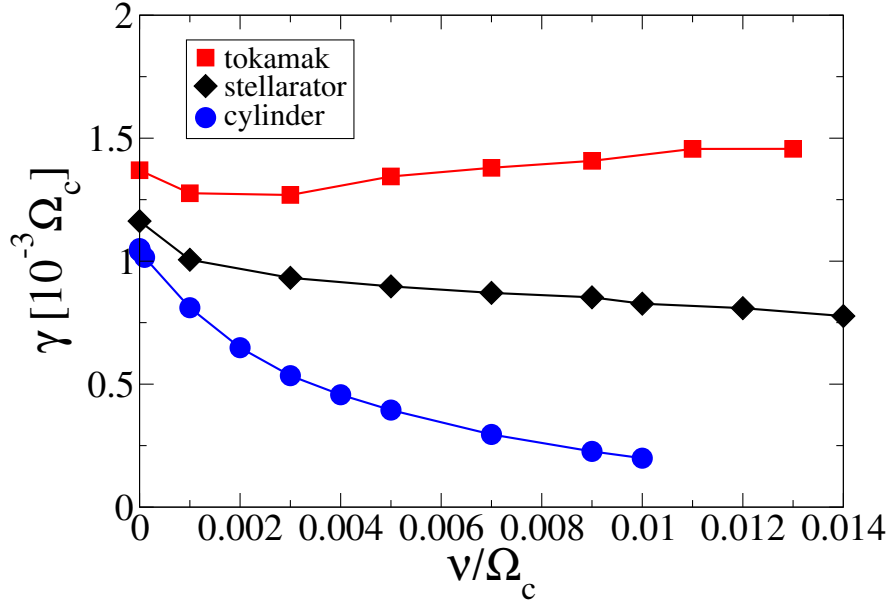


Figure 5.2: Growth rate dependence on collisionality for different geometries. In this case, LHD was chosen as the example of stellarator geometry.

angle from θ to $-\theta$ and the toroidal angle from ϕ to $-\phi$, whereas the tokamak reinsertion changes only the poloidal angle θ to $-\theta$, but leaves the toroidal angle unchanged. If this is not done, the stellarator runs break down, because the particle is reinserted in a place where the magnetic field B is not the same while μ stays constant, thus, the energy is not conserved.

Fig. 5.2 shows the growth rate γ as a function of the collision frequency ν for the three different configurations. It is possible to observe that for the slab ITG modes in cylindrical geometry, the growth rate decreases strongly with increasing collisionality. This is in agreement with [3], however, it is relevant to point out that if conservation of parallel momentum were added, the growth rate should show a different behavior with respect to the collision frequency [83]. As a consequence, even though the pitch-angle scattering operator does not portray a realistic physical effect, it allows us to differentiate between a mode that it is mainly driven by parallel dynamics, from a mode that is essentially toroidal.

In contrast to the slab ITG mode, the curvature driven ITG mode is not affected significantly by parallel dynamics, thus, collisionality does not modify the growth rate considerably.

5. MICROINSTABILITIES

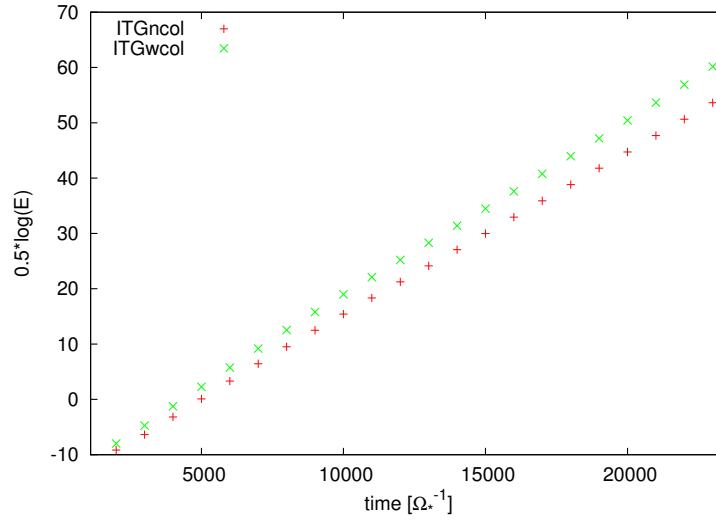


Figure 5.3: Evolution in time of the electric field energy for ITGs with and without collisions.

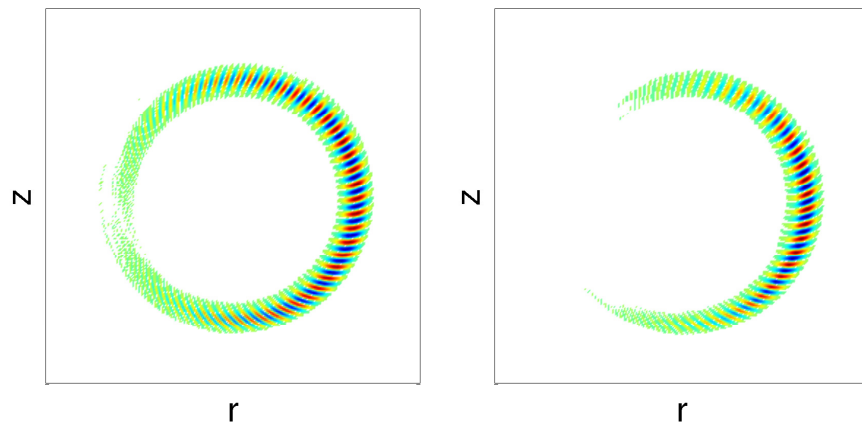


Figure 5.4: Poloidal cuts for the ITG instability at a time= $2.2 \times 10^4 \Omega_*^{-1}$. On the left: $\nu = 0$. On the right: $\nu = 1 \times 10^{-2} \Omega_*$.

This can be observed for the tokamak geometry in the following figures. In Fig. 5.3 we have plotted the electric field energy evolution in time. We can see that the growth rate of the instability (slope) is slightly higher in the collisional case, but not by a significant amount. It can also be observed that the mode structure (Fig. 5.4) does not differ considerably in shape; collisions just lead to a stronger localization of the instability zone at the outer side of the torus. This confirms the fact that in tokamaks, where toroidal ITG modes are dominant, collisionality is not so important for the growth rates.

In the LHD case, the ITG growth rate decreases, although not as strongly as in the cylinder case. This could be mainly because in stellarator devices we could have a mixture of slab ITG modes and curvature driven modes, so that the parallel dynamics can also play a role for the instability. A more detailed account of collisional effects will be given in section 5.4.3.

Next we investigate the effects of collisionality on the onset of the instability, i.e. on the threshold η_{ic} . The η_i variation is performed by varying the value of κ_n in the range of $[0, 4]$ and leaving the inverse of the temperature length scale constant, i.e. $\kappa_T = 3.5$. The density and temperature profile widths were chosen as $\Delta s_n = 0.2$ and $\Delta s_T = 0.2$ respectively. We use more points near marginal stability to resolve it better. One consideration to take into account when measuring growth rates near the marginal point is to let the simulation run long enough so that the instability is given sufficient time to develop and to have a noticeable slope. It is difficult to distinguish a slightly unstable mode from a stable one, since it requires long run times.

The growth rate dependence on η_i is displayed in Figs. 5.5 and 5.6. The dotted lines and open symbols represent the collisionless case, whereas the solid lines and filled symbols represent the collisional case, with a collisionality $\nu = 1 \times 10^{-2} \Omega_*$. From Fig. 5.5 we take an enlarged area represented in Fig. 5.6, which allows us to distinguish the critical value of η_i ($\eta_{i,c}$) at which an instability develops for the different devices and collisionalities. It can be noticed that the instability threshold value in cylindrical geometry is reduced by collisions. This is due to the collisional coupling between parallel and perpendicular temperatures [3], allowing the system to access more degrees of freedom. In the *collisionless* plasma limit, there is no coupling, thus the threshold for slab ITG modes is higher. In the

5. MICROINSTABILITIES

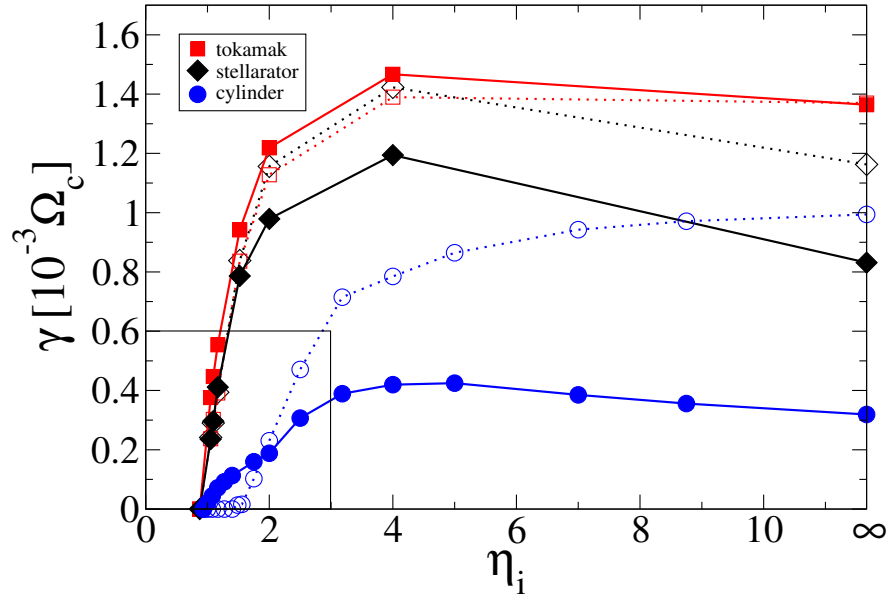


Figure 5.5: Growth rate dependence on η_i . Collisionless case (dotted lines and open symbols). Collisional case (solid lines and filled symbols). The black box indicates the area enlarged and displayed in Fig. 5.6.

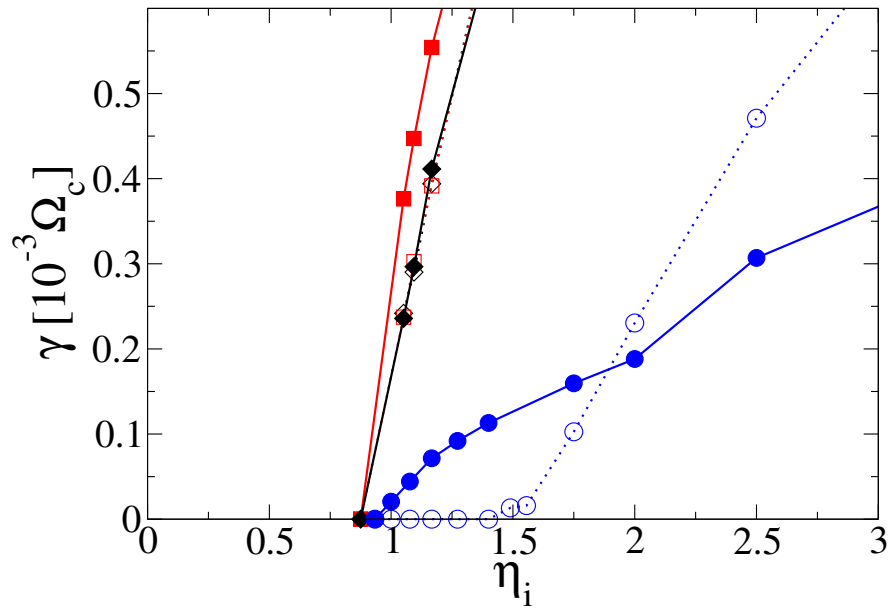


Figure 5.6: Detail of Fig. 5.5

opposite case, in which the plasma is highly collisional, the threshold drops as a consequence of the additional degrees of freedom of the system and the parallel and perpendicular temperatures are now strongly coupled.

In the tokamak case, collisions do not have a significant effect on the threshold (Fig. 5.6), which is in agreement with theoretical results [3]. Similarly for the stellarator configuration, collisions do not modify the onset of the instability. Nevertheless, for sufficiently large values of η_i , a decrease of the growth rate is observed with increasing η_i (see Fig. 5.5) in both collisionless and collisional cases, a phenomenon which is not present in the tokamak case.

5.4.2 Collisional TEM instabilities in a tokamak

As already explained, when fully kinetic electrons are included in the circular tokamak case, the dynamics of the trapped electrons also come into play, which provide an additional instability mechanism, even without collisions. When having kinetic electrons in the simulations it becomes necessary to lower the time step to be able to resolve the timescales of the electrons. The motion of the electrons is $\sqrt{m_i/m_e}$ times faster than the ion motion, thus the value of the time step needed to simulate TEM instabilities is roughly two orders of magnitude smaller than the one needed for ITG runs. This requirement makes the simulations much more costly (roughly, about two orders of magnitude more) in terms of CPU-hours.

Fig. 5.7 is similar to Fig. 5.5, but now the aspect ratio considered is $A = 3$. For simplicity, we set the electron temperature gradient to zero, i.e. $\eta_e = 0$. For this figure, no collisions were taken into account. The points displayed in red are the values of the growth rates with kinetic electrons. For the η_i scan, the density profile was kept the same with $\kappa_n = 0.875$ while varying κ_T . It is possible to see that in the region for values below the onset ($\eta_{i,c}$), where no ITG modes were present before, now we have non-zero growth rates. One can assert that these modes are purely associated with TEM, whereas when we move to higher values of η_i we can no longer distinguish between TEM and ITG instabilities. In this region ($\eta_i \sim [1 - 2]$ in the figure) one refers to a coupled ITG/TEM instability.

Unlike the ITG case, collisions do affect TEM instabilities considerably. In these simulations, it is observed that collisions lead to a smaller growth rate. TEMs

5. MICROINSTABILITIES

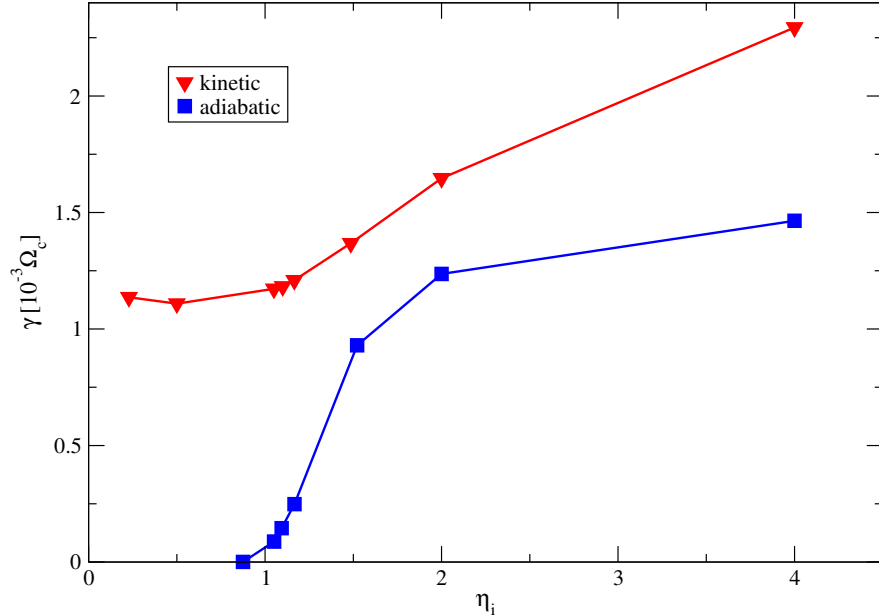


Figure 5.7: Growth rate vs. η_i for a tokamak with aspect ratio $A = 3$ in the collisionless case. The simulations with adiabatic electrons are represented by the blue curve. Simulations with kinetic electrons are depicted in red.

persist depending on whether the value of R/L_n is higher or lower than R/L_{Ti} , i.e. if the instability is driven predominantly by density or temperature gradients [4, 5]. This can be seen in Fig. 5.8, where the same major radius $R = 4$ m was used and $R/L_{Ti} = 3.21$ was kept constant. If the density profile gets flatter ($R/L_n < 3$), the mode is fully suppressed for higher collisionalities. When $R/L_n = 3.75$, the growth rate tends to become constant for higher collisionalities.

This result suggests that even in highly collisional plasmas, TEM effects could be of relevance.

5.4.3 Collisional ITG instabilities in LHD

The inclusion of collisions in EUTERPE now allows the calculation of effects of such collisions on ITG modes in stellarators, as already shown briefly in Fig. 5.2. First, we study these effects in LHD [84]. To investigate the nature of the modes further, we studied the spatial structure of the electrostatic potential. In Figs. 5.9 and 5.10, the real part of the potential $\Re(\phi)$ for the collisional and collisionless

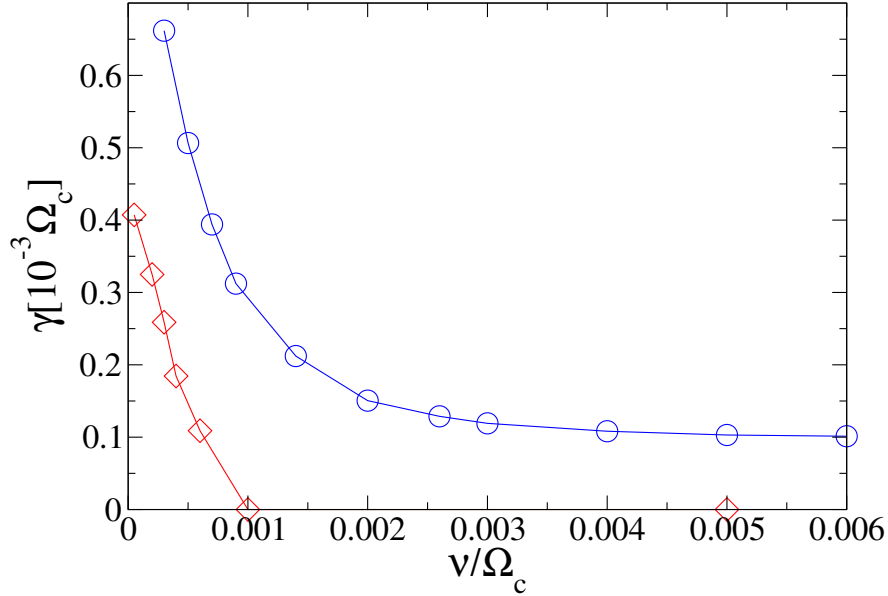


Figure 5.8: TEM instability growth rate as a function of collisionality for $R/L_{Te} = 0$, $R/L_{Ti} = 3.21$. Blue circles represent the values for $R/L_n = 3.75$. Red diamonds, for $R/L_n = 2.57$.

cases at the beginning and the middle of a period is shown. Interestingly, it is found that the mode is not localized at the low field side, as it is in the case of standard ballooning modes in a tokamak, but they are rather found at the bottom of the device. Comparing the structure of the potential at the beginning and middle of a period, shows that, despite the strong helical twist of LHD and its unfavorable curvature region being helically symmetric, the modes are nearly axisymmetric and are only slightly modified by the variation of the equilibrium with the toroidal angle, i.e. , they are independent from the unfavorable curvature.

When collisions are included ($\nu = 1 \times 10^{-2} \Omega_*$), we find that the structures once present in the collisionless case, become wider and more irregular. It is also observed that some of the structures are tilted in comparison with their collisionless counterparts.

5. MICROINSTABILITIES

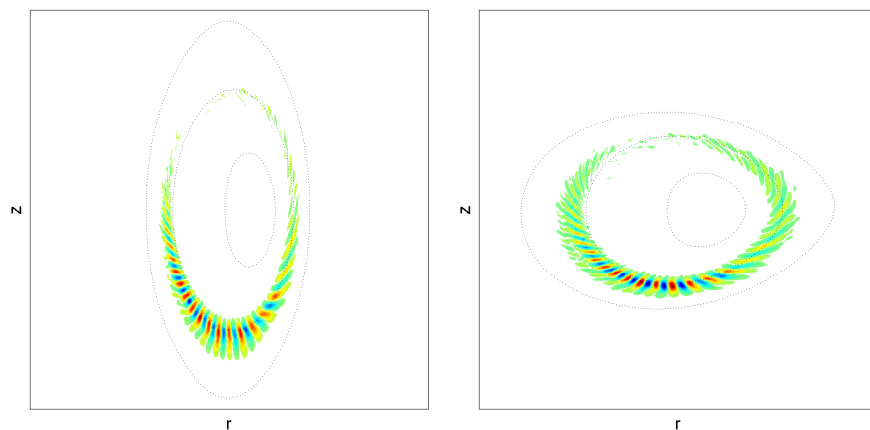


Figure 5.9: Collisionless ITG mode for LHD. Shown here is the beginning of a period ($\varphi = 0$, left) and the middle of a period ($\varphi = 2\pi/20$, right). Dashed lines represent $s = 0.1, 0.5, 1.0$.

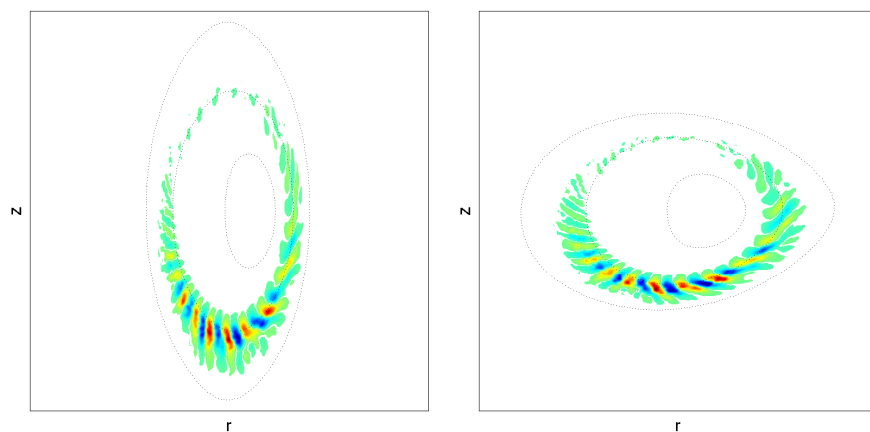


Figure 5.10: Collisional ($\nu = 1 \times 10^{-2} \Omega_*$) ITG mode for LHD at the beginning (left) and the middle (right) of a period.

5.4 Results and discussion

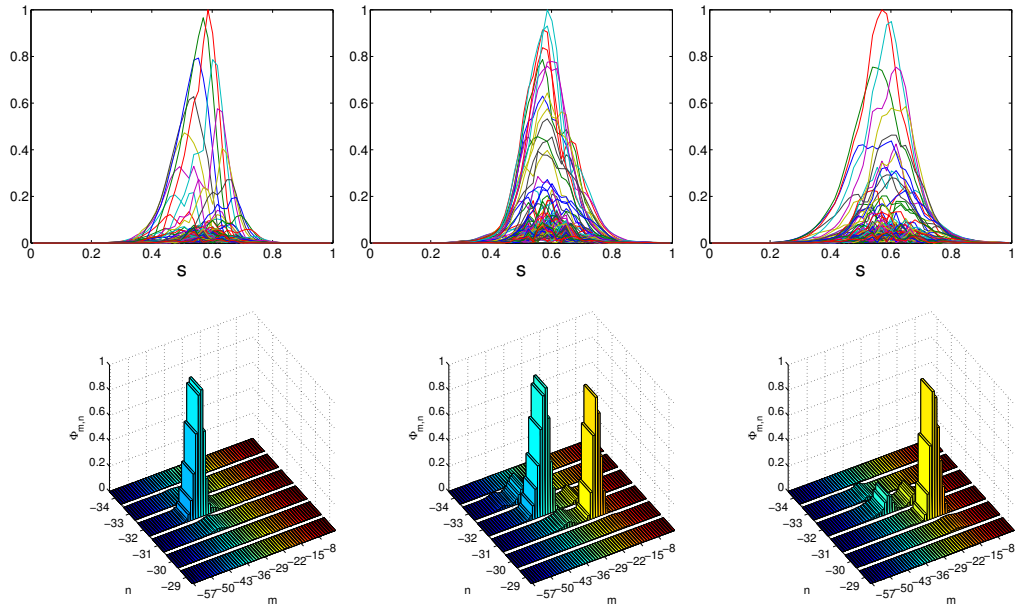


Figure 5.11: Fourier components for the electrostatic potential of the ITG mode (top) and Fourier spectra (bottom) for the ITG mode in the LHD configuration (shown here with increasing collisionality from left to right: $\nu = 0$, $\nu = 7.0 \times 10^{-3} \Omega_*$, $\nu = 1.0 \times 10^{-2} \Omega_*$).

5. MICROINSTABILITIES

The Fourier components of the electrostatic potential are presented in Fig. 5.11 (above). An additional effect of collisions can be seen in the Fourier spectrum of the electrostatic potential (see Fig. 5.11, below). Without collisions the mode exhibits a typical ballooning-like structure and has a strong coupling between the m components of the perturbation. Interestingly, despite the pronounced helical structure of LHD, the toroidal (n) sidebands are relatively small. As collisionality increases, another mode appears. Its growth rate becomes larger with increasing collisionality. In Fig. 5.11, where the collisionality is $\nu = 7.0 \times 10^{-3} \Omega_*^{-1}$ (bottom, middle), the growth rate of this second mode is almost as large as the growth rate of the mode obtained with $\nu = 0$. The two modes compete with each other as they evolve in time and this interplay never achieves a steady state (the time shown here is $t = 1 \times 10^5 \Omega_*^{-1}$), without anyone of them dominating completely. Above a critical value of the collision frequency, only the second mode remains, which has a lower m . This fact can be also noticed in the mode structure in Figs. 5.9 and 5.10, where the number of radial structures decreases at high collisionality. The remaining mode shows a somewhat weaker coupling in m and the ballooning structure becomes weaker. Also, for different values of κ_n we found that the Fourier modes coupling can be larger.

It can be seen from the figure that the modes are well localized in Fourier space. Nevertheless, a high grid resolution and consequently many Fourier modes are necessary to prevent the growth of spurious unresolved modes, located at the edge of the filter, which can otherwise dominate the simulation.

5.4.4 Collisional ITG instabilities in W7-X

Simulations of ITG modes in the stellarator Wendelstein 7-X were also carried out. For the results shown, the following parameters were used: total number of particles $N = 32 \times 10^6$, $\Delta t = 10$, the grid size was $64 \times 128 \times 128$, in s, θ, φ . $M_0 = 70$, $N_0 = -62$, the filter widths were $\Delta m = 40$, $\Delta n = 20$ and the density and temperature profiles were taken as $\kappa_n = 0.0$, $\kappa_T = 3.5$, respectively. A run takes 48 CPU-hours with 128 processors, which is longer than in the case of LHD.

It was found that collisionality changes the structure, growth rate and Fourier modes of the instability, but not by a significant amount. Unlike the LHD case, it

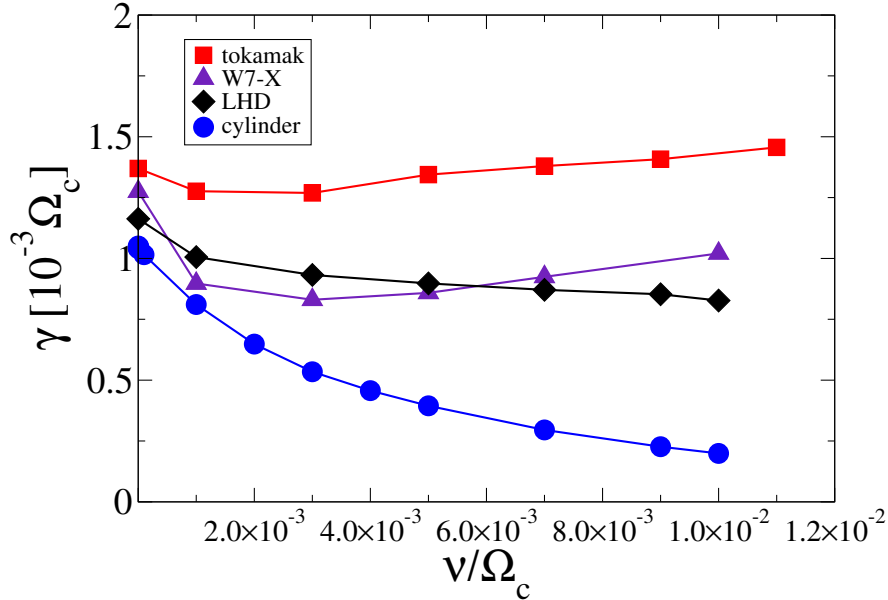


Figure 5.12: Collisionality dependence of the growth rate of ITG instabilities in different devices (as in Fig. 5.2) now including W7-X.

was not possible to observe a threshold collisionality in which an additional mode would appear.

First we consider Fig. 5.12: This figure is similar to Fig. 5.2 but now W7-X was added. It is possible to state that the W7-X growth rate is not considerably affected by collisions and exhibits a behavior closer to the tokamak, at least for high collisionalities, i.e. when the growth rate increases slightly.

It is also visible from the different poloidal cuts (Fig. 5.13), that the structures of the eigenmode do not differ significantly between the collisionless and collisional cases ($\nu = 1 \times 10^{-2} \Omega_*$), besides a slightly localizing effect. For both cases (with and without collisions) it is possible to see that the modes are strongly localized, and are always in the unfavorable curvature region. This is different to the LHD case, in which the poloidal cuts (Figs. 5.9 and 5.10) show that the modes are mainly located at the bottom of the device and are less localized.

Also, in the collisional case, the mode spreading in Fourier space becomes slightly uneven and endures small changes as it evolves with time, just like in the LHD case, with the difference that in the W7-X case, the spectrum continuously fluctuates, even for extremely high collisionalities. From this we can say that the

5. MICROINSTABILITIES

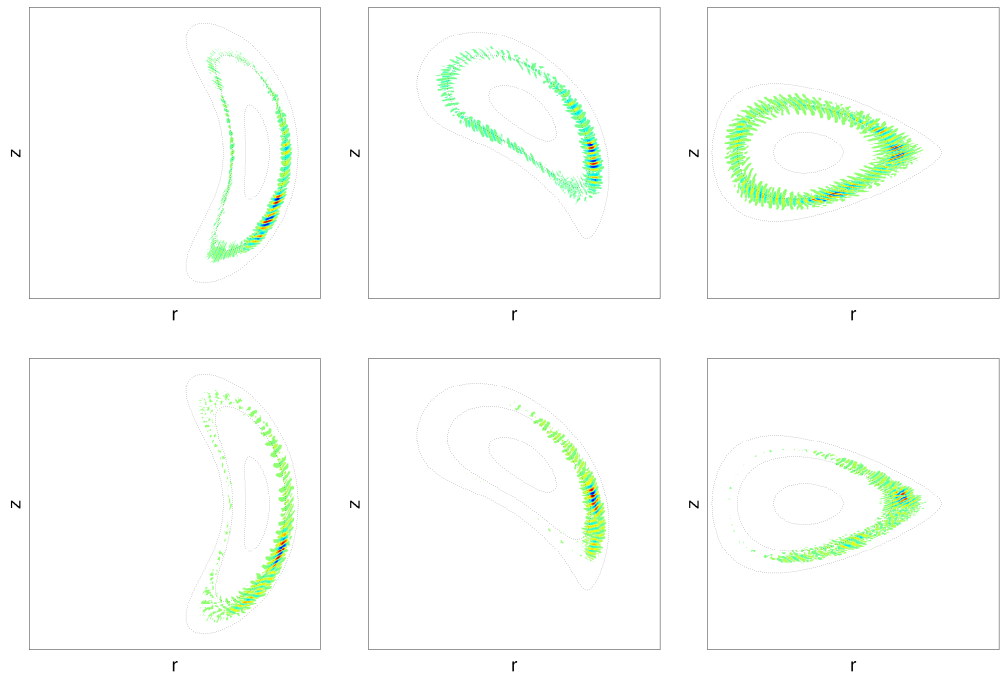


Figure 5.13: Three cross sections of W7-X over a half field period. From left to right $\varphi = 0$, $\varphi = 2\pi/20$, $\varphi = 2\pi/10$. Above: without collisions; below: collisional case with frequency $\nu = 1 \times 10^{-2} \Omega_*$.

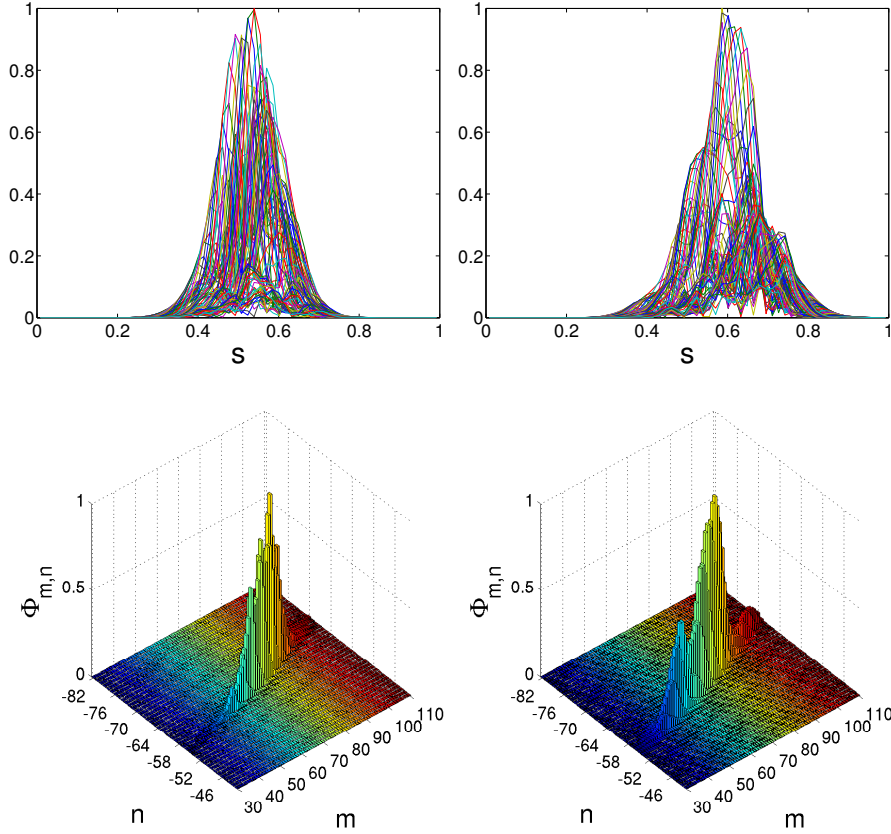


Figure 5.14: Fourier components for the electrostatic potential of the ITG mode (top) and Fourier spectra (bottom) for W7-X configuration. Shown here for $\nu = 0$ (left) and $\nu = 1.0 \times 10^{-2} \Omega_*$ (right).

spectrum never reaches a steady state with collisions. For both the collisional and collisionless cases, a strong coupling between m and n can be observed. Comparing with the LHD spectra, we see that the W7-X spectra are much broader and contain many more Fourier components. The modes lie in a diagonal since this is the resonant subset composed by the m and n modes that satisfy $\iota(s_0)m + n \approx 0$. In comparison, the LHD spectrum (see Fig. 5.11, bottom) also lies on a resonant line, but due to the weak coupling in n , is not as spread out as the W7-X spectrum.

From these observations one can conclude that ITG instability behavior in stellarators is difficult to predict without carrying out simulations for each particular case, because it depends sensitively on the geometry of each device.

Chapter 6

Conclusions and Outlook

6.1 Conclusions

Coulomb collisions play an important role in the kinetic theory of stellarator plasmas. They control the neoclassical transport, which is usually dominant at high temperatures. They affect microinstabilities, particularly TEMs, and thus the turbulent transport. Nevertheless, prior to this thesis collisions had (to my knowledge) not been implemented in any three-dimensional gyrokinetic code.

Here, the pitch-angle scattering collision operator was successfully implemented for all species in the global gyrokinetic code EUTERPE. Following the scheme proposed in [1] and further improved in [2], a method for simulating the evolution of the parallel and perpendicular velocities of the particles was developed. This basically amounts to a diffusion process over a spherical shell in velocity space. The polar and azimuthal angles are obtained independently, through the implementation of a random number generator. The collision implementation in a code that employs the δf method requires the utilization of the two-weight scheme proposed in [39, 45]. These works differ in their presentation but the resulting schemes are equivalent. A more transparent method depicting the two-weight scheme is shown in the first part of [46]. This scheme was used for the simulations we have made, but reduces, under our assumptions, to the one-weight scheme. The main issue with the two-weight scheme is that its statistical error increases with time. As a means to circumvent this problem, the collisionless and collisional schemes can be formulated as a control-variate problem and be improved by

6. CONCLUSIONS AND OUTLOOK

adopting an enhanced control-variate technique [46], in which the noise behaves like the δf scheme for early times and is bounded for later times by the noise of the full- f scheme.

The collision implementation was tested in two cases. The first one consisted in loading the initial δf part of the distribution function as a Legendre polynomial. Since these are eigenfunctions of the Lorentz operator, the time evolution is known analytically and can be compared with the numerical results, which showed good agreement. The second test case was the Spitzer problem for a cylinder and a tokamak, where the parallel conductivity is reduced by the trapped particles. First, the current was measured in a cylinder configuration and its dependence on the external electric field and collision frequency was studied. In a second step, the parallel current was measured in the Pfirsch-Schlüter regime of a tokamak configuration, using also a velocity-dependent collision frequency and comparing it with the case of a constant collision frequency. Finally, the current was evaluated in the banana regime. In the particular case when trapped particles were suppressed by eliminating the mirror driving term it was also possible to compare the numerical results with the time-dependent solution obtained analytically, which also showed a good agreement.

As a further measure, code diagnostics were adapted to obtain the flux-surface averaged radial particle flux. The flux was computed for a tokamak configuration as well as for the LHD stellarator. It was possible to observe the characteristic analytical regimes in a tokamak configuration: the Pfirsch-Schlüter regime for high collisionalities, a plateau regime for collision frequencies near the range of the bounce frequency, and the banana-regime for low collisionalities. In the case of a stellarator, the banana regime is replaced by the $1/\nu$ regime, which was clearly observed in the LHD results. The numerical results were not only benchmarked with the analytical calculations, but in the tokamak case, they were compared with the fluxes calculated from the mono-energetic coefficients provided by the DKES code [73, 74]. In order to compare the results from EUTERPE with the analytical results as well as with the results from DKES, it was necessary to calculate the weighted energy-average of the mono-energetic coefficients. All these benchmarks also showed a good agreement. Since DKES has been part of a

combined effort to benchmark mono-energetic coefficients [75], this validates the neoclassical results obtained with EUTERPE.

Since collisions were implemented, tested and validated it was possible to perform collisional gyrokinetic simulations as a next step. First, the effects of collisions on ITGs was investigated. It was observed that collisions do not affect ITG instabilities in tokamaks, but they strongly influence the growth rate in cylinder geometry. This is expected, due to the fact that in the cylinder, the predominant instability mechanism is the one produced by slab ITGs, which are driven by parallel dynamics, and this is damped by the collision operator that was implemented. A more accurate operator that conserves parallel momentum would presumably not damp the slab ITG as much.

In tokamaks, however, the main instabilities are the toroidal ITGs, where collisions do not noticeably affect the instability growth rate, since parallel ion motion is not so important.

EUTERPE has the capability of being able to simulate kinetic electrons, and consequently, the effect of collisions on TEM modes in a tokamak could be studied. It was observed that TEMs depend strongly on collisions, which can lead to a much lower growth rate at high collisionality or even a complete stabilization of the mode, depending on whether it is driven predominantly by density or temperature gradients.

The effect of collisions on ITGs in two different stellarator configurations was studied: LHD and W7-X. In LHD, it was possible to see that the instability growth rate slightly depends on collisions and exhibits a behavior midway between a tokamak and a cylinder configuration. This is probably due to a mixture of slab and toroidal ITG modes driving the instability in this geometry. In W7-X, however, the growth rate appeared to be unaffected by collisions, resembling the results for the tokamak. This suggests that the effects of collisions on ITGs in stellarator geometries depend strongly on the specific stellarator configuration. Nevertheless, it is important to remember that the implemented collision operator does not conserve momentum, which is especially relevant for parallel dynamics. In this sense, the decrease of the growth rate clarifies only the driving mechanism behind the instability, and not whether it is stabilized physically.

6. CONCLUSIONS AND OUTLOOK

Another observed effect on ITGs in stellarators was that collisions make the ballooning structure of the Fourier modes weaker. In LHD, collisions can make two Fourier modes appear, each of which dominates the simulation intermittently. In W7-X, collisions make the spectrum fluctuate.

While the W7-X spectrum is widely spread out along the resonant line $\iota(s_0)m + n \approx 0$, the LHD spectrum is highly localized due to its weak coupling in n .

6.2 Outlook

With collisions having been implemented, an interesting neoclassical problem that the EUTERPE code could address is that of impurity transport. Highly charged impurity ions are predicted in neoclassical theory to accumulate in the center of a stellarator plasma if the radial electric field points inward, which is usually the case. Such accumulation is indeed observed experimentally and can lead to the termination of the discharge.

Conventional neoclassical theory rests on the following assumption for the perturbed part of the electric potential ϕ_1 :

$$\frac{q\phi_1}{k_B T} \ll 1. \quad (6.1)$$

However, for high Z impurities, this potential can have a strong poloidal variation $\phi_1(\theta, \varphi)$, thus, the energy of the particles can vary significantly over one and the same flux surface, rendering the neoclassical mono-energetic assumption invalid. EUTERPE, on the other hand, can take into account this ϕ_1 and simulate the full energy range of the particles without necessarily assuming that the particles are mono-energetic. It could also be of interest to implement additional neoclassical diagnostics such as the heat transport and current, as well as the measurement of the energy scattering.

Another feature that could be developed is the study of the effects of collisions on TEMs in stellarator configurations. Currently, it has not been possible to simulate them because, with kinetic electrons, a much smaller Δt (about two orders of magnitude) than for the case with adiabatic electrons is required to

resolve the fast motion of the electrons. This makes the simulations extremely expensive in terms of computational time, since they need to run long enough to be able to measure a growth rate. The study of gyrokinetic effects with collisions for new configurations is also a topic of interest.

It could also be useful to implement a momentum conserving term in the collision operator, making the description of collisions more realistic. This would make it possible to measure ITGs growth rates with greater accuracy since, in theory, when momentum is conserved in the parallel direction, the growth rates of slab ITG modes should show a different behavior with collisionality [3]. Also, momentum correction could allow computations of the bootstrap current for neoclassical calculations to be carried out.

Finally, the code could be further optimized by the implementation of a higher order collisional pushing method for the particles. The current method is of first order whereas the collisionless push is implemented using a Runge-Kutta method of 4th order.

References

- [1] T. Takizuka and H. Abe. A binary collision model for plasma simulation with a particle code. *J. Comput. Phys.*, 25(3):205, 1977.
- [2] T. Vernay. Numerical study of electron-ion collision effects on trapped electron modes with the gyrokinetic code ORB5. Master's thesis, École Polytechnique Fédérale de Lausanne., 2008.
- [3] A. M. Dimits and B. I. Cohen. Collision operators for partially linearized particle simulation codes. *Phys. Rev. E*, 49(1):709, 1994.
- [4] C. Angioni, A. G. Peeters, F. Jenko, and T. Dannert. Collisionality dependence of density peaking in quasilinear gyrokinetic calculations. *Phys. Plasmas*, 12(11):112310, 2005.
- [5] J. W. Connor, R. J. Hastie, and P. Helander. Stability of the trapped electron mode in steep density and temperature gradients. *Plasma Phys. Control. Fusion*, 48(6):885, 2006.
- [6] A. H. Wapstra and G. Audi. The 1983 atomic mass evaluation: (I). Atomic mass table. *Nucl. Phys. A*, 432(1):1, 1985.
- [7] J. D. Lawson. Some Criteria for a Power Producing Thermonuclear Reactor. *Proc. Phys. Soc. B*, 70(1):6, 1957.
- [8] T. H. Stix. Highlights in early stellarator research at Princeton. *J. Plasma Fusion Res. SERIES*, 1:3, 1998.

REFERENCES

- [9] A.A. Galeev and R.Z. Sagdeev. Transport phenomena in a collisionless plasma in a toroidal magnetic system (collisionless plasma transport phenomena associated with particle drift in toroidal magnetic system, considering trapped particles role). *Sov. Phys. JETP*, 26(1):233, 1968.
- [10] G. Grieger, C. D. Beidler, H. Maassberg, E. Harmeyer, F. Herrnegger, J. Junker, J. Kisslinger, W. Lotz, P. Merkel, J. Nührenberg, F. Rau, J. Sapper, A. Schlüter, F. Sardei, and H. Wobig. In *Plasma Physics and Controlled Nuclear Fusion Research 1990*, volume 3, page 525. International Atomic Energy Agency, Vienna, 1991.
- [11] X. Garbet. Turbulence in fusion plasmas: key issues and impact on transport modelling. *Plasma Phys. Control. Fusion*, 43(12A):A251, 2001.
- [12] W. M. Tang. Microinstability theory in tokamaks. *Nucl. Fusion*, 18(8):1089, 1978.
- [13] L. I. Rudakov and R. Z. Sagdeev. On the instability of a nonuniform rarefied plasma in a strong magnetic field. *Dokl. Akad. Nauk SSSR*, 138:581, 1961. [English transl.: *Sov. Phys. Dokl.* 6:415, 1961].
- [14] W. Horton, D. I. Choi, and W. M. Tang. Toroidal drift modes driven by ion pressure gradients. *Phys. Fluids*, 24(6):1077, 1981.
- [15] B. B. Kadomtsev and O. P. Pogutse. Dissipative, trapped-particle instability in a dense plasma. *Sov. Phys. Dokl.*, 14:470, 1969.
- [16] M. Kick, H. Maaßberg, M. Anton, J. Baldzuhn, M. Endler, C. Görner, M. Hirsch, A. Weller, S. Zoletnik, and the W7-AS Team. Electric field and transport in W7-AS. *Plasma Phys. Control. Fusion*, 41(3A):A549, 1999.
- [17] R. W. Hockney and J. W. Eastwood. *Computer Simulation Using Particles*. New York: McGraw-Hill, 1981.
- [18] G. Jost. *Simulations particulières d'ondes de dérive dans des configurations magnétiques 3D*. PhD thesis, Centre de Recherches en Physique des Plasmas (CRPP), Association Euratom - Confédération Suisse, École Polytechnique Fédérale de Lausanne., 2000.

REFERENCES

- [19] G. Jost, T.M. Tran, and K. Appert. Global linear gyrokinetic PIC simulations in 3D magnetic configurations. In *Theory of Fusion Plasmas, International Workshop, Varenna*, page 419. Editrice Compositori, Società Italiana di Fisica, Bologna, 1999.
- [20] G. Jost, T. M. Tran, W. A. Cooper, L. Villard, and K. Appert. Global linear gyrokinetic simulations in quasi-symmetric configurations. *Phys. Plasmas*, 8(7):3321, 2001.
- [21] V. Kornilov. *Global Ion-Temperature-Gradient Driven Instabilities in Stellarators within Two-Fluid and Gyrokinetic Descriptions*. PhD thesis, Ernst-Moritz-Arndt-Universität, Mathematisch-Naturwissenschaftlichen Fakultät., 2004.
- [22] V. Kornilov, R. Kleiber, R. Hatzky, L. Villard, and G. Jost. Gyrokinetic global three-dimensional simulations of linear ion-temperature-gradient modes in Wendelstein 7-X. *Phys. Plasmas*, 11(6):3196, 2004.
- [23] E. Sánchez, R. Kleiber, R. Hatzky, A. Soba, X. Sáez, F. Castejón, and J. M. Cela. Linear and nonlinear simulations using the EUTERPE gyrokinetic code. *Plasma Science, IEEE Transactions on*, 38(9):2119, 2010.
- [24] R. Kleiber, R. Hatzky, and A. Mishchenko. Simulation of residual zonal flow levels in stellarators including a radial electric field. *Contrib. Plasm. Phys.*, 50(8):766, 2010.
- [25] W. D. D’Haeseleer, W. N. G. Hitchon, J. D. Callen, and J. L. Shohet. *Flux coordinates and magnetic field structure: a guide to a fundamental tool of plasma theory*. Springer, 1991.
- [26] R. D. Hazeltine. Recursive derivation of drift-kinetic equation. *Plasma Phys.*, 15(1):77, 1973.
- [27] R. G. Littlejohn. Variational principles of guiding centre motion. *J. Plasma Phys.*, 29:111, 1983.

REFERENCES

- [28] T. S. Hahm. Nonlinear gyrokinetic equations for tokamak microturbulence. *Phys. Fluids*, 31(9):2670, 1988.
- [29] S. P. Hirshman and D. K. Lee. MOMCON: A spectral code for obtaining three-dimensional magnetohydrodynamic equilibria. *Comput. Phys. Commun.*, 39(2):161, 1986.
- [30] R. C. Grimm, J. M. Greene, and J. L. Johnson. Computation of the magnetohydrodynamic spectrum in axisymmetric toroidal confinement systems. In J. Killeen, editor, *Controlled Fusion*, volume 16 of *Methods in Computational Physics*, page 253. Academic Press, New York, 1976.
- [31] S. Balay, J. Brown, K. Buschelman, W. D. Gropp, D. Kaushik, M. G. Knepley, L. C. McInnes, B. F. Smith, and H. Zhang. PETSc Web page, 2011. <http://www.mcs.anl.gov/petsc>.
- [32] S. Balay, J. Brown, K. Buschelman, V. Eijkhout, W. D. Gropp, D. Kaushik, M. G. Knepley, L. C. McInnes, B. F. Smith, and H. Zhang. PETSc users manual. Technical Report ANL-95/11 - Revision 3.1, Argonne National Laboratory, 2010.
- [33] S. Balay, W. D. Gropp, L. C. McInnes, and B. F. Smith. Efficient management of parallelism in object oriented numerical software libraries. In E. Arge, A. M. Bruaset, and H. P. Langtangen, editors, *Modern Software Tools in Scientific Computing*, pages 163--202. Birkhäuser Press, 1997.
- [34] R. Hatzky. Domain cloning for a particle-in-cell (PIC) code on a cluster of symmetric-multiprocessor (SMP) computers. *Parallel Computing*, 32(4):325, 2006.
- [35] M. Kotschenreuther. Numerical simulation. *Bulletin of the American Physical Society*, 33:2107, 1988.
- [36] A. Y. Aydemir. A unified Monte Carlo interpretation of particle simulations and applications to non-neutral plasmas. *Phys. Plasmas*, 1(4):822, 1994.

REFERENCES

- [37] G. Hu and J. A. Krommes. Generalized weighting scheme for δf particle-simulation method. *Phys. Plasmas*, 1(4):863, 1994.
- [38] Y. Chen and R. B. White. Collisional δf method. *Phys. Plasmas*, 4(10):3591, 1997.
- [39] W. X. Wang, N. Nakajima, M. Okamoto, and S. Murakami. A new δf method for neoclassical transport studies. *Plasma Phys. Control. Fusion*, 41(9):1091, 1999.
- [40] X. Q. Xu and M. N. Rosenbluth. Numerical simulation of ion-temperature-gradient-driven modes. *Phys. Fluids B*, 3(3):627, 1991.
- [41] R. Graham. Covariant formulation of non-equilibrium statistical thermodynamics. *Zeitschrift für Physik B Condensed Matter*, 26:397, 1977. 10.1007/BF01570750.
- [42] P. Lezaud. Introduction to Stochastic Differential Equations. online document., 2002. <http://perso.tls.cena.fr/lezaud/publications/NR02-848.ps>.
- [43] H. Risken. *The Fokker-Planck Equation*. Springer, 1996.
- [44] M. N. Rosenbluth, W. M. MacDonald, and D. L. Judd. Fokker-planck equation for an inverse-square force. *Phys. Rev.*, 107(1):1, 1957.
- [45] S. Brunner, E. Valeo, and J. A. Krommes. Collisional δf scheme with evolving background for transport time scale simulations. *Phys. Plasmas*, 6(12):4504, 1999.
- [46] R. Kleiber, R. Hatzky, A. Könies, K. Kauffmann, and P. Helander. An improved control-variate scheme for particle-in-cell simulations with collisions. *Comput. Phys. Commun.*, 182(4):1005, 2011.
- [47] P. Helander and D. J. Sigmar. *Collisional transport in magnetized plasmas*. U.K. : Cambridge University Press, 2002.
- [48] B. A. Trubnikov. Particle interactions in a fully ionized plasma. *Rev. Plasma Phys.*, 1:105, 1965.

REFERENCES

- [49] C. Liu, H. Qin, C. Ma, and X. Yu. A gyrokinetic collision operator for magnetized Lorentz plasmas. *Phys. Plasmas*, 18(3):032502, 2011.
- [50] A. H. Boozer and G. Kuo-Petravic. Monte Carlo evaluation of transport coefficients. *Phys. Fluids*, 24(5):851, 1981.
- [51] K. Nanbu. Theory of cumulative small-angle collisions in plasmas. *Phys. Rev. E*, 55:4642, 1997.
- [52] L. Spitzer. *Physics of fully ionized gases*. Interscience, New York, 1962.
- [53] S. I. Braginskii. Transport Processes in a Plasma. *Rev. Plasma Phys.*, 1:215, 1965.
- [54] C. Hastings. *Approximations for Digital Computers*. Princeton University Press, Princeton, N. J., 1955.
- [55] Z. Lin, W. M. Tang, and W. W. Lee. Gyrokinetic particle simulation of neoclassical transport. *Phys. Plasmas*, 2(8):2975, 1995.
- [56] A. Bergmann, A. G. Peeters, and S. D. Pinches. Guiding center particle simulation of wide-orbit neoclassical transport. *Phys. Plasmas*, 8(12):5192, 2001.
- [57] Website of JET, 2011. <http://www.jet.efda.org/>.
- [58] Website of MAST, 2011. <http://www.ccf.ac.uk/MAST.aspx>.
- [59] Website of IPP, 2011. <http://www.ipp.mpg.de/>.
- [60] Website of LHD, 2011. <http://www.lhd.nifs.ac.jp/en/>.
- [61] Website of TJII, 2011. http://www-fusion.ciemat.es/New_fusion/en/TJII/.
- [62] Website of ITER, 2011. <http://www.iter.org/>.
- [63] F. L. Hinton and R. D. Hazeltine. Theory of plasma transport in toroidal confinement systems. *Rev. Mod. Phys.*, 48(2):239, 1976.

REFERENCES

- [64] H. Maaßberg, R. Brakel, R. Burhenn, U. Gasparino, P. Grigull, M. Kick, G. Kuhner, H. Ringler, F. Sardei, U. Stroth, and A. Weller. Transport in stellarators. *Plasma Phys. Control. Fusion*, 35(SB):B319, 1993.
- [65] B. B. Kadomtsev and O. P. Pogutse. Trapped particles in toroidal magnetic systems. *Nucl. Fusion*, 11(1):67, 1971.
- [66] U. Stroth. Transport in toroidal plasmas. *Lect. Notes Phys., Springer-Verlag Berlin Heidelberg*, 670:213, 2005.
- [67] R. J. Bickerton, J. W. Connor, and J. B. Taylor. Diffusion driven plasma currents and bootstrap tokamak. *Nat. Phys. Sci.*, 229:110, 1971.
- [68] L. Spitzer and R. Härm. Transport phenomena in a completely ionized gas. *Phys. Rev.*, 89:977, 1953.
- [69] S. P. Hirshman and D. J. Sigmar. Neoclassical transport of impurities in tokamak plasmas. *Nucl. Fusion*, 21(9):1079, 1981.
- [70] D. Pfirsch and A. Schlüter. Der Einfluß der elektrischen Leitfähigkeit auf das Gleichgewichtsverhalten von Plasmen niedrigen Drucks in Stellaratoren. Technical report, Max-Planck-Institut für Plasmaphysik, Garching, 1962. MPI/Pa/7/62.
- [71] V. V. Nemov, S. V. Kasilov, W. Kernbichler, and M. F. Heyn. Evaluation of $1/\nu$ neoclassical transport in stellarators. *Phys. Plasmas*, 6(12):4622, 1999.
- [72] Y. Turkin. Magnetic Configuration Viewer (MCView). Max-Planck Institut für Plasmaphysik, 2011. Private communications with Y. Turkin.
- [73] S. P. Hirshman, K. C. Shaing, W. I. van Rij, C. O. Beasley Jr., and E. C. Crume Jr. Plasma transport coefficients for nonsymmetric toroidal confinement systems. *Phys. Fluids*, 29(9):2951, 1986.
- [74] W. I. van Rij and S. P. Hirshman. Variational bounds for transport coefficients in three-dimensional toroidal plasmas. *Phys. Fluids B*, 1(3):563, 1989.

REFERENCES

- [75] C. D. Beidler, K. Allmaier, M. Yu. Isaev, S. V. Kasilov, W. Kernbichler, G. O. Leitold, H. Maaßberg, D. R. Mikkelsen, S. Murakami, M. Schmidt, D. A. Spong, V. Tribaldos, and A. Wakasa. Benchmarking of the mono-energetic transport coefficients results from the international collaboration on neoclassical transport in stellarators (ICNTS). *Nucl. Fusion*, 51(7):076001, 2011.
- [76] K. Kauffmann, R. Kleiber, and R. Hatzky. Collisional effects on global gyrokinetic particle-in-cell simulations of ITG and TEM instabilities in tokamaks. Poster presented at the EPS, 37th Conference on Plasma Physics, Dublin, Ireland., 2010.
- [77] I. S. Gradshteyn and I. M. Ryzhik. *Table of Integrals, Series, and Products*. Academic Press, 1965.
- [78] A. B. Mikhailovskii. *Theory of Plasma Instabilities, Vol. 2: Instabilities of an Inhomogeneous Plasma, Chapter 3*. Consultants Bureau, New York, 1974.
- [79] S. Brunner. *Global approach to the spectral problem of microinstabilities in tokamak plasmas using a gyrokinetic model*. PhD thesis, École Polytechnique Fédérale de Lausanne, 1997.
- [80] F. Romanelli. Ion temperature-gradient-driven modes and anomalous ion transport in tokamaks. *Phys. Fluids B*, 1(5):1018, 1989.
- [81] X. Garbet, L. Laurent, F. Mourgues, J. P. Roubin, A. Samain, X. L. Zou, and J. Chinardet. Ionic instability thresholds in tokamaks. *Phys. Fluids B*, 4(1):136, 1992.
- [82] M. Rosenbluth and M. L. Sloan. Finite-beta stabilization of the collisionless trapped particle instability. *Phys. Fluids*, 14(8):1725, 1971.
- [83] Z. Chang and J. D. Callen. Unified fluid/kinetic description of plasma microinstabilities. part II: Applications. *Phys. Fluids B*, 4(5):1182, 1992.
- [84] K. Kauffmann, R. Kleiber, R. Hatzky, and M. Borchardt. Global linear gyrokinetic simulations for LHD including collisions. *Journal of Physics: Conference Series*, 260(1):012014, 2010.

Hiermit erkläre ich, dass diese Arbeit bisher von mir weder an der Mathematisch-Naturwissenschaftlichen Fakultät der Ernst-Moritz-Arndt-Universität Greifswald noch einer anderen wissenschaftlichen Einrichtung zum Zwecke der Promotion eingereicht wurde.

Ferner erkläre ich, dass ich diese Arbeit selbständig verfasst und keine anderen als die darin angegebenen Hilfsmittel und Hilfen benutzt und keine Textabschnitte eines Dritten ohne Kennzeichnung übernommen habe.

(Karla Kauffmann)

Karla Andrea Kauffmann Figueroa

PERSONAL DETAILS

Address : Gutsweg 8, D-17491 Greifswald, Germany
Telephone : +49 (0) 3834 - 888 - 290
E-mail : karla.kauffmann@ipp.mpg.de
Date of Birth : January 25th, 1982
Birthplace : Antofagasta, Chile
Nationality : Chilean, German

EDUCATION & WORK

- 2007 -- 2011 **PhD candidate in Physics**, Ernst-Moritz-Arndt-Universität Greifswald in association with Max-Planck-Institut für Plasmaphysik, Greifswald, Germany. Thesis title: *“Including Collisions in Gyrokinetic Tokamak and Stellarator Simulations”*. Supervisor: Prof. Dr. Per Helander.
- 2005 -- 2007 **MSc in Physics**, Universidad de Concepción, Concepción, Chile. Thesis title: *“Parametric instabilities of an Alfvén wave in a multispecies plasma: Kinetic effects”*. Supervisor: Dr. Jaime Araneda.
- 2000 -- 2005 **Licentiate Degree in Physics with a Minor in Computation and Informatics**, Maximum Distinction, Pontificia Universidad Católica de Chile, Santiago, Chile. Thesis title: *“Radio-frequency plasma simulation”*. Supervisor: Dr. Mario Favre.
- 2004 Laboratory work with plasma focus device. Laboratory of Optics and Plasma, Pontificia Universidad Católica de Chile, Santiago, Chile. Time of flight diagnostics were conducted to determine the energy of the beam particles.
- 2003 Summer job as Telescope and Instrument Operator (TIO), La Silla Observatory, ESO, Chile.
- 2002 -- 2006 Teaching and laboratory assistant in Pontificia Universidad Católica de Chile (2002-2004) and Universidad de Concepción (2005-2006)

1987 -- 1999 Primary and secondary education in The Kent School, Santiago, Chile.
Best Promotion Student 1999.

FELLOWSHIPS & AWARDS

2005 -- 2007 National Graduate Program CONICYT Grant 21050814.

2004 Grant as licentiate degree thesis student part of the FONDECYT Project 1030970: “*Experimental Investigations of Novel Plasma Sources for Ion Immersion Implantation*”.

CONFERENCE PRESENTATIONS

Contributed talks

2009 Garching-Greifswald Theory Meeting, Sellin, Germany.

2008 Garching-Greifswald Theory Meeting, Ringberg, Germany.

Contributed posters

2010 Theory of Fusion Plasmas. Joint Varenna-Lausanne International Workshop. Villa Monastero, Varenna, Italy.

2010 37th European Physical Society Conference on Plasma Physics, Dublin, Ireland.

2009 Deutsche Physikalische Gesellschaft Frühjahrstagung, Greifswald, Germany.

Workshops and schools

2007-- 2011 International Max Planck Research School (IMPRS) for Bounded Plasmas.

2006 Summer University for Plasma Physics and Fusion Research, Max-Planck-Institut für Plasmaphysik, Garching, Germany.

2004 15th symposium of the Chilean Physical Society (SOCHIFI), Antofagasta, Chile.

PUBLICATIONS

- R. Kleiber, R. Hatzky, A. Könies, **K. Kauffmann** and P. Helander: “*An improved control-variate scheme for particle-in-cell simulations with collisions*”, *Comput. Phys. Commun.* 182, 1005 (2011).
- **K. Kauffmann**, R. Kleiber, R. Hatzky and M. Borchardt: “*Global linear gyrokinetic simulations for LHD including collisions*”, *Journal of Physics: Conference Series* 260, 012014 (2010).
- **K. Kauffmann** and J. A. Araneda, “*Parametric instabilities of Alfvén waves in a multispecies plasma: Kinetic effects*”, *Phys. Plasmas* 15, 062106 (2008).

CONFERENCE PROCEEDINGS

- **K. Kauffmann**, R. Kleiber and R. Hatzky, “*Collisional effects on global gyrokinetic particle-in-cell simulations of ITG and TEM instabilities in tokamaks*”, 37th European Physical Society Conference on Plasma Physics, Dublin, Ireland (2010).
- A. Bottino, M. Borchardt, T.B. Féhér, R. Hatzky, **K. Kauffmann**, R. Kleiber, A. Könies, A. Mishchenko, A.G. Peeters, E. Poli and B. Scott: “*Global Nonlinear Gyrokinetic Simulations of Electromagnetic Turbulence in Tokamaks and Stellarator*”, 23rd IAEA Fusion Energy Conference, Daejeon, Republic of Korea (2010).
- H. Bhuyan, M. Favre, **K. Kauffmann**, H. Chuaqui, I. Mitchell and E. Wyndham: “*Comparative Studies of Ion Emission Characteristics in a Low Energy Plasma Focus Operating with Different Gas Fillings*”, *Proceedings of 15th International Conference on High-Power Particle Beams*, St. Petersburg, Russia, July 18-23 (2004).

Acknowledgements

In this section I want to thank all the people who helped me through, not only with the thesis, but also the ones who contributed to make my staying in Germany an excellent and unforgettable experience.

First, this work would have not been possible without the support and guidance of Per Helander and Ralf Kleiber. Per Helander, for receiving me in the group and not only being an inspired scientist and always ready to discuss questions, but a wonderful human being. I want to especially thank for the fact that, on my first year, he invited me, a complete stranger and alone foreigner, to spend Christmas with his lovely family. This is something I really appreciated and will never forget.

I am also extremely grateful to Ralf Kleiber for his great patience and help with all the things related to my work and EUTERPE. One day I hope I can telepathically communicate with computers like he does.

I would like to thank José García, Axel Könies, Alexey Mishchenko, Craig Beidler, Henning Maassberg, Yuriy Turkin, Matthias Borchardt and the rest of the stellarator theory group for related discussions, very helpful advice, and good atmosphere. I am also grateful to Andreas Bergmann, Emanuele Poli and Clemente Angioni for fruitful discussions, to Roman Hatzky for helping with code related issues and Henry Leyh for his help with the computers.

I owe my deepest gratitude to Jutta Gauger, Andrea Kleiber and Ute Müller for helping me survive all the German bureaucracy and for the good disposition for solving all my crazy foreigner/not-really-foreigner problems. I want to additionally thank Andrea for helping me with L^AT_EX issues.

It is a pleasure for me to thank Peter Drewelow, Steffi Braun, Håkan Smith, Tamás Fehér, Mareike Kiwitt, Josefine Proll, Hannah Brunnbauer, Julia Cantarini, Johan Anderson, Melissa Renov, Oliver Lischtschenko, Anu Korpi, Verónica Soto, Patricio Vásquez, Lucía Menéndez, Christian Czerwenka, Daniela Villegas,

Francisco Suzuki, Elizabeth Ortega and all the nice people I met during my PhD that I forgot to mention (sorry), for receiving me in Greifswald, for helping me when I needed to move, for discussing work-related and personal problems. All in all, for being there to share their friendship.

I owe my sanity to the best guitar-teacher/therapist, Lukas Müller (and Lena).

My gratefulness also extends to an eccentric group of friends who have stayed by my side for more than 25 years. It has been *with a little help of these friends* that I have been able to finish this work without going mad. Thank you, Tamara Larraín, Claudia Díaz, María Pía Fontecilla, Catherine Bernales and María Paz Majluf.

I am forever indebted to my family, Claudia Figueroa, Claus Behn, Elisa Kauffmann, Florencia Kauffmann, Ronald Kauffmann, María Teresa Parada, Max Kauffmann, Andrés Salas, my grandparents and Balú. Thank you for the support and encouragement during all these years.

Finally, I want to thank the person who helped me the most during all this time. My fiancé, Omar Jiménez. It was difficult living apart for more than 4 years, but it was worth it. I cannot thank you enough.